A Theoretical and Experimental Investigation of Nonlinear Vibrations of Buckled Beams

Walter Lacarbonara

Thesis submitted to the Faculty of the Virginia Polytechnic Institute and State University in partial fulfillment of the requirements for the degree of

Master of Science

in

Engineering Mechanics

Ali H. Nayfeh, Chair

Romesh C. Batra

Saad A. Ragab

February, 1997

Blacksburg, Virginia

Keywords: Direct Approach, Galerkin Discretization, Post-Buckling, Internal Resonances, Nonlinear Normal Modes

A Theoretical and Experimental Investigation of Nonlinear Vibrations of Buckled Beams

Walter Lacarbonara

(ABSTRACT)

There is a need for reliable methods to determine approximate solutions of nonlinear continuous systems. Recently, it has been proved that finite–degree–of–freedom Galerkin–type discretization procedures applied to some distributed–parameter systems may fail to predict the correct dynamics. By contrast, direct procedures yield reliable approximate solutions. Starting from these results and extending some of these concepts and procedures, we compare the outcomes of these two approaches (the Galerkin discretization and the direct application of a reduction method to the original governing equations) with experimental results. The nonlinear planar vibrations of a buckled beam around its first buckling mode shape are investigated. Frequency–response curves characterizing single-mode responses of the beam under a primary resonance are generated using both approaches and contrasted with experimentally obtained frequency–response curves. It is shown that discretization leads to erroneous quantitative as well as qualitative results in certain ranges of the buckling level, whereas the direct approach predicts the correct dynamics of the system.

ACKNOWLEDGMENTS

In the first place, I thank Dr. Ali H. Nayfeh whose insightful guidance has led me to produce much of this research. Also, I acknowledge the valuable learning experience with him over the last year and a half.

I would like to thank Dr. Giuseppe Rega of the University of Rome "La Sapienza" for suggesting the initial direction of my research along with the advisory of Dr. A. H. Nayfeh, and for his helpful comments. I must also express my thanks to Dr. Fabrizio Vestroni of the University of Rome for his concise yet enlightening comments that improved the quality of part of this work. Also, I express my appreciation for the time and consideration given by the other committee members, Dr. Romesh C. Batra and Saad A. Ragab.

I must also acknowledge the important contributions of others. First, I thank Wayne Kreider who initiated much of the work on buckled beams in this Lab. His comments and encouragement have been of great help in the progress of my research. I also thank Jon Pratt for his assistance in designing and implementing part of the experimental setup, Dr. Char-Ming Chin for his help in the software aspects, Randy Soper for helpful discussions, Shafic Oueini for helping with pictures of the experimental apparatus, and Adel Jilani for his assistance in running some of the experiments. Furthermore, I express my thanks to Sally Shrader for her help with LaTeX and all administrative matters.

This work was partially supported by the Rotary Foundation under a Academic–Year scholarship and the Office of Naval Research under Grant N00014-96-1-1123.

In memory of my grandmother Benedetta

Contents

List of Figures

List of Tables

Chapter 1

Introduction

1.1 Background and Motivation

Approximate methods for studying nonlinear vibrations of distributed–parameter systems are important for investigative and/or designing purposes. Most of the structures and systems respond nonlinearly if they are pushed into a nonlinear range of operation and drastic changes in their states are entailed due to some instabilities caused by external perturbations. Depending on the design criteria, a structure may operate in the nonlinear range routinely or infrequently during its lifetime. The design criteria depend in turn on the performance of suitable nonlinear analyses based on an accurate model of the nonlinear behavior of the system. Some advanced design codes (e.g., EUROCODE) allow nonlinear design of civil structures provided that a 'proper' analysis of the dynamics of the structures can be performed. Hence, suitable methods for investigating reliably the nonlinear dynamics of continuous systems are becoming increasingly important.

There are two available classes of methods for determining approximate solutions of

nonlinear continuous systems: numerical and analytical methods. With numerical methods (e.g., finite differences, finite elements, and boundary elements), the nonlinear partial–differential equations and boundary conditions are replaced with a set of nonlinear algebraic equations, which are solved in turn by using a variety of techniques. These techniques are combined with path–following algorithms to compute variation of the solution with some system parameters. By contrast, a broad class of weakly nonlinear systems can be suitably treated with approximate analytical procedures, which can be divided into discretization and direct techniques.

In discretization methods, the solution is postulated in the form

$$w(x,t) = \sum_{m=1}^{M} \phi_m(x) q_m(t) \tag{1.1}$$

where M is a finite integer. Then, one either assumes the temporal functions $q_m(t)$, time discretization, or the spatial functions $\phi_m(x)$, space discretization. With time discretization, the $q_m(t)$ are usually taken to be harmonic and the method is called the method of harmonic balance. On performing the harmonic balance, one obtains a set of nonlinear boundary–value problems for the $\phi_m(x)$.

With space discretization, the $\phi_m(x)$, referred to as trial functions, are assumed a priori. Substituting Eq. (1.1) into the governing partial–differential equations and boundary conditions, one, subsequently, performs the minimization of the residuals by using one of many available criteria, such as the Rayleigh–Ritz method, the Galerkin method, the collocation method, and the least–squares method (Finlayson, 1972, Kantorovich and Krylov, 1964). More recently, some enhanced versions of these methods (e.g., the Rayleigh–Ritz enhanced method) have been developed (Meirovitch, 1996). By employing the method of weighted residuals, one reduces the original partial–differential equations and boundary conditions to a system of ordinary–differential equations for the time–dependent functions $q_m(t)$.

One of the best known implementations of the method of weighted residuals is the Galerkin method. The fundamental requirement is that the weighting functions are chosen to be the trial functions, which must be members of a complete set of functions. In particular, if the boundary conditions are homogeneous, the trial functions are usually taken as the eigenfunctions of the linearized problem, forming themselves a complete set. In the great majority of recent works on forced nonlinear vibrations, it has been a common practice to assume as trial functions only the eigenmodes that are directly or indirectly excited (Nayfeh and Mook, 1979), regardless of the conditions under which such a projection from an infinite–dimensional space to a finite–dimensional space is performed. In particular if a system is excited near the natural frequency of a specific linear mode and that mode is not involved in an internal resonance with any other mode, only that mode is assumed in the expansion. This discretization procedure has two drawbacks. First, by minimizing the residuals, one discards the nonlinear terms that are orthogonal to the eigenmodes assumed in the expansion. Second, the shape of the motion is fixed *a priori*. On the contrary, by attacking directly a distributed–parameter system with a reduction method, such as the method of multiple scales, one does not assume the form of the solution a priori. Using two examples, we show that the discretization approach can lead to erroneous results.

First, we study the nonlinear response of an Euler–Bernoulli beam resting on an elastic foundation with distributed quadratic and cubic nonlinearities by using a single–mode Galerkin–type discretization and the direct approach and investigate their quantitative and qualitative differences. The motivation for the study of this system is the relatively simple, intrinsic mathematical structure of the governing partial–differential boundary–value problem. The results of both approaches can be quantitatively and qualitatively different. Hence, we conclude that the discretization approach may lead to erroneous results.

To confirm this conclusion, we compare the predictions of both approaches with ex-

perimental results. We conducted experiments on a buckled beam and we compared the experimental results with the outcomes of the two approximate approaches for conditions where qualitative differences exist between them. To narrow the range of investigation, we study single–mode responses of a homogeneous buckled beam around its first buckling mode shape to a primary resonant uniform base excitation. We validate predictions of the direct approach by comparing the frequency–response curves obtained with the two approximate approaches with those obtained experimentally. During the experiments, we found interesting responses involving modal interactions resulting from three–to–one, one–to–one, and simultaneous internal resonances. Therefore, we use the direct approach to develop uniform asymptotic expansions of the responses of the beam for these cases.

1.2 Literature Review

Acknowledging the failure of several attempts to formulate the problem of nonlinear, undamped, free–vibrations of beams in terms of Ritz–type finite elements by using the transverse displacement only, Bhashyam and Prathap (1980) implemented a Galerkin finite–element formulation in two different ways. First, they obtained a set of nonlinear ordinary–differential equations in terms of the nodal displacements. Recognizing certain properties of the time function at the point of maximum amplitude of the motion, they defined a nonlinear eigenvalue–like problem and determined numerically the exact mode shape – nonlinear normal mode – by iteratively solving a series of linear eigenvalue problems. Second, they applied a traditional Galerkin–type discretization by assuming a stationary mode shape. They showed that, for clamped–clamped and hinged–clamped beams, the governing integro–partial–differential equation and boundary conditions do not admit separable solutions in time and space. This result is in close agreement with the results of the direct approach. Troger and Steindl (1991) showed that, in the context of snap–buckling prob-

lems, discretization techniques, such as the Rayleigh–Ritz and Galerkin methods, can lead to qualitatively erroneous bifurcation diagrams. On the other hand, Abhyankar, Hall, and Hanagud (1993) contrasted finite–difference solutions for a hinged-hinged buckled beam with a single–mode discretization. They found that the responses obtained by the two procedures are in qualitative agreement. Leissa and Saad (1994) compared a finite–degree–of–freedom Galerkin–type discretization with a first–order central finite–difference scheme for finite–amplitude coupled longitudinal and transverse vibrations of stretched strings that involve cubic nonlinearity only. To obtain agreement between the approximate solutions, they needed to include at least 3 to 5 admissible functions in the expansions of the displacements.

1.2.1 Systems with Quadratic and Cubic Nonlinearities

Mook, Plaut, and HaQuang (1985) and Plaut, HaQuang, and Mook (1985) investigated the influence of a 2:1 internal resonance on nonlinear vibrations of general structures characterized by quadratic and cubic nonlinearities under either a subharmonic or a combination resonance. They first discretized the governing equation using the full set of linear, undamped mode shapes. In the case of subharmonic resonance, the response exhibits the saturation phenomenon. In the case of combination resonance, the response may be nonstationary with a continual exchange of energy between the internally resonant modes. Nayfeh, Nayfeh, and Mook (1992) studied nonlinear vibrations of a relief valve characterized by quadratic and cubic nonlinearities in the case of primary resonance and several relevant secondary resonances. They contrasted the results obtained by using a single–mode discretization and the direct approach. They showed that the single–mode discretization can lead to erroneous results. Nayfeh, Nayfeh, and Pakdemirli (1995) compared the results obtained by discretization and direct treatment of several one–dimensional distributed–

parameter systems with quadratic and cubic nonlinearities, including an Euler–Bernoulli beam resting on a nonlinear elastic foundation, surface waves in a rectangular container, a relief valve, and a suspended cable in the presence of a one–to–one internal resonance involving the first in–plane and out–of–plane modes.

In the next sections, the research related to continuous systems with quadratic and cubic nonlinearities is reviewed. Notably, such systems are characterized by initial curvature or initial deformation - quadratic nonlinearity - and midplane stretching - cubic nonlinearity.

1.2.2 Cables

Pakdemirli, Nayfeh, and Nayfeh (1995) studied the dynamics of a suspended cable in the case of a one–to–one autoparametric internal resonance involving the first symmetric in–plane and first antisymmetric out–of–plane modes by using a two–mode Galerkin discretization and the direct treatment. They found differences in the obtained frequency–response curves and the predicted bifurcations of the system response. Benedettini, Rega, and Alaggio (1995) used a four–mode discretization to study nonlinear in–plane and out–of–plane responses of a suspended cable to different external resonance conditions in the presence of multiple internal resonances. They found complex dynamic and chaotic solutions. Recognizing the inadequacy of the four–mode discretization in explaining some of the experimental observations, Rega, Lacarbonara, and Nayfeh (1996) used the direct approach to develop an asymptotic model for coupled in–plane and out–of–plane vibrations in the case of multiple internal resonances involving the first two in–plane and first two out–of–plane modes. They showed that the predicted coefficients of the terms appearing in the modulation equations differ significantly from those obtained with the discretization approach.

1.2.3 Arches

Extensive research has been done on either shallow or nonshallow arches. However, all of the studies to date are based on a Galerkin–type discretization. Nayfeh (1984) studied the response of a shallow arch to a two–frequency transverse load with each frequency being nearly twice a natural frequency. He retained in the discretization only the two modes that are directly excited by the subharmonic resonances. Tien, Namachchivaya, and Bajaj (1994) and Tien, Namachchivaya, and Malhotra (1994) used the generalized Melnikov method to determine conditions for the existence of Smale horseshoe–type chaos in a two–mode discretization model of a shallow arch for the cases of two–to–one and one–to–one internal resonance. Thomsen (1992) investigated the response of nonshallow arches to a subharmonic resonance of order one–half of the lowest symmetric mode in the case of a two–to–one internal resonance using a two–mode discretization.

1.2.4 Shells

Recently, there has been a growing interest in two–dimensional continuous systems. Karesmen, Ileri, and Akkas (1992) investigated chaotic dynamics of viscoelastic shallow spherical shells. Nayfeh and Raouf (1987) and Raouf and Nayfeh (1990) used the direct approach to study nonlinear forced responses of infinitely long cylindrical shells in the case of a 1:1 autoparametric resonance. Chin and Nayfeh (1995) investigated the response of an infinitely long cylindrical shell to a primary resonance of one of its orthogonal flexural modes by using a two–mode discretization and the direct approach. They found that the two–mode discretization results in erroneous predictions because it does not account for the effects of the quadratic nonlinearities.

1.2.5 Buckled Beams

Buckled beams have received great attention in the last fifty years. Bisplinghoff and Pian (1957) investigated theoretically and experimentally linear vibrations of hinged–hinged buckled beams, including temperature effects and initial geometric imperfections. Recently, Nayfeh, Kreider, and Anderson (1995) and Kreider (1995) obtained an exact solution for linear vibrations of a beam around its nth buckling mode shape and validated experimentally the calculated mode shapes and natural frequencies of a clamped–clamped beam around its first buckling mode over a wide range of static buckling deflections.

Eisley (1964), Eisley and Bennett (1970), Min and Eisley (1972), and Tseng and Dugundji (1971) tackled the problem of forced nonlinear vibrations of buckled beams. They studied asymmetric and symmetric vibrations. Tseng and Dugundji (1971) presented the first experimental data regarding the snap–through phenomenon and some harmonic and superharmonic steady–state solutions. Abou–Rayan et al. (1993) studied the single–mode discretized dynamics of a parametrically excited, hinged–hinged, buckled beam; they documented interesting nonlinear phenomena, such as period–multiplying and period–demultiplying bifurcations, chaotic motions, and jump phenomena.

Yamaki and Mori (1980) documented experimentally for the first time internal and combination resonances in buckled beams. Afaneh and Ibrahim (1993) and Lee and Ibrahim (1993) investigated the dynamics of a clamped–clamped buckled beam subject to either a harmonic or a wide–band excitation in the case of a one–to–one internal resonance. They used the lowest three modes of a straight beam to discretize the system. Ramu, Sankar, and Ganesan (1994) presented a thorough investigation of the bifurcations of the response of a buckled beam. They used the first two modes of a straight beam to discretize the governing integro–partial–differential equation and associated boundary conditions. However, they did not address the problem of the dependence of the bifurcation patterns

on the discretization scheme.

Nagai (1990) documented experimentally chaotic vibrations of a clamped-clamped beam subject to a periodic end load. Nagai and Yamaguchi (1994) and Yamaguchi and Nagai (1994) presented experimental and theoretical results concerning the chaotic dynamics of a post-buckled beam carrying a concentrated mass.

By using the direct approach, Kreider (1995) developed approximate solutions for single–mode responses to a primary resonant uniform distributed excitation and 1:1 and 2:1 internal resonances. He presented experimental data for nonlinear asymmetric single–mode responses for various levels of buckling. Among other interesting results, he conjectured the presence of a *subcritical* period–doubling bifurcation of the single–mode motions at buckling levels higher than that corresponding to the first crossover and a *supercritical* period–doubling bifurcation route to chaos at buckling levels below the first crossover. This conjecture arose from consistent and repeated observations of transient period–doubled responses that developed into chaotic motions. Kreider, Nayfeh, and Chin (1995) used the direct approach to analyze the vibrations of buckled beams with two–to–one internal resonance about a static buckling deflection, taking into account quadratic nonlinearities only. They found that the response of the beam is complex.

Recently, Pellicano and Vestroni (1997) addressed the nonlinear dynamic behavior of a hinged-hinged, axially moving beam in the pre– and post–critical ranges. They used the Galerkin method to discretize the system and retained the first eight modes in the expansion. They found interesting dynamics above the lowest critical speed.

1.3 Contributions

A closer understanding of the limitations of Galerkin–type discretization techniques is obtained. First, we study the response of an Euler–Bernoulli beam resting on a nonlinear elastic foundation with quadratic and cubic nonlinearities to either a primary resonance or a subharmonic resonance of order one–half. We show where discrepancies between the single–mode Galerkin discretization and the direct approach results occur. Then, we explore in detail theoretically and experimentally the unimodal dynamics of a beam around its first buckling mode shape.

All of the related works on nonlinear dynamics of buckled beams assume an initially straight beam undergoing a pitchfork bifurcation at the first critical end load. Kreider (1995) conjectured that the nonstationarity of the natural frequencies in his experiments was due to a combination of slipping in the clamps and temperature changes. In the present work, recognizing the importance of these factors on the overall dynamic behavior of buckled beams, we use exact solutions to investigate the dependence of the post–buckling equilibria and linear vibrations on the initial geometric imperfections and temperature changes. As a by-product of studying the nonlinear integro–differential boundary–value problem governing pre– and post–buckling equilibria, we found *null-load solutions* for a clamped–clamped initially imperfect beam.

Kreider (1995) addressed possible errors induced by the discretization on approximate nonlinear solutions, but he did not explore them. Following Kreider (1995) and introducing a different nondimensionalization of the governing equation and boundary conditions, we use a single–mode Galerkin discretization and the direct approach to obtain approximate single–mode responses to a harmonic, uniformly distributed excitation. We compare the *effective nonlinearity* coefficients in the frequency–response equations obtained using both approaches for a broad range of buckling levels. We show that, for odd modes, there are

ranges where the computed frequency–response curves are qualitatively as well as quantitatively different. Next, we obtain experimentally frequency–response curves for two test beams with buckling levels for which qualitative differences between the results of the two approaches occur but no internal resonances are activated. The experimentally obtained frequency–response curves are in agreement with those obtained with the direct approach and in disagreement with those obtained with the discretization approach.

Finally, by exploring experimentally some of the dynamic responses of the buckled beams, we found interesting modal interactions caused by one–to–one, three–to–one, and simultaneous resonances. Therefore, we use the direct approach to develop approximate solutions for the beam motion in these cases.

Chapter 2

Beam on a Nonlinear Elastic Foundation

In this chapter, we determine the response of a hinged–hinged Euler–Bernoulli beam resting on a nonlinear elastic foundation with distributed quadratic and cubic nonlinearities to either a primary resonance ($\Omega \approx \omega_n$) or a subharmonic resonance of order one–half ($\Omega \approx 2\omega_n$) of the nth mode, where Ω is the excitation frequency and ω_n is the natural frequency of the nth mode of the beam. First, we discretize the governing equation by using the Galerkin method assuming that only the nth mode is excited. Then, we apply the method of multiple scales to the obtained nonlinear ordinary–differential equation to determine asymptotic expansions for the responses. Next, we attack directly the distributed–parameter system using the method of multiple scales.

The amplitude and phase modulation equations show that the single–mode discretization may lead to erroneous qualitative as well as quantitative predictions. Regions of softening (hardening) behavior of the system, the spatial dependence of the response drift,

and frequency–response curves are numerically evaluated and compared using both approaches. It is shown that the discretization and direct solutions, for the first mode, are in quantitative agreement; however, for higher modes, the results of both approaches are in quantitative as well as qualitative disagreement.

2.1 A Typical Model

In nondimensional form, small but finite–amplitude transverse vibrations of a hinged–hinged Euler–Bernoulli beam resting on a nonlinear elastic foundation with distributed quadratic and cubic nonlinearities are governed by

$$\frac{\partial^2 w}{\partial t^2} + \frac{\partial^4 w}{\partial x^4} + \epsilon\alpha_2 w^2 + \epsilon^2\alpha_3 w^3 + 2\epsilon^2\mu\frac{\partial w}{\partial t} = F(x)\cos(\Omega t) \tag{2.1}$$

$$w(x,t) = 0 \ \text{ and } \ \frac{\partial^2 w(x,t)}{\partial x^2} = 0 \ \text{ at } \ x = 0 \ \text{ and } \ 1 \tag{2.2}$$

where the α_i, μ, and Ω are constant and ϵ is a small nondimensional bookkeeping parameter. The linear undamped normalized eigenmodes and natural frequencies are

$$\phi_n(x) = \sqrt{2}\sin(n\pi x) \ \text{ and } \ \omega_n = n^2\pi^2 \tag{2.3}$$

2.2 Single–Mode Galerkin Discretization

To perform a single–mode Galerkin discretization, we let

$$w(x,t) \approx \phi_n(x) q_n(t) \tag{2.4}$$

and obtain the following nonlinear ordinary–differential equation for the nth generalized coordinate:

$$\ddot{q}_n + \omega_n^2 q_n + \epsilon\delta_n\alpha_2 q_n^2 + \frac{3}{2}\epsilon^2\alpha_3 q_n^3 + 2\epsilon^2\mu\dot{q}_n = f_n\cos(\Omega t) \tag{2.5}$$

where

$$\delta_n = \frac{4\sqrt{2}}{3n\pi}(1-\cos n\pi) \;\text{ and }\; f_n = \int_0^1 F(x)\phi_n(x)dx \tag{2.6}$$

We observe from Eq. (2.6) that $\delta_n = 0$ for even n. Hence the equation for q_n obtained with the Galerkin discretization does not depend on the quadratic nonlinearity and the even modes will be characterized by a hardening–type behavior if $\alpha_3 > 0$, irrespective of the value of the coefficient α_2 of the quadratic nonlinearity.

2.3 Primary Resonance of the nth Mode

To express the nearness of the excitation frequency to the natural frequency, we introduce a detuning parameter σ defined by $\Omega = \omega_n + \epsilon^2\sigma$. Hence,

$$\omega_n^2 = \Omega^2 - 2\epsilon^2\Omega\sigma + ... \tag{2.7}$$

2.3.1 Attacking the Discretized Equation

To balance the effects of the nonlinearity, damping, and resonance, we scale f as $\epsilon^2 f$, use Eq. (2.7), and rewrite Eq. (2.5) as

$$\ddot{q} + \Omega^2 q + \epsilon\delta\alpha_2 q^2 - 2\epsilon^2\sigma\Omega q + 2\epsilon^2\mu\dot{q} + \frac{3}{2}\epsilon^2\alpha_3 q^3 + ... = \epsilon^2 f\cos(\Omega t) \tag{2.8}$$

where the subscript n was dropped for simplicity of the notation.

To determine a second–order uniform expansion of the solution of Eq. (2.8) by using the method of multiple scales, we introduce the two time scales

$$T_0 = t \quad \text{and} \;\; T_2 = \epsilon^2 t \tag{2.9}$$

Hence, the temporal operators can be expanded as

$$\frac{\partial}{\partial t} = D_0 + \epsilon^2 D_2 + \dots \quad \text{and} \quad \frac{\partial^2}{\partial t^2} = D_0^2 + 2\epsilon^2 D_0 D_2 + \dots \tag{2.10}$$

where $D_n \equiv \partial/\partial T_n$. Next, we expand the time–dependent variable q in powers of ϵ as

$$q(t;\epsilon) = q_0(T_0, T_2) + \epsilon q_1(T_0, T_2) + \epsilon^2 q_2(T_0, T_2) + ... \tag{2.11}$$

Substituting Eq. (2.11) into Eq. (2.8) and equating coefficients of like powers of ϵ yields

Order ϵ^0:

$$\mathcal{D}(q_0) = D_0^2 q_0 + \Omega^2 q_0 = 0 \tag{2.12}$$

Order ϵ^1:

$$\mathcal{D}(q_1) = -\delta\alpha_2 q_0^2 \tag{2.13}$$

Order ϵ^2:

$$\mathcal{D}(q_2) = -2D_0 D_2 q_0 - 2\mu D_0 q_0 + 2\sigma\Omega q_0 - 2\delta\alpha_2 q_0 q_1 - \frac{3}{2}\alpha_3 q_0^3 + f\cos(\Omega T_0) \tag{2.14}$$

where

$$\mathcal{D}(q) = D_0^2 q + \Omega^2 q \tag{2.15}$$

The solution of Eq. (2.12) can be expressed as

$$q_0 = A(T_2)e^{i\Omega T_0} + \overline{A}(T_2)e^{-i\Omega T_0} \tag{2.16}$$

where the overbar indicates the complex conjugate. The function $A(T_2)$ will be determined by eliminating the secular terms from q_2. Substituting Eq. (2.16) into Eq. (2.13) yields

$$\mathcal{D}(q_1) = -\delta\alpha_2[A^2 e^{2i\Omega T_0} + A\overline{A}] + cc \tag{2.17}$$

whose particular solution can be expressed as

$$q_1 = \frac{\delta\alpha_2}{3\Omega^2}A^2 e^{2i\Omega T_0} - \frac{\delta\alpha_2}{\Omega^2}A\overline{A} + cc \tag{2.18}$$

where cc indicates the complex conjugate of the preceding terms. Substituting Eqs. (2.16) and (2.18) into Eq. (2.14) and eliminating the terms that lead to secular terms in q_2, we obtain the following modulation equation:

$$2i\Omega A' = -2i\mu\Omega A + 2\sigma\Omega A - \left(\frac{9}{2}\alpha_3 - \frac{10\delta^2\alpha_2^2}{3\Omega^2}\right)A^2\overline{A} + \frac{1}{2}f \tag{2.19}$$

where the prime indicates the derivative with respect to T_2.

Expressing the complex–valued amplitude A in the polar form

$$A(T_2) = \frac{1}{2}ae^{-i\gamma} \tag{2.20}$$

where a and γ are real functions of T_2 and separating Eq. (2.19) into its real and imaginary parts, we obtain the following two nonlinear ordinary–differential equations governing the modulation of the amplitude a and phase γ with T_2:

$$a' = -\mu a + \frac{f}{2\Omega}\sin\gamma \tag{2.21}$$

$$a\gamma' = \sigma a - \tilde{\alpha}_e a^3 + \frac{f}{2\Omega}\cos\gamma \tag{2.22}$$

where the effective nonlinearity coefficient $\tilde{\alpha}_e$ is given by

$$\tilde{\alpha}_e = \frac{1}{8\Omega}\left(\frac{9}{2}\alpha_3 - \frac{10\alpha_2^2\delta^2}{3\Omega^2}\right) \tag{2.23}$$

Combining Eqs. (2.4), (2.11), (2.16), (2.18), and (2.20), we express the deflection, to the second approximation, as

$$w(x,t) = \phi_n(x)\left\{a\cos(\Omega t - \gamma) + \epsilon\frac{\delta\alpha_2}{6\Omega^2}a^2\left[\cos(2\Omega t - 2\gamma) - 3\right] + ...\right\} \tag{2.24}$$

where a and γ are given by Eqs. (2.21) and (2.22). It follows from Eq. (2.24) that the drift is given by

$$\tilde{d}(x) = -\epsilon \frac{\delta_n \alpha_2}{2\Omega^2} a^2 \phi_n(x) + ... \tag{2.25}$$

We observe that for even modes $\delta_n = 0$ and hence the single–mode response obtained with the discretization approach does not predict any drift.

2.3.2 Attacking Directly the Original Equations

In this section, we apply the method of multiple scales directly to Eqs. (2.1) and (2.2) to produce a second–order uniform solution. We assume that $w(x,t)$ can be represented by an expansion having the form

$$w(x,t;\epsilon) = w_0(x,T_0,T_2) + \epsilon w_1(x,T_0,T_2) + \epsilon^2 w_2(x,T_0,T_2) + ... \tag{2.26}$$

We scale the forcing term $F(x)$ as $\epsilon^2 F(x)$. Substituting Eqs. (2.26) and (2.10) into Eqs. (2.1) and (2.2) and equating coefficients of like powers of ϵ yields

Order ϵ^0:

$$\mathcal{M}(w_0) = \frac{\partial^2 w_0}{\partial T_0^2} + \frac{\partial^4 w_0}{\partial x^4} = 0 \tag{2.27}$$

Order ϵ^1:

$$\mathcal{M}(w_1) = -\alpha_2 w_0^2 \tag{2.28}$$

Order ϵ^2:

$$\mathcal{M}(w_2) = -2\frac{\partial^2 w_0}{\partial T_0 T_2} - 2\mu \frac{\partial w_0}{\partial T_0} - 2\alpha_2 w_0 w_1 - \alpha_3 w_0^3 + F(x)\cos(\Omega T_0) \tag{2.29}$$

$$w_j = 0 \ \text{ and } \ \frac{\partial^2 w_j}{\partial x^2} = 0 \ \text{ at } \ x = 0 \ \text{ and } \ 1, \quad j = 0, 1, 2, ... \tag{2.30}$$

where

$$\mathcal{M}(w) = \frac{\partial^2 w}{\partial T_0^2} + \frac{\partial^4 w}{\partial x^4} \tag{2.31}$$

The general solution of the homogeneous boundary–value problem given by Eqs. (2.27) and (2.30) can be expressed as

$$w_0(x, T_0, T_2) = \sum_{n=1}^{\infty} \phi_n(x) A_n(T_2) e^{i\omega_n T_0} + cc \tag{2.32}$$

It can be argued from physical considerations that, for a damped system, the modes that are not directly excited by an external source or indirectly excited by an internal resonance eventually decay with time (Nayfeh and Mook, 1979). In the case of primary resonance of the nth mode and with no active internal resonances, we reduce Eq. (2.32) to

$$w_0(x, T_0, T_2) = \phi_n(x) A_n(T_2) e^{i\omega_n T_0} + cc \tag{2.33}$$

Substituting Eq. (2.33) into Eq. (2.28) yields

$$\mathcal{M}(w_1) = -\alpha_2 \phi_n^2(x)[A_n^2 e^{2i\omega_n T_0} + A_n \overline{A}_n] + cc \tag{2.34}$$

The solution of Eqs. (2.34) and (2.30) can be written as

$$w_1(x, T_0, T_2) = \frac{1}{2}\alpha_2 \Upsilon_1(x) A_n \overline{A}_n + \alpha_2 \Upsilon_2(x) A_n^2 e^{2i\omega_n T_0} + cc \tag{2.35}$$

where the functions $\Upsilon_1(x)$ and $\Upsilon_2(x)$ are solutions of the boundary–value problems

$$L(\Upsilon_1; 0) = -2\phi_n^2(x) \tag{2.36}$$

$$L(\Upsilon_2; 2\omega_n) = -\phi_n^2(x) \tag{2.37}$$

$$\Upsilon_i = 0 \text{ and } \Upsilon_i'' = 0 \text{ at } x = 0 \text{ and } 1, \quad i = 1, 2 \tag{2.38}$$

where

$$L(\Upsilon; \omega) = \Upsilon^{iv}(x) - \omega^2 \Upsilon(x) \tag{2.39}$$

The result is

$$\Upsilon_1(x) = \frac{1}{8\omega_n^2}\Big\{ \cos 2n\pi x + 2\omega_n(x^2 - x) - 1\Big\} - \frac{1}{12}\Big(x^4 - 2x^3 + x\Big) \tag{2.40}$$

$$\begin{aligned}\Upsilon_2(x) = \frac{1}{12\omega_n^2}\Big\{ & 3 + \cos 2n\pi x - 3\cos\gamma_n x - \cosh\gamma_n x \\ & -3\tan\left(\frac{\gamma_n}{2}\right)\sin\gamma_n x + \tanh\left(\frac{\gamma_n}{2}\right)\sinh\gamma_n x\Big\}\end{aligned} \tag{2.41}$$

where $\gamma_n = \sqrt{2}n\pi$.

Substituting Eqs. (2.33) and (2.35) into Eq. (2.29) yields

$$\begin{aligned}\mathcal{M}(w_2) = -\Big\{ & 2i\omega_n(A_n' + \mu A_n)\phi_n(x) \\ & + \Big[\alpha_2^2(\Upsilon_1(x) + \Upsilon_2(x))\phi_n(x) + 3\alpha_3\phi_n^3(x)\Big]A_n^2\bar{A}_n \\ & - \frac{1}{2}F(x)e^{i\sigma T_2}\Big\}e^{i\omega_n T_0} + cc + NST\end{aligned} \tag{2.42}$$

where NST stands for terms that do not produce secular terms. To determine the solvability condition (Nayfeh, 1981) at this order, we note that the associated homogeneous boundary–value problem at second order as well as at all orders is self–adjoint. Then, the solvability condition of Eqs. (2.42) and (2.30) demand that the right–hand side of Eq. (2.42) be orthogonal to $e^{-i\omega_n T_0}\phi_n(x)$. Hence, making use of the normalization of the eigenmodes and accounting for the primary resonance condition, we obtain the following solvability condition:

$$2i(A_n' + \mu A_n) = -8\alpha_e A_n^2\overline{A}_n + \frac{f}{2\omega_n}e^{i\sigma T_2} \tag{2.43}$$

where f is the nth modal force given by Eq. (2.6),

$$\alpha_e = \frac{1}{8\omega_n}\left\{\frac{9}{2}\alpha_3 + 2\alpha_2^2\Gamma_n[\Upsilon_1;\Upsilon_2]\right\} \tag{2.44}$$

and

$$\Gamma_n[\Upsilon_1;\Upsilon_2] = \int_0^1 [\Upsilon_1(x) + \Upsilon_2(x)]\phi_n^2(x)dx \tag{2.45}$$

Expressing the complex–valued function A_n in the polar form

$$A_n = \frac{1}{2}ae^{i(\sigma T_2 - \gamma)} \tag{2.46}$$

and separating Eq. (2.43) into its real and imaginary parts, we obtain

$$a' = -\mu a + \frac{f}{2\omega_n}\sin\gamma \tag{2.47}$$

$$a\gamma' = \sigma a - \alpha_e a^3 + \frac{f}{2\omega_n}\cos\gamma \tag{2.48}$$

Combining Eqs. (2.26), (2.33), (2.35), and (2.46), we express the deflection, to the second approximation, as

$$w(x,t) = \phi_n(x)a\cos(\Omega t - \gamma) + \frac{1}{4}\epsilon\alpha_2 a^2\left[2\Upsilon_2(x)\cos(2\Omega t - 2\gamma) + \Upsilon_1(x)\right] + ... \tag{2.49}$$

where a and γ are given by Eqs. (2.47) and (2.48). It follows from Eq. (2.49) that the drift is given by

$$d(x) = \frac{1}{4}\epsilon\alpha_2 a^2\Upsilon_1(x) + ... \tag{2.50}$$

An approximation to the nonlinear normal mode that reduces to the nth linear mode as the nonlinearity vanishes (i.e., $\epsilon \to 0$) can be obtained from Eqs. (2.49), (2.47), and (2.48) by setting $\mu = 0$ and $F(x) \equiv 0$ and replacing Ω with ω_n, a and γ with $a = a_0$ =constant, and $\gamma = -\epsilon^2 a_0^2\alpha_e t - \gamma_0$. The result is

$$\begin{aligned} W_n(x,t) = {} & \phi_n(x)a_0\cos[(\omega_n + \epsilon^2 a_0^2\alpha_e)t - \gamma_0] \\ & + \frac{1}{4}\epsilon\alpha_2 a^2\left[2\Upsilon_2(x)\cos[2(\omega_n + \epsilon^2 a_0^2\alpha_e)t - 2\gamma_0] + \Upsilon_1(x)\right] + ... \end{aligned} \tag{2.51}$$

It is evident that the discretization and direct approaches yield different approximate motions. The spatial distributions of the motion as well as the effective nonlinearity coefficient are different. Equation (2.44) shows clearly that the effective nonlinearity coefficient depends on the overall spatial dependence of the motion.

In Fig. 2.1 we show the spatial distribution of $w(x)$ for the first, second, and third modes as obtained by the direct and discretization approaches. For the chosen values of a and α_2, both techniques lead to the same distribution for the first mode, whereas the distributions are slightly shifted and differ in amplitude for the higher modes.

2.3.3 Periodic Solutions

Discretization approach

Periodic solutions of the system correspond to the fixed points of Eqs. (2.21) and (2.22); that is,

$$\mu a = \frac{f}{2\Omega}\sin\gamma \tag{2.52}$$

$$\sigma a = \tilde{\alpha}_e a^3 - \frac{f}{2\Omega}\cos\gamma \tag{2.53}$$

Eliminating γ from Eqs. (2.52) and (2.53) and solving the resulting equation for σ in terms of a, we obtain the *frequency–response equation*

$$\sigma = \tilde{\alpha}_e a^2 \pm \left(\frac{f^2}{4\Omega^2 a^2} - \mu^2\right)^{\frac{1}{2}} \tag{2.54}$$

It follows from Eq. (2.54) that the *backbone curve* is given by the parabola

$$\sigma = \tilde{\alpha}_e a^2 \tag{2.55}$$

Hence, $\tilde{\alpha}_e$ determines the extent of bending of the resonance curves. When $\tilde{\alpha}_e > 0$, the frequency–response curves are bent to the right and the effective nonlinearity is of the hardening type. When $\tilde{\alpha}_e < 0$, the frequency–response curves are bent to the left and the effective nonlinearity is of the softening type. And when $\tilde{\alpha}_e = 0$, the frequency–response curves are neither bent to the right nor to the left and, to the second approximation, the response of the system is linear. It follows from Eq. (2.23) that the quadratic nonlinearity has a softening effect, irrespective of the sign of α_2 as long as $\delta \neq 0$. When α_3 is positive, the effective nonlinearity $\tilde{\alpha}_e$ may be positive or negative depending on the relative magnitudes of α_3 and α_2. For even modes, $\delta = 0$ and the nonlinearity is of the hardening type. For odd modes, $\delta \neq 0$ and $\tilde{\alpha}_e = 0$ describes a curve in the $\alpha_2 - \alpha_3$ plane, which we refer to as the *transition curve* that separates softening from hardening behavior. This curve is given by

$$\alpha_3 - \frac{20\delta_n^2\alpha_2^2}{27\Omega^2} = 0 \tag{2.56}$$

Direct approach

Periodic solutions of the original system correspond to solutions of

$$\mu a = \frac{f}{2\omega_n}\sin\gamma \tag{2.57}$$

$$\sigma a = \alpha_e a^3 - \frac{f}{2\omega_n}\cos\gamma \tag{2.58}$$

The *frequency–response equation* and the *backbone curve* are given by

$$\sigma = \alpha_e a^2 \pm \left(\frac{f^2}{4\omega_n^2 a^2} - \mu^2\right)^{\frac{1}{2}} \tag{2.59}$$

$$\sigma = \alpha_e a^2 \tag{2.60}$$

Table 2.1: The Coefficients of $-\alpha_2^2$ in Eqs. (2.23) and (2.44) for the First Six Modes

n	Discretization Approach	Direct Approach
1	0.04931136	0.04935607
3	0.00006764	0.03527747
4	0	0.03440494
5	0.00000316	0.03400331
6	0	0.03380668

When $\alpha_3 > 0$, it follows from Eq. (2.44) that the *transition curve* in the $\alpha_2 - \alpha_3$ plane separating softening from hardening behavior is given by

$$\alpha_3 + \frac{4}{9}\alpha_2^2\Gamma_n = 0 \tag{2.61}$$

In Table 2.1, we list the coefficients of $-\alpha_2^2$ in Eqs. (2.23) and (2.44). In Fig. 2.2(a–c) we contrast the transition curves obtained by the discretization and direct approaches for the first three modes. Figure 2.2(a) shows that both approaches yield the same result for the first mode to a remarkably good accuracy. Figure 2.2(b) portrays the transition curve predicted by the direct approach for the second mode. It is evident from Fig. 2.2(c) that the *softening region* predicted by the discretization approach is negligible compared to that predicted by the direct approach. Because the coefficients of α_2^2 in Eqs. (2.23) and (2.44) tend to zero as $n \to \infty$, the system exhibits a hardening–type behavior for large n, irrespective of the value of the coefficient of the quadratic nonlinearity. However, the rate of decay of the coefficient of α_2^2 with n predicted by the discretization approach is much faster than that predicted by the direct approach.

In Fig. 2.3, we show the frequency–response curves calculated for the first, second, and third modes. For each externally resonant mode, we show variation of the frequency–response curves with α_2 for a fixed value of α_3 so that the transition curve is crossed in the

$\alpha_2 - \alpha_3$ plane and a switching from hardening– to softening–type behavior occurs.

In Fig. 2.3(a–c), the frequency–response curves obtained with the two approaches agree to a remarkably good accuracy. It is clear from Fig. 2.3(d–f) that the discretization treatment predicts hardening–type responses, irrespective of the value of the quadratic coefficient, whereas the direct approach predicts hardening–, linear–, or softening–type responses, depending on the location of the nonlinearity coefficients in the $\alpha_2 - \alpha_3$ plane with respect to the transition curve. We also observe from Fig. 2.3(d) that, although the two approaches predict qualitatively similar results, they do differ quantitatively. A similar behavior is shown in Fig. 2.3(g–i) for the third mode with the difference being that the bending of the frequency–response curves predicted by discretization varies with α_2. Nevertheless, they practically do not show a softening behavior because the region of softening responses is characterized by extremely small values of α_3 and large values of α_2, as shown in Fig. 2.2(c).

2.4 Subharmonic Resonance of Order One–Half of the nth Mode

To express the nearness of the excitation frequency to twice the natural frequency of the nth mode, we introduce a detuning parameter σ defined by $\Omega = 2\omega_n + \epsilon^2\sigma$ so that

$$\omega_n^2 = \frac{1}{4}\Omega^2 - \frac{1}{2}\epsilon^2\sigma\Omega + ... \tag{2.62}$$

2.4.1 Attacking the Discretized Equation

For the case of subharmonic resonance, we scale f as ϵf in order that the effect of the nonlinearity and damping balance the effect of the resonance. Next, using Eq. (2.62), we rewrite Eq. (2.5) as

$$\ddot{q} + \frac{1}{4}\Omega^2 q + \epsilon\delta\alpha_2 q^2 - \frac{1}{2}\epsilon^2\sigma\Omega q + \frac{3}{2}\epsilon^2\alpha_3 q^3 + 2\epsilon^2\mu\dot{q} + ... = \epsilon f\cos(\Omega t) \tag{2.63}$$

To determine a second–order uniform expansion of the solution of Eq. (2.63) by using the method of multiple scales, we use the two time scales T_0 and T_2 and expand the time–dependent variable q in powers of ϵ as in Eq. (2.11). Substituting Eqs. (2.11) and (2.10) into Eq. (2.63) and equating coefficients of like powers of ϵ yields

Order ϵ^0:

$$\mathcal{S}(q_0) = D_0^2 q_0 + \frac{1}{4}\Omega^2 q_0 = 0 \tag{2.64}$$

Order ϵ^1:

$$\mathcal{S}(q_1) = -\delta\alpha_2 q_0^2 + f\cos(\Omega T_0) \tag{2.65}$$

Order ϵ^2:

$$\mathcal{S}(q_2) = -2D_0 D_2 q_0 - 2\mu D_0 q_0 + \frac{1}{2}\sigma\Omega q_0 - 2\delta\alpha_2 q_0 q_1 - \frac{3}{2}\alpha_3 q_0^3 \tag{2.66}$$

The solution of Eq. (2.64) can be written as

$$q_0 = A(T_2)e^{\frac{1}{2}i\Omega T_0} + cc \tag{2.67}$$

Substituting Eq. (2.67) into Eq. (2.65) yields

$$\mathcal{S}(q_1) = -\delta\alpha_2[A^2 e^{i\Omega T_0} + A\overline{A}] + \frac{1}{2}f e^{i\Omega T_0} + cc \tag{2.68}$$

whose particular solution can be written as

$$q_1 = \left(\frac{4\delta\alpha_2}{3\Omega^2}A^2 - \frac{2f}{3\Omega^2}\right)e^{i\Omega T_0} - \frac{4\delta\alpha_2}{\Omega^2}A\overline{A} + cc \tag{2.69}$$

Substituting Eqs. (2.67) and (2.69) into Eq. (2.66) and eliminating the terms that lead to secular terms in q_2, we obtain

$$i\Omega(A' + \mu A) = \frac{1}{2}\sigma\Omega A - \left(\frac{9}{2}\alpha_3 - \frac{40\delta^2\alpha_2^2}{3\Omega^2}\right)A^2\overline{A} + \frac{4\delta\alpha_2 f}{3\Omega^2}\bar{A} \tag{2.70}$$

Substituting Eq. (2.20) into Eq. (2.70) and separating the result into its real and imaginary parts leads to

$$a' = -\mu a + \frac{4\delta\alpha_2 f}{3\Omega^3}a\sin 2\gamma \tag{2.71}$$

$$a\gamma' = \frac{1}{2}\sigma a - \hat{\alpha}_e a^3 + \frac{4\delta\alpha_2 f}{3\Omega^3}a\cos 2\gamma \tag{2.72}$$

where

$$\hat{\alpha}_e = \frac{27\alpha_3\Omega^2 - 80\delta^2\alpha_2^2}{24\Omega^3} \tag{2.73}$$

We observe that when n is even, $\delta_n = 0$ and hence the terms producing the activation of the subharmonic resonance vanish from Eqs. (2.71) and (2.72). Consequently, the amplitude a decays exponentially with time and the system response consists of the particular solution only.

Combining Eqs. (2.4), (2.11), (2.67), (2.69), and (2.20), we express the deflection, to the second approximation, as

$$w(x,t) = \phi_n(x)\left\{a\cos(\frac{1}{2}\Omega t - \gamma) + \epsilon\left[\frac{2\delta\alpha_2}{3\Omega^2}a^2\cos(\Omega t - 2\gamma) - \frac{2\delta\alpha_2}{\Omega^2}a^2 - \frac{4f}{3\Omega^2}\cos(\Omega t)\right] + ...\right\} \tag{2.74}$$

It follows from Eq. (2.74) that the drift is given by

$$\hat{s}(x) = -2\epsilon\frac{\delta\alpha_2}{\Omega^2}a^2\phi_n(x) + ... \tag{2.75}$$

2.4.2 Attacking Directly the Original Equations

In this section, we apply the method of multiple scales directly to Eqs. (2.1) and (2.2) and seek a second–order uniform solution in the form of Eq. (2.26). Moreover, we scale the forcing term *F(x)* as $\epsilon F(x)$. Then, substituting Eqs. (2.26) and (2.10) into Eqs. (2.1) and (2.2) and equating coefficients of like powers of ϵ, we obtain

Order ϵ^0:

$$\mathcal{M}(w_0) = 0 \tag{2.76}$$

Order ϵ^1:

$$\mathcal{M}(w_1) = -\alpha_2 w_0^2 + F(x)\cos(\Omega T_0) \tag{2.77}$$

Order ϵ^2:

$$\mathcal{M}(w_2) = -2\frac{\partial^2 w_0}{\partial T_0 T_2} - 2\mu\frac{\partial w_0}{\partial T_0} - 2\alpha_2 w_0 w_1 - \alpha_3 w_0^3 \tag{2.78}$$

The boundary conditions at the various orders are given by Eq. (2.30).

Using arguments similar to those used in Section 2.3.2, we can write the solution of Eqs. (2.76) and (2.30) as in Eq. (2.33). Substituting Eq. (2.33) into Eq. (2.77) yields

$$\mathcal{M}(w_1) = -\alpha_2\phi_n^2(x)[A_n^2 e^{2i\omega_n T_0} + A_n\overline{A}_n] + \frac{1}{2}F(x)e^{i\Omega T_0} + cc \tag{2.79}$$

The solution of Eqs. (2.79) and (2.30) can be expressed as

$$w_1(x, T_0, T_2) = \frac{1}{2}\alpha_2\Upsilon_1(x)A_n\overline{A}_n + \alpha_2\Upsilon_2(x)A_n^2 e^{2i\omega_n T_0} + \frac{1}{2}\mathcal{F}(x)e^{i\Omega T_0} + cc \tag{2.80}$$

where $\Upsilon_1(x)$ and $\Upsilon_2(x)$ are given by Eqs. (2.40) and (2.41), respectively, and $\mathcal{F}(x)$ is the solution of the following nonhomogeneous boundary–value problem:

$$L(\mathcal{F};\Omega) = F(x) \tag{2.81}$$

$$\mathcal{F} = 0 \text{ and } \mathcal{F}'' = 0 \text{ at } x = 0 \text{ and } 1 \tag{2.82}$$

When $F(x) = 1$, the solution can be expressed as

$$\begin{aligned}\mathcal{F}(x) \approx \frac{1}{8\omega_n^2}\Bigg\{ &-2 + \cos\gamma_n x + \cosh\gamma_n x + \left(\frac{1}{\cos\gamma_n} - \cot\gamma_n\right)\sin\gamma_n x \\ &+\left(\frac{1}{\cosh\gamma_n} - \coth\gamma_n\right)\sinh\gamma_n x\Bigg\}\end{aligned} \tag{2.83}$$

Substituting Eqs. (2.33) and (2.80) into Eq. (2.78), we obtain

$$\begin{aligned}\mathcal{M}(w_2) = -\Big\{ &2i\omega_n(A_n' + \mu A_n)\phi_n(x) \\ &+ \Big[2\alpha_2^2\Big[\Upsilon_1(x) + \Upsilon_2(x)\Big]\phi_n(x) + 3\alpha_3\phi_n^3(x)\Big]A_n^2\bar{A}_n \\ &+ \alpha_2\mathcal{F}(x)\phi_n(x)\bar{A}_n e^{i\sigma T_2}\Big\}e^{i\omega_n T_0} + cc + NST\end{aligned} \tag{2.84}$$

The solvability condition for Eqs. (2.84) and (2.30) yields the modulation equation

$$2i\omega_n(A_n' + \mu A_n) + 8\omega_n\alpha_e A_n^2\overline{A}_n + \alpha_2 f_e\overline{A}_n e^{i\sigma T_2} = 0 \tag{2.85}$$

where α_e is defined in Eq. (2.44) and

$$f_e = \int_0^1 \mathcal{F}(x)\phi_n^2(x)dx \tag{2.86}$$

Expressing A_n in the polar form

$$A_n = \frac{1}{2}ae^{i(\frac{1}{2}\sigma T_2 - \gamma)} \tag{2.87}$$

and separating Eq. (2.85) into its real and imaginary parts, we obtain

$$a' = -\mu a - \frac{\alpha_2 f_e}{2\omega_n} a \sin 2\gamma \tag{2.88}$$

$$a\gamma' = \frac{1}{2}\sigma a - \alpha_e a^3 - \frac{\alpha_2 f_e}{2\omega_n} a \cos 2\gamma \tag{2.89}$$

Combining Eqs. (2.26), (2.33), (2.80), and (2.87), we express the deflection, to the second approximation, as

$$w(x,t) = \phi_n(x) a \cos(\frac{1}{2}\Omega t - \gamma) + \epsilon \Big\{ \phi(x) \cos(\Omega t) + \frac{1}{4}\alpha_2 a^2 \Big[2\Upsilon_2(x) \cos(\Omega t - 2\gamma) + \Upsilon_1(x) \Big] \Big\} + ... \tag{2.90}$$

where a and γ are given by Eqs. (2.88) and (2.89). It follows from Eq. (2.90) that the drift is given by Eq. (2.50).

2.4.3 Periodic Solutions

For the discretization approach, periodic solutions correspond to solutions of the following algebraic equations:

$$\mu a = \frac{4\delta\alpha_2 f}{3\Omega^3} a \sin 2\gamma \tag{2.91}$$

$$\frac{1}{2}\sigma a = \hat{\alpha}_e a^3 - \frac{4\delta\alpha_2 f}{3\Omega^3} a \cos 2\gamma \tag{2.92}$$

There are two possibilities: either $a = 0$ or

$$\mu^2 + (\frac{1}{2}\sigma - \hat{\alpha}_e a^2)^2 = \frac{16 f^2 \delta^2 \alpha_2^2}{9\Omega^6} \tag{2.93}$$

It follows from Eq. (2.93) and the fact that $\Omega \approx 2\omega_n$ that

$$\sigma = 2\hat{\alpha}_e a^2 \pm 2 \left(\frac{\delta^2 \alpha_2^2 f^2}{36\omega_n^6} - \mu^2 \right)^{\frac{1}{2}} \tag{2.94}$$

In order that Eq. (2.94) have real solutions, f must exceed the critical value

$$f_{cr} = \frac{6\omega_n^3 \mu}{\delta \alpha_2} \tag{2.95}$$

For the direct approach, periodic solutions correspond to solutions of

$$-\mu a = \frac{\alpha_2 f_e}{2\omega_n} a \sin 2\gamma \tag{2.96}$$

$$\frac{1}{2}\sigma a = \alpha_e a^3 + \alpha_2 \frac{f_e}{2\omega_n} a \cos 2\gamma \tag{2.97}$$

Again, there are two possibilities: either $a = 0$ or

$$\sigma = 2\alpha_e a^2 \pm 2\left(\alpha_2^2 \frac{f_e^2}{4\omega_n^2} - \mu^2\right)^{\frac{1}{2}} \tag{2.98}$$

The threshold level for the activation of the subharmonic resonance, in this case, is

$$f_{cr} = \frac{2\omega_n \mu}{\alpha_2} \tag{2.99}$$

In Fig. 2.4(a–f), we show typical frequency–response curves for the subharmonic resonance of the first (a,b), second (c,d), and third (e,f) modes. A general feature of these curves is the presence of a trivial branch and the nontermination of the nontrivial branches. The frequency–response curves are plotted by keeping α_3 fixed and varying α_2. As in the case of primary resonance, the first–mode responses obtained with both approaches agree, as shown in Fig. 2.4(a,b). In Fig. 2.4(c,d), we show the frequency–response curves obtained only with the direct treatment because the discretization approach does not predict the activation of the subharmonic response. It follows form Fig. 2.4(e,f) that the frequency–response curves for the third–mode predicted with discretization are narrower than those obtained by the direct treatment. This implies that the discretization approach can underestimate the range over which the subharmonic resonance is activated.

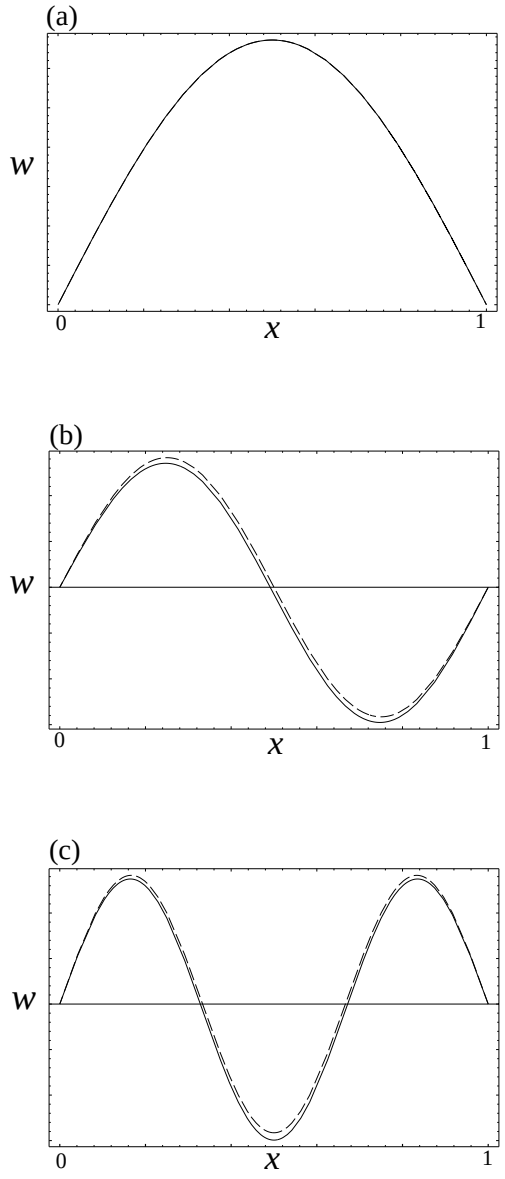

Figure 2.1: Spatial distribution of the displacement $w(x)$ in the case of primary resonance: (a) first mode; (b) second mode; and (c) third mode when $\epsilon = 1$, $\alpha_2 = 5$, and $a = 1$. Solid (dashed) lines denote the response obtained by the direct (discretization) approach.

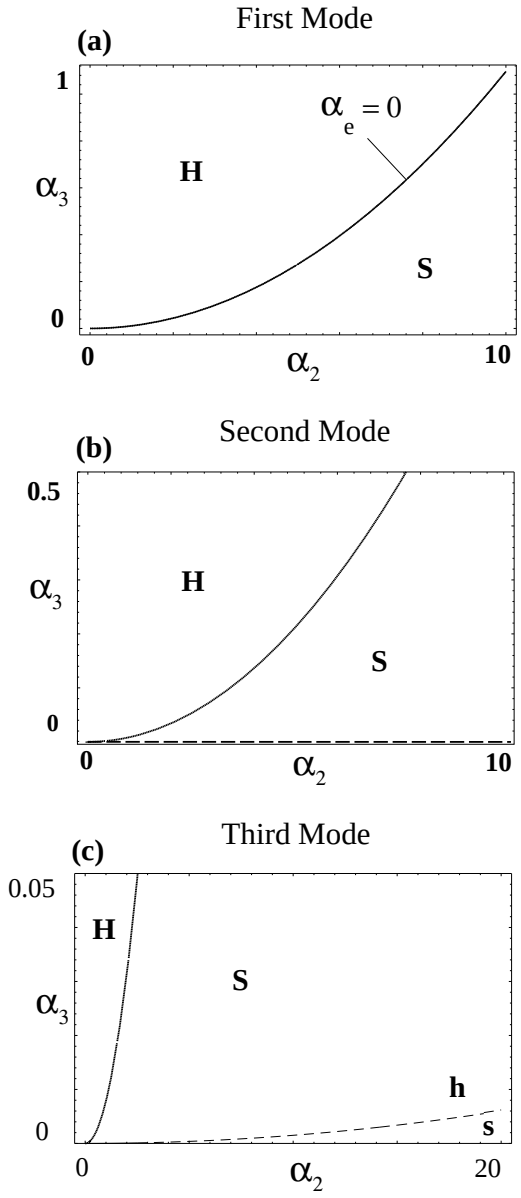

Figure 2.2: Transition curves separating softening and hardening behavior: (a) first mode, (b) second mode, and (c) third mode. Solid (dashed) lines denote direct (discretization) approach results: H (h) denotes the hardening region obtained with the direct (discretization) approach; S (s) denotes the softening region obtained with the direct (discretization) approach.

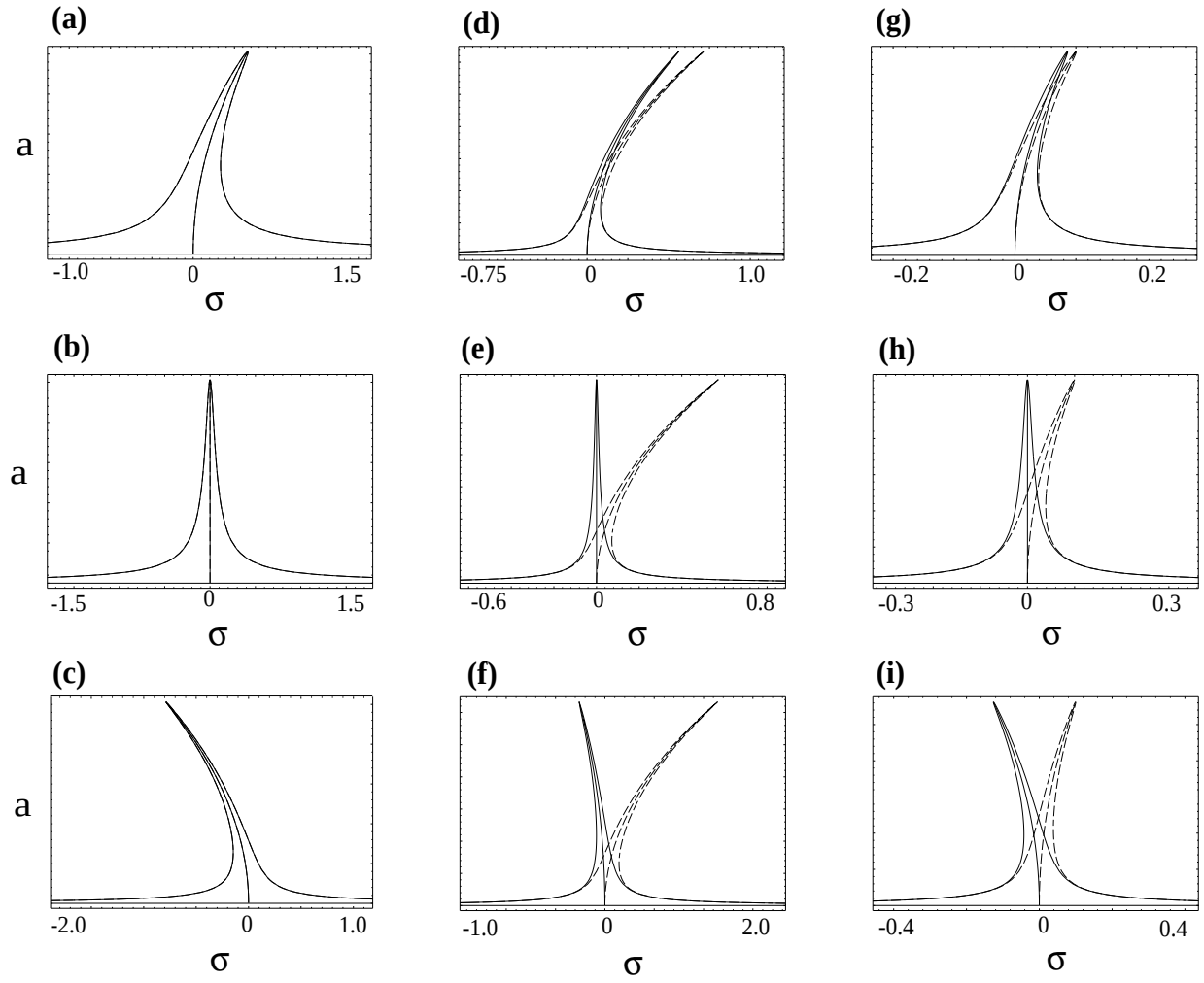

Figure 2.3: Frequency–response curves for the case of primary resonance: (a)–(c) first mode for $\mu = 0.05$, $\alpha_3 = 0.5$, and $f = 5$, (d)–(f) second mode for $\mu = 0.01$, $\alpha_3 = 1$, and $f = 5$, and (g)–(i) third mode for $\mu = 0.01$, $\alpha_3 = 0.5$, and $f = 10$. In these figures, the values of α_2 are: (a) $\alpha_2 = 5$, (b) $\alpha_2 = 6.755$, (c) $\alpha_2 = 12$, (d) $\alpha_2 = 5$, (e) $\alpha_2 = 10.827$, (f) $\alpha_2 = 12$, (g) $\alpha_2 = 3$, (h) $\alpha_2 = 7.986$, and (i) $\alpha_2 = 12$. Solid (dashed) lines denote direct (discretization) results.

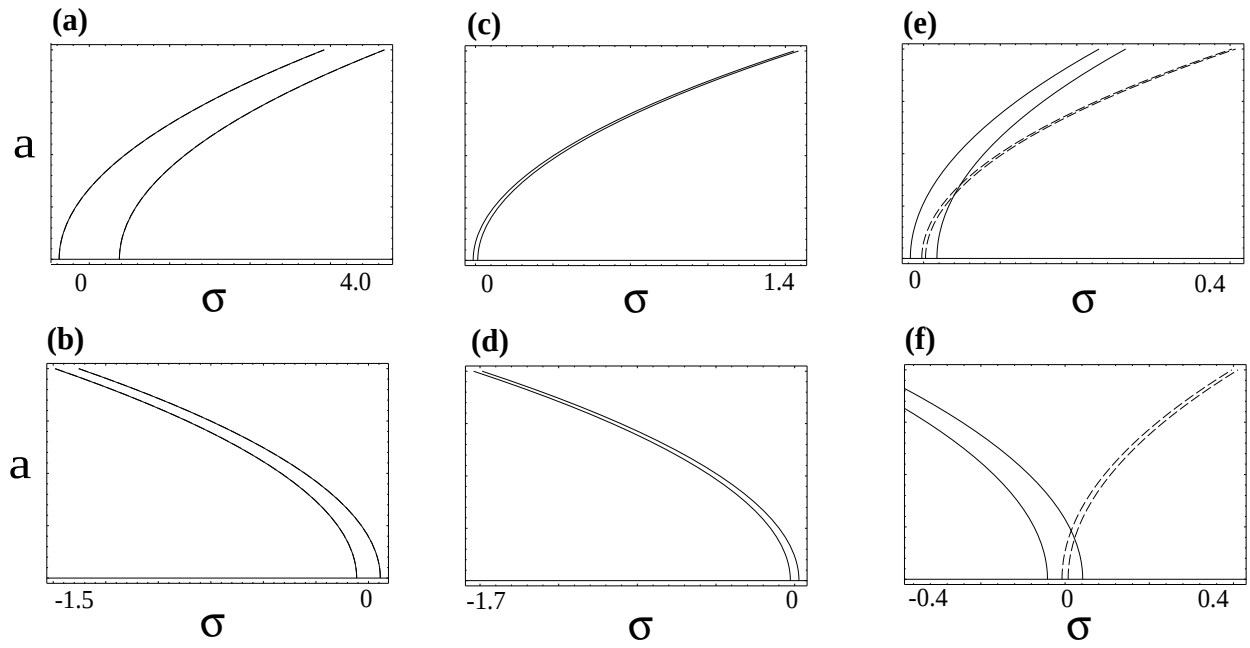

Figure 2.4: Frequency–response curves for the case of subharmonic resonance of order one–half for $\alpha_3 = 0.5$: (a) and (b) first mode, (c) and (d) second mode, and (e) and (f) third mode when (a) $\mu = 0.01$ and $\alpha_2 = 5$, (b) $\mu = 0.05$ and $\alpha_2 = 10$, (c) $\mu = 0.05$ and $\alpha_2 = 15$, (d) $\mu = 0.01$ and $\alpha_2 = 5$, (e) $\mu = 0.01$ and $\alpha_2 = 7.986$, and (f) $\mu = 0.01$ and $\alpha_2 = 12$. Solid (dashed) lines denote direct (discretization) results.

Chapter 3

Imperfect Buckled Beams

In this chapter, we derive the equations of motion governing moderately large finite–amplitude transverse vibrations of a homogeneous, isotropic, geometrically imperfect beam around an initial pre– or post–buckling equilibrium subject to a time–dependent end load and a distributed excitation. The elastic equilibrium is due to distributed transverse loads and/or end loads and/or distributed changes in temperature.

3.1 The Kinematic Model

We consider an Euler–Bernoulli beam with an initial geometric imperfection, undergoing moderately large transverse displacements. We note that the theory of planar, *geometrically imperfect* beams coincides with the theory of *shallow* arches. A geometrically imperfect beam is, in fact, a shallow arch because the rise–to–span ratio of the imperfect beam is assumed to be small. The theory of shallow arches is based on the following assumptions (Mettler, 1962): the shear deformation, longitudinal inertia, and rotary inertia are negli-

gible. The second assumption allows the elimination of the longitudinal degree of freedom by using a kinematic condensation condition.

We let $\hat{w}_0(\hat{x})$ be the beam initial geometric imperfection with respect to a Cartesian, inertial frame of reference, as shown in Fig. 3.1; and let $\hat{u}$ and $\hat{w}$ the displacement components along the x and z directions, respectively, where the hat designates dimensional variables. Following Mettler (1962), we express the engineering strain accounting for stretching of the midplane surface of the beam as

$$\epsilon_0 = \frac{\hat{ds}}{\hat{ds}_0} - 1 \tag{3.1}$$

where

$$\hat{ds}_0 = \sqrt{1 + \hat{w}_0'^2}d\hat{x} \quad \text{and} \quad \hat{ds} = \sqrt{(1 + \hat{u}')^2 + (\hat{w}_0' + \hat{w}')^2}d\hat{x}$$

represent the lengths of a line element of the centerline of the imperfect beam in the undeformed and deformed configurations, respectively. The prime denotes differentiation with respect to $\hat{x}$. Hence, Eq. (3.1) becomes

$$\epsilon_0 = \frac{\sqrt{(1 + \hat{u}')^2 + (\hat{w}_0' + \hat{w}')^2}}{\sqrt{1 + \hat{w}_0'^2}} - 1 \tag{3.2}$$

Next, we expand Eq. (3.2) to second order and obtain

$$\epsilon_0 = \hat{u}' + \hat{w_0}'\hat{w}' + \frac{1}{2}\hat{w}'^2 + ... \tag{3.3}$$

where $\hat{u}'^2$ is assumed to be small compared with $\hat{w}'^2$.

To account for bending effects, we consider the flexural strain field given by the Euler–Bernoulli beam theory

$$\epsilon_f(x) = -\xi\hat{w}''(\hat{x}) \tag{3.4}$$

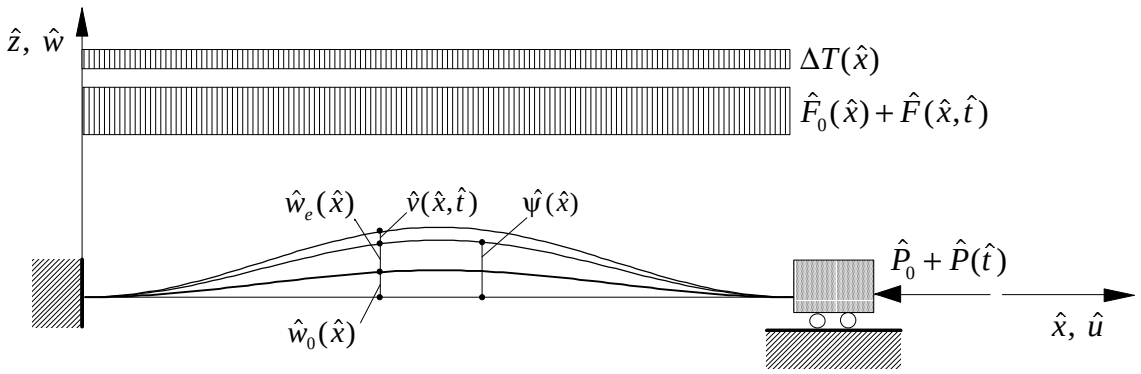

Figure 3.1: A schematic of an initially imperfect beam subject to an end load, a distributed transverse load, and a change in temperature.

where ξ measures the transverse distance from the neutral axis in the cross–section of the beam. Furthermore, the strain field due to linear thermoelastic effects is given by

$$\epsilon_t(x) = -\alpha \Delta T(\hat{x}) \tag{3.5}$$

where α is the coefficient of thermal expansion and $\Delta T(\hat{x})$ is the change in temperature distribution in the initial undeformed configuration. By summing the strains given by Eqs. (3.3), (3.4), and (3.5), we obtain the total strain to second order as

$$\epsilon = \hat{u}' + \hat{w_0}'\hat{w}' + \frac{1}{2}\hat{w}'^2 - \xi \hat{w}'' - \alpha \Delta T \tag{3.6}$$

3.2 Equations of Motion

The total potential energy can be written as

$$V = \frac{1}{2}\int_0^\ell \int_A E\epsilon^2 dA d\hat{x} - \int_0^\ell \hat{F}_0 \hat{w} d\hat{x} + \hat{P}_0 \hat{u}(\ell, \hat{t}) \tag{3.7}$$

where ℓ is the span of the beam, A is its cross–sectional area, E is Young's modulus, $\hat{F}_0$ is a static transverse distributed load, and $\hat{P}_0$ is a static end load applied at $\hat{x} = \ell$. We assume that the end load is positive if it is compressive.

Substituting Eq. (3.6) into Eq. (3.7) and performing the integration, we obtain

$$V = \frac{1}{2}EA\int_0^\ell \epsilon_s^2 d\hat{x} + \frac{1}{2}EI\int_0^\ell (\hat{w}'')^2 d\hat{x} - \int_0^\ell \hat{F}_0 \hat{w} d\hat{x} + \hat{P}_0 \hat{u}(\ell, \hat{t}) \tag{3.8}$$

where I denotes the moment of inertia of the cross–section of the beam and

$$\epsilon_s = \hat{u}' + \hat{w_0}'\hat{w}' + \frac{1}{2}\hat{w}'^2 - \alpha \Delta T \tag{3.9}$$

represents the total stretching strain of the centerline of the beam. The kinetic energy can be expressed as

$$T = \frac{1}{2}\int_0^\ell m(\dot{\hat{u}}^2 + \dot{\hat{w}}^2) d\hat{x} \tag{3.10}$$

where m is the distributed mass per unit length of the beam and the overdot denotes differentiation with respect to $\hat{t}$.

Hamilton's extended principle can be written as

$$\delta \int_{\hat{t}_1}^{\hat{t}_2} (T - V) d\hat{t} + \int_{\hat{t}_1}^{\hat{t}_2} \int_0^{\ell} \left[\hat{F}(\hat{x}, \hat{t}) + \hat{c}\dot{\hat{w}} \right] \delta \hat{w} d\hat{t} + \int_{\hat{t}_1}^{\hat{t}_2} \hat{P}(\hat{t}) \delta \hat{u}(\ell, \hat{t}) d\hat{t} = 0 \tag{3.11}$$

where $\hat{c}$ is the coefficient of viscous damping, $\hat{F}(\hat{x}, \hat{t})$ is a nonconservative transverse distributed load, and $\hat{P}(\hat{t})$ is a time–dependent load applied at $\hat{x} = \ell$. Substituting Eqs. (3.8)–(3.10) into Eq. (3.11) and performing the pertinent variations and integrations yields the following two nonlinear coupled integro–partial–differential equations:

$$m\ddot{\hat{u}} - EA\epsilon_s' = 0 \tag{3.12}$$

$$m\ddot{\hat{w}} + EI\hat{w}^{iv} - EA\Big[\epsilon_s(\hat{w}_0' + \hat{w}')\Big]' + \hat{c}\dot{\hat{w}} = \hat{F}_0 + \hat{F}(\hat{x}, \hat{t}) \tag{3.13}$$

Neglecting the longitudinal inertia, we reduce Eq. (3.12) to

$$\epsilon_s' = 0 \tag{3.14}$$

which implies that the total stretching strain field along the centerline of the beam is constant. Hence, using Eq. (3.14), assuming $\hat{u}(0) = 0$, and integrating Eq. (3.9) from $\hat{x} = 0$ to $\hat{x} = \ell$, we obtain

$$\begin{aligned} \epsilon_s = \frac{1}{\ell} \int_0^{\ell} \Big[\hat{u}' + \hat{w_0}'\hat{w}' + \frac{1}{2}\hat{w}'^2 - \alpha\Delta T \Big] d\hat{x} = \\ \frac{\hat{u}(\ell, \hat{t})}{\ell} - \frac{\hat{u}_t}{\ell} + \frac{1}{\ell} \int_0^{\ell} \Big[\hat{w_0}'\hat{w}' + \frac{1}{2}\hat{w}'^2 \Big] d\hat{x} \end{aligned} \tag{3.15}$$

where

$$\hat{u}_t = \int_0^{\ell} \alpha\Delta T d\hat{x}$$

and $\hat{u}(\ell, \hat{t})$ represents the horizontal displacement at $\hat{x} = \ell$.

Making use of Eq. (3.15) and taking into account the boundary condition at $\hat{x} = \ell$, we rewrite Eq. (3.13) as

$$m\ddot{\hat{w}} + EI\hat{w}^{iv} + \hat{c}\dot{\hat{w}} + \frac{EA}{\ell}(\hat{w_0}'' + \hat{w}'')\left[\frac{\ell}{EA}\left(\hat{P}_0 + \hat{P}(\hat{t})\right) + \hat{u}_t - \frac{1}{2}\int_0^\ell (\hat{w}'^2 + 2\hat{w_0}'\hat{w}')d\hat{x}\right] = \hat{F}_0 + \hat{F}(\hat{x},\hat{t}) \tag{3.16}$$

or

$$m\ddot{\hat{w}} + EI\hat{w}^{iv} + \hat{c}\dot{\hat{w}} - \frac{EA}{\ell}(\hat{w_0}'' + \hat{w}'')\left[\hat{u}(\ell,\hat{t}) - \hat{u}_t + \frac{1}{2}\int_0^\ell (\hat{w}'^2 + 2\hat{w_0}'\hat{w}')d\hat{x}\right] = \hat{F}_0 + \hat{F}(\hat{x},\hat{t}) \tag{3.17}$$

depending on whether the boundary at $\hat{x} = \ell$ is subjected to an end load or to an imposed displacement. In the following, we consider the case of an applied end load.

By dropping the time derivatives and the dynamic loads in Eq. (3.16), we obtain the following equation governing the nonlinear equilibrium of the beam:

$$EI\hat{w_e}^{iv} + \frac{EA}{\ell}(\hat{w_0}'' + \hat{w_e}'')\left[\frac{\hat{P}_0\ell}{EA} + \hat{u}_t - \frac{1}{2}\int_0^\ell (\hat{w_e}'^2 + 2\hat{w_0}'\hat{w_e}')d\hat{x}\right] = \hat{F}_0 \tag{3.18}$$

To obtain the equation governing transverse vibrations around the nonlinear equilibrium $\hat{w}_e(\hat{x})$, we let

$$\hat{w}(\hat{x},\hat{t}) = \hat{w}_e(\hat{x}) + \hat{v}(\hat{x},\hat{t}) \tag{3.19}$$

where $\hat{v}(\hat{x},\hat{t})$ represents the dynamic deflection. Substituting Eq. (3.19) into Eq. (3.16) and taking into account Eq. (3.18) yields

$$\begin{aligned} m\ddot{\hat{v}} + EI\hat{v}^{iv} + \hat{c}\dot{\hat{v}} + \frac{EA}{\ell}\hat{v}''\left[\frac{\ell}{EA}\left(\hat{P}_0 + \hat{P}(\hat{t})\right) + \hat{u}_t - \frac{1}{2}\int_0^\ell (\hat{w}_e'^2 + 2\hat{w_0}'\hat{w}_e')d\hat{x}\right] \\ -\frac{EA}{\ell}(\hat{w_0}'' + \hat{w_e}'')\int_0^\ell \hat{v}'(\hat{w_0}' + \hat{w_e}')d\hat{x} - \frac{EA}{2\ell}(\hat{w_0}'' + \hat{w_e}'')\int_0^\ell \hat{v}'^2 d\hat{x} \\ -\frac{EA}{2\ell}\hat{v}''\int_0^\ell \left[\hat{v}'^2 + 2\hat{v}'(\hat{w_0}' + \hat{w_e}')\right]d\hat{x} = \hat{F}(\hat{x},\hat{t}) - \left(\hat{w_0}'' + \hat{w_e}''\right)\hat{P}(\hat{t}) \end{aligned} \tag{3.20}$$

If we let

$$\hat{\psi}(\hat{x}) = \hat{w}_e(\hat{x}) + \hat{w}_0(\hat{x}) \tag{3.21}$$

Equations (3.18) and (3.20) become, respectively,

$$EI\hat{\psi}^{iv} + \frac{EA}{\ell}\hat{\psi}''\left[\frac{\hat{P}_0\ell}{EA} + \hat{u}_t + \frac{1}{2}\int_0^\ell (\hat{w}_0'^2 - \hat{\psi}'^2)d\hat{x}\right] = \hat{F}_0 + EI\hat{w}_0^{iv} \tag{3.22}$$

$$\begin{aligned} m\ddot{\hat{v}} + EI\hat{v}^{iv} + \hat{c}\dot{\hat{v}} + \frac{EA}{\ell}\hat{v}''\left[\frac{\ell}{EA}\left(\hat{P}_0 + \hat{P}(\hat{t})\right) + \hat{u}_t + \frac{1}{2}\int_0^\ell (\hat{w}_0'^2 - \hat{\psi}'^2)d\hat{x}\right] \\ -\frac{EA}{\ell}\hat{\psi}''\int_0^\ell \hat{v}'\hat{\psi}'d\hat{x} - \frac{EA}{\ell}\hat{v}''\int_0^\ell \hat{v}'\hat{\psi}'d\hat{x} - \frac{EA}{2\ell}\hat{\psi}''\int_0^\ell \hat{v}'^2 d\hat{x} \\ -\frac{EA}{2\ell}\hat{v}''\int_0^\ell \hat{v}'^2 d\hat{x} = \hat{F}(\hat{x},\hat{t}) - \hat{\psi}''\hat{P}(\hat{t}) \end{aligned} \tag{3.23}$$

3.3 Nondimensionalization

We nondimensionalize the spatial and temporal variables by letting

$$x = \frac{\hat{x}}{\ell},\ \ w_0 = \frac{\hat{w}_0}{r},\ \ \psi = \frac{\hat{\psi}}{r},\ \ v = \frac{\hat{v}}{r},\ \ t = \hat{t}\sqrt{\frac{EI}{m\ell^4}},\ \ \Omega = \hat{\Omega}\sqrt{\frac{m\ell^4}{EI}} \tag{3.24}$$

where r $(=\sqrt{I/A})$ denotes the radius of gyration of the cross-section and $\hat{\Omega}$ is the dimensional external excitation frequency. This nondimensionalization produces the simplest nondimensional form of Eqs. (3.22) and (3.23), namely

$$\psi^{iv} + \psi''\left[P_0 + \frac{1}{2}\int_0^1 (w_0'^2 - \psi'^2)dx\right] = F_0 + w_0^{iv} \tag{3.25}$$

$$\begin{aligned} \ddot{v} + v^{iv} + c\dot{v} + v''\left[P_0 + P(t) + \frac{1}{2}\int_0^1 (w_0'^2 - \psi'^2)dx\right] - \psi''\int_0^1 v'\psi' dx \\ -v''\int_0^1 v'\psi' dx - \frac{1}{2}\psi''\int_0^1 v'^2 dx - \frac{1}{2}v''\int_0^1 v'^2 dx = F(x,t) - P(t)\psi'' \end{aligned} \tag{3.26}$$

where

$$P_0 = \Big(\frac{\hat{P}_0}{EA} + \frac{\hat{u}_t}{\ell}\Big)\varrho^2, \quad P(t) = \frac{\hat{P}(\hat{t})}{EA}\varrho^2, \quad \varrho = \frac{\ell}{r}, \quad c = \frac{\hat{c}\ell^2}{\sqrt{mEI}}, \quad F_0 = \frac{\hat{F}_0\ell^4}{rEI} \tag{3.27}$$

We note that the nondimensional parameter ϱ is a measure of the slenderness of the beam. Hence, it follows from Eqs. (3.25)–(3.27) that the effects of the end load and the distributed change in temperature are significant for slender beams.

Chapter 4

Post–Buckling Behavior

A mixed analytical–numerical procedure is used to determine the equilibrium solutions in the pre– and post–buckling ranges of an initially imperfect beam. The boundary conditions are assumed to be clamped–clamped. We show that, depending on the initial shape, more than two stable equilibrium configurations are admissible. We find null–load solutions or everted equilibrium states in the absence of external loads and/or other sources of inhomogeneities for initial imperfections exceeding a threshold value.

4.1 Analysis

To study the nonlinear equilibria of the beam, we seek solutions of Eq. (3.25); that is,

$$\psi^{iv} + \psi''\Big[P_0 + \frac{1}{2}\int_0^1 (w_0'^2 - \psi'^2)dx\Big] = F_0 + w_0^{iv} \tag{4.1}$$

Without loss of generality, we consider the linear homogeneous boundary conditions

$$B_{11}[\psi] = B_{12}[\psi] = 0 \ \text{ at } \ x = 0 \ \text{ and } \ B_{21}[\psi] = B_{22}[\psi] = 0 \ \text{ at } \ x = 1 \tag{4.2}$$

where the B_{ij} represent linear boundary differential operators.

We observe, following Nayfeh, Kreider, and Anderson (1995) and Johnson and Plaut (1980), that the integral term appearing in Eq. (4.1) can be treated as a constant term. Hence, we let

$$\lambda^2 = P_0 + \frac{1}{2}\int_0^1 (w_0'^2 - \psi'^2)dx \tag{4.3}$$

and rewrite Eq. (4.1) as

$$\psi^{iv} + \lambda^2\psi'' = F_0 + w_0^{iv} \tag{4.4}$$

The general solution of Eq. (4.4) consists of the superposition of the homogeneous solution and a particular solution. The homogeneous solution can be written as

$$\psi_h = a_1 + a_2 x + a_3 \cos\lambda x + a_4 \sin\lambda x \tag{4.5}$$

We observe that the particular solution depends on the eigenvalue λ, the initial imperfection $w_0(x)$, and the applied distributed load $F_0(x)$; that is,

$$\psi_p = \psi(x; \lambda, w_0, F_0) \tag{4.6}$$

Hence, the general solution of Eq. (4.4) can be written as

$$\psi(x;\lambda) = a_1 + a_2 x + a_3 \cos\lambda x + a_4 \sin\lambda x + \psi_p(x; \lambda, w_0, F_0) \tag{4.7}$$

To determine the arbitrary constants a_i, we enforce the boundary conditions given by Eq. (4.2). Because the boundary operators are linear,

$$\begin{aligned}
B_{11}[\psi_h]|_{x=0} &= -B_{11}[\psi_p]|_{x=0} \\
B_{12}[\psi_h]|_{x=0} &= -B_{12}[\psi_p]|_{x=0} \\
B_{21}[\psi_h]|_{x=1} &= -B_{21}[\psi_p]|_{x=1} \\
B_{22}[\psi_h]|_{x=1} &= -B_{22}[\psi_p]|_{x=1}
\end{aligned} \tag{4.8}$$

If the boundary conditions are independent, then Eq. (4.8) admits a unique solution. Then, we substitute for the a_i in Eq. (4.3) and obtain the following nonlinear equation for λ:

$$H(\lambda, w_0, F_0, P_0) = \lambda^2 + \frac{1}{2}\int_0^1 \left(\frac{d\psi(x;\lambda, w_0, F_0)}{dx}\right)^2 dx - P_0 - \frac{1}{2}\int_0^1 \left(\frac{dw_0}{dx}\right)^2 dx = 0 \quad (4.9)$$

Substituting the solutions of Eqs. (4.8) and (4.9) into Eq. (4.7), we uniquely determine the equilibrium solutions. In general, Eq. (4.9) yields one or more roots, depending, for a given beam, on the geometric imperfection w_0, the distributed load F_0, the end load P_0, and the distributed change in temperature ΔT. The single root corresponds to the stable elastic pre–buckling solution, whereas the multiple roots correspond to the multiple post–buckling equilibria.

4.2 Clamped–Clamped Imperfect Beams

To investigate the equilibria in the absence of distributed loads, we seek solutions of Eq. (4.1) when $F_0 = 0$. For clamped–clamped beams, the boundary conditions are given by

$$\psi = \psi' = 0 \ \text{ at } \ x = 0 \ \text{ and } \ 1 \quad (4.10)$$

Hence, Eq. (4.8) becomes

$$a_1 + a_3 = -\psi_p(0)$$

$$a_2 + \lambda a_4 = -\psi_p'(0)$$

$$a_1 + a_2 + a_3\cos\lambda + a_4\sin\lambda = -\psi_p(1)$$

$$a_2 - a_3\lambda\sin\lambda + a_4\lambda\cos\lambda = -\psi_p'(1) \quad (4.11)$$

Next, we assume an initial geometric imperfection of the form

$$w_0(x) = \frac{1}{2}a(1 - \cos 2\pi x) \tag{4.12}$$

Then, the particular solution of Eq. (4.4) with $F_0 = 0$ can be expressed as

$$\psi_p = \frac{2\pi^2 a}{\lambda^2 - 4\pi^2} \cos 2\pi x \tag{4.13}$$

Substituting Eq. (4.13) into Eq. (4.11) and solving the resulting equations, we obtain

$$a_2 = a_3 = a_4 = 0, \quad a_1 = \frac{2\pi^2 a}{4\pi^2 - \lambda^2} \tag{4.14}$$

Hence, the solution can be expressed as

$$\psi = \frac{2\pi^2 a}{4\pi^2 - \lambda^2}(1 - \cos 2\pi x) \tag{4.15}$$

Substituting Eqs. (4.12) and (4.15) into Eq. (4.9), we obtain the following characteristic equation for λ:

$$H(\lambda, a, P_0) = \lambda^2 - \frac{\pi^2 a^2 \lambda^2 (\lambda^2 - 8\pi^2)}{4(\lambda^2 - 4\pi^2)^2} - P_0 = 0 \tag{4.16}$$

Instead of solving the algebraic equation (4.16), we can determine the solution of Eqs. (4.1) and (4.10) when w_0 is given by Eq. (4.12) in a different fashion. Guided by Eq. (4.15), we express the post–buckling solution as

$$\psi = \frac{1}{2}b\Big(1 - \cos 2\pi x\Big) \tag{4.17}$$

where b is determined by requiring that Eq. (4.17) satisfy Eq. (4.1) with $F_0 = 0$. The result is

$$b^3 - \left(\frac{4}{\pi^2}P_0 + a^2 - 16\right)b - 16a = 0 \tag{4.18}$$

Buckling occurs when two roots of Eq. (4.18) coalesce. This condition is satisfied if the discriminant of Eq. (4.18) is zero. That is,

$$\left(16 - a^2 - \frac{4}{\pi^2}P_0\right)^3 + 1728a^2 = 0 \tag{4.19}$$

Solving this equation for P_0, we obtain the buckling load

$$P_c = 4\pi^2 + \pi^2\left(3a^{\frac{2}{3}} - \frac{a^2}{4}\right) \tag{4.20}$$

In Fig. 4.1, we show variation of the buckling amplitude with the nondimensional end load for three different values of the amplitude of the initial imperfection. When $a = 0$, the bifurcation diagram is symmetric; at $P_0 = 4\pi^2$, the trivial equilibrium undergoes a pitchfork bifurcation and the beam may buckle. On the other hand, when $a \neq 0$, the symmetry of the bifurcation is lost and buckling occurs for P_c given by Eq. (4.20) through a saddle–node bifurcation. It is clear that the buckling bifurcation of a straight beam is structurally unstable and this has significant consequences on its dynamic behavior in the pre– and post–buckling ranges, as we show in the next chapter.

In Fig. 4.2, we show variation of the lowest critical nondimensional load, given by Eq. (4.20), with the nondimensional imperfection amplitude. When $a = 2\sqrt{2}$, the buckling load reaches its maximum; that is, twice the buckling load of the straight beam. Hence, by increasing the imperfection amplitude from 0 to $2\sqrt{2}$, the beam experiences an overall stiffening effect. By increasing a above $2\sqrt{2}$, the buckling load decreases. In contrast, in this range, the beam experiences a stiffness degrading effect. When $a_c = 8$, the buckling load is zero. This is a trademark of the onset of a peculiar system state which is known as an 'everted state' or a 'null–load equilibrium'. For this critical value of the imperfection amplitude, the beam has two possible states: the fundamental and everted states. As a is increased further, the critical load becomes negative and increases in absolute value. This result is in agreement with the results of Srubshchik (1967). He found that the lowest critical load of a shell with sufficiently large curvature is negative. Next, we investigate the case of an initial geometric imperfection of the form of the lowest eigenmode of a straight clamped–clamped beam; that is,

$$w_0(x) = a\phi(x) \tag{4.21}$$

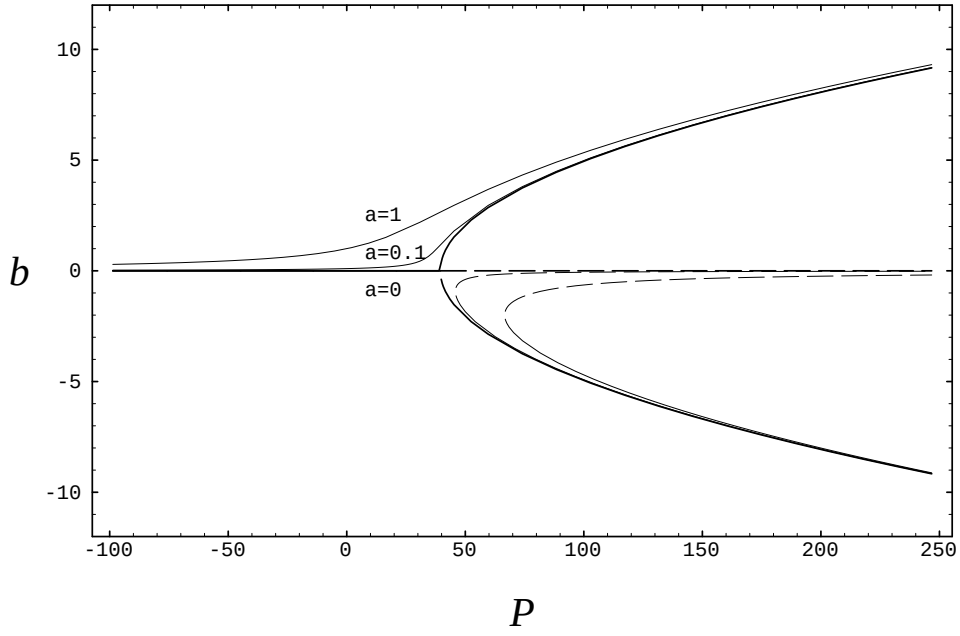

Figure 4.1: Bifurcation diagram: variation of the nonlinear static response with the nondimensional end load for $a = 0$, $a = 0.1$, $a = 1$. Solid (dashed) lines denote stable (unstable) solutions.

where a represents the initial rise parameter and

$$\phi = b_1(\cos\eta x - \cosh\eta x) + b_2(\sin\eta x - \eta\sinh\eta x) \tag{4.22}$$

where η is the lowest positive root of the characteristic equation $\cos\eta\cosh\eta = 1$. Normalizing $\phi(x)$ such that $\phi(\frac{1}{2}) = 1$ yields

$$\begin{aligned} b_1 = ku_1,\ \ b_2 = ku_2,\ \ u_1 = \sin\eta - \sinh\eta,\ \ u_2 = -(\cos\eta - \cosh\eta) \\ k = \left\{u_1\left(\cos\frac{\eta}{2} - \cosh\frac{\eta}{2}\right) + u_2\left(\sin\frac{\eta}{2} - \eta\sinh\frac{\eta}{2}\right)\right\}^{-1} \end{aligned} \tag{4.23}$$

Substituting Eqs. (4.21) and (4.22) into Eq. (4.4) and letting $F_0 = 0$, we can express a particular solution of the resulting equation as

$$\psi_p = a_5(\cos\eta x + k_1\cosh\eta x + k_2\sin\eta x + k_3\sinh\eta x) \tag{4.24}$$

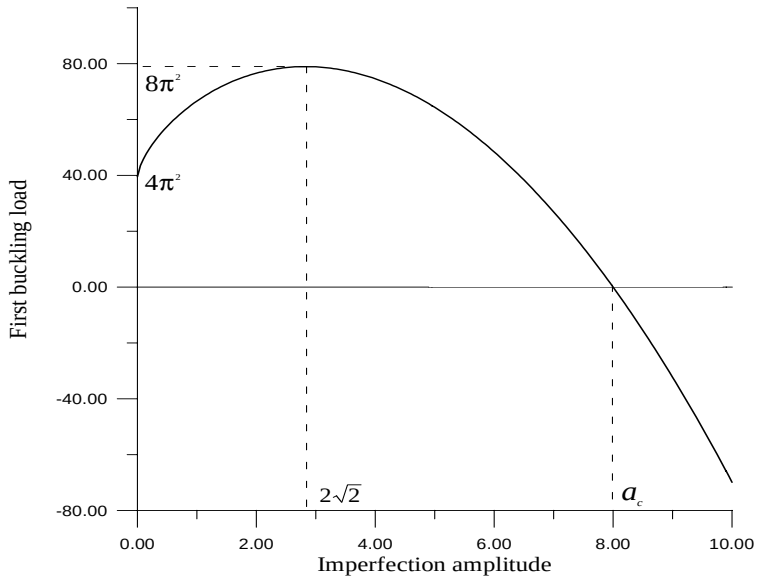

Figure 4.2: Variation of the first nondimensional buckling load with the nondimensional imperfection amplitude.

where

$$a_5 = b\frac{\eta^2 b_1}{\eta^2 - \lambda^2}, \quad k_1 = -\frac{\eta^2 - \lambda^2}{\eta^2 + \lambda^2}, \quad k_2 = \frac{b_2}{b_1}, \quad k_3 = \eta k_2 \tag{4.25}$$

Next, substituting Eq. (4.24) into Eq. (4.11), solving for the a_i, and then substituting the result into Eq. (4.9) yields the eigenvalues. The nonlinear equilibrium can be expressed as

$$\begin{aligned}\psi = {} & a_1 + a_2 x + a_3 \cos\lambda x + a_4 \sin\lambda x \\ & + a_5(\cos\eta x + k_1 \cosh\eta x + k_2 \sin\eta x + k_3 \sinh\eta x)\end{aligned} \tag{4.26}$$

In Fig. 4.3, we show the characteristic equation for the eigenvalue λ, Eq. (4.9), when $a = 5$ and $P_0 = 70$. There are three solutions for $\lambda : \lambda_1 = 3.368$, $\lambda_2 = 9.334$, $\lambda_3 = 10.236$. These eigenvalues correspond to three post–buckling equilibria, as shown in Fig. 4.4.

In Figs. 4.5 and 4.6, we show the characteristic equation and the post–buckling equilibria, respectively, when $a = 10$ and $P_0 = 70$. In this case, there are five solutions: $\lambda_1 = 2.110$,

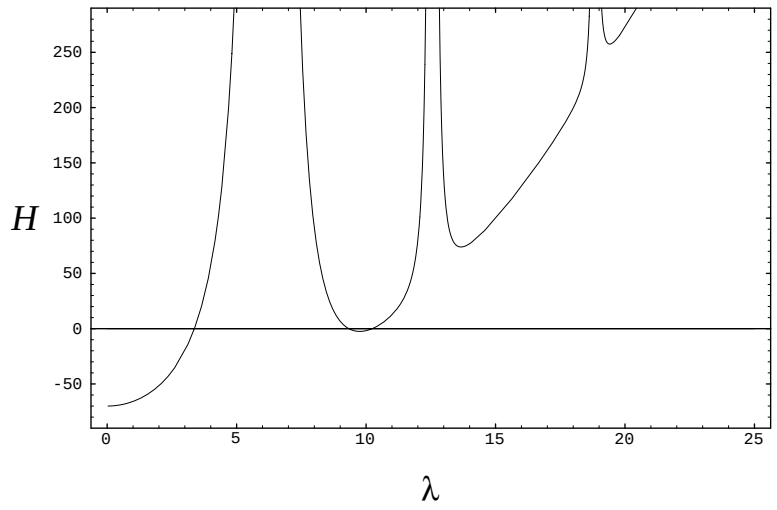

Figure 4.3: Characteristic equation for $a = 5$ and $P_0 = 70$.

$\lambda_2 = 8.964$, $\lambda_3 = 11.819$, $\lambda_4 = 13.329$, $\lambda_5 = 17.311$. Three of these solutions are stable and two are unstable. Therefore, the system possesses an additional stable equilibrium state in contrast with the case of the initial imperfection given by Eq. (4.12). Clearly, the shape of the initial imperfection plays a key role.

4.3 Straight Beams

The equilibria of an initially straight beam subject to an end load and distributed change in temperature are governed by Eqs. (4.4) and (4.3) with $w_0 \equiv 0$ and $F_0 \equiv 0$; that is,

$$\psi^{iv} + \lambda^2 \psi'' = 0 \tag{4.27}$$

$$\lambda^2 = P_0 - \frac{1}{2}\int_0^1 \psi'^2 dx \tag{4.28}$$

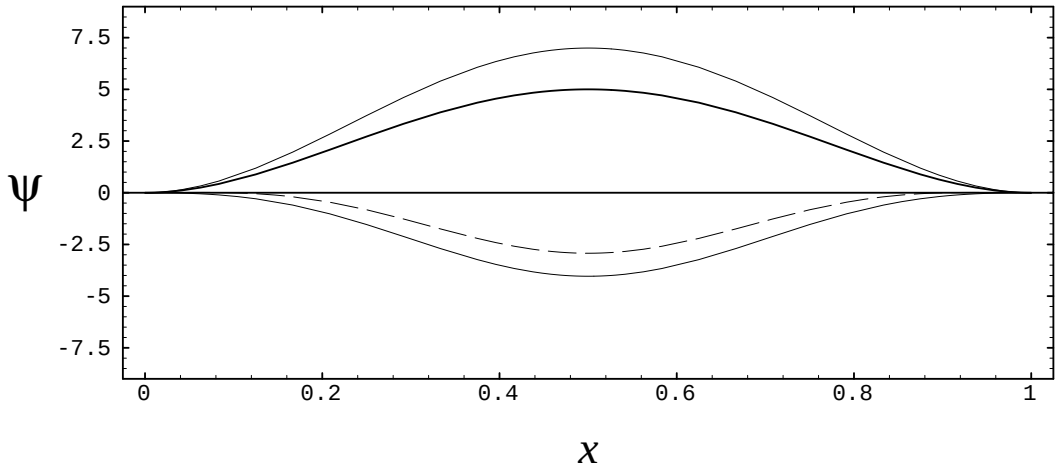

Figure 4.4: Post–buckling solutions for $a = 5$ and $P_0 = 70$. The solid (dashed) lines denote the stable (unstable) solutions. The thick solid line indicates the initial configuration.

It follows from Eq. (4.27) that the particular solution is identically zero and Eq. (4.8) becomes

$$\begin{aligned} B_{11}[\psi_h]|_{x=0} &= 0 \\ B_{12}[\psi_h]|_{x=0} &= 0 \\ B_{21}[\psi_h]|_{x=1} &= 0 \\ B_{22}[\psi_h]|_{x=1} &= 0 \end{aligned} \tag{4.29}$$

For nontrivial solutions for ψ, the determinant of Eq. (4.29) must be equal to zero. This condition yields the characteristic equation for the eigenvalue λ. Once we obtain λ, we can determine the a_i within an arbitrary constant. Hence, the post–buckling deflection can be expressed as

$$\psi = b\varphi(x;\lambda) \tag{4.30}$$

where

$$\varphi(x;\lambda) = a_1 + a_2 x + a_3 \cos\lambda x + a_4 \sin\lambda x \tag{4.31}$$

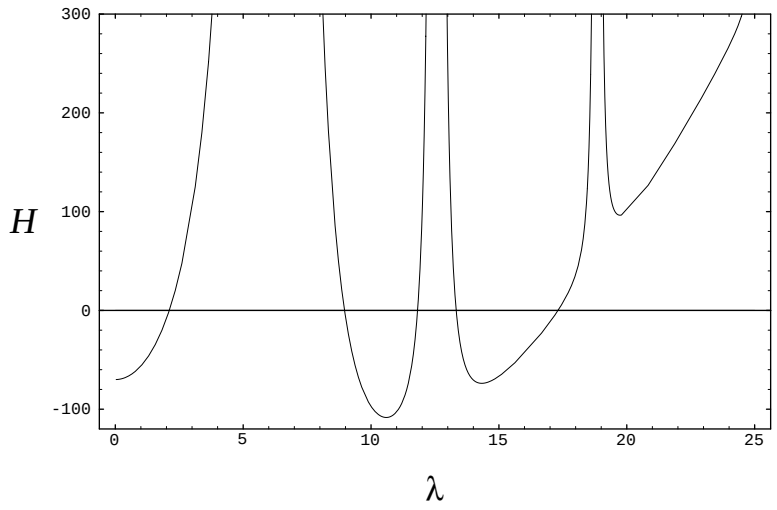

Figure 4.5: Characteristic equation for $a = 10$ and $P_0 = 70$.

is the buckling mode corresponding to the eigenvalue λ. The buckling mode shape is normalized such that $\varphi(\frac{1}{2}) = 1$.

At the onset of buckling, $b = 0$. Consequently, it follows from Eq. (4.28), that

$$P_c = \lambda^2 \tag{4.32}$$

where P_c denotes the first nondimensional buckling load. In the post–buckling range, $P_0 > P_c$ and $b \neq 0$. Then, it follows from Eqs. (4.28) and (4.32) that

$$P_0 = P_c + \frac{1}{2} b^2 \int_0^1 \varphi'^2 dx \tag{4.33}$$

Hence,

$$b^2 = \frac{2(P_0 - P_c)}{\int_0^1 \varphi'^2 dx} \tag{4.34}$$

For a clamped–clamped straight beam, the lowest eigenvalue and corresponding buckling mode are

$$\lambda = 2\pi \quad \text{and} \quad \varphi(x) = \frac{1}{2}(1 - \cos 2\pi x) \tag{4.35}$$

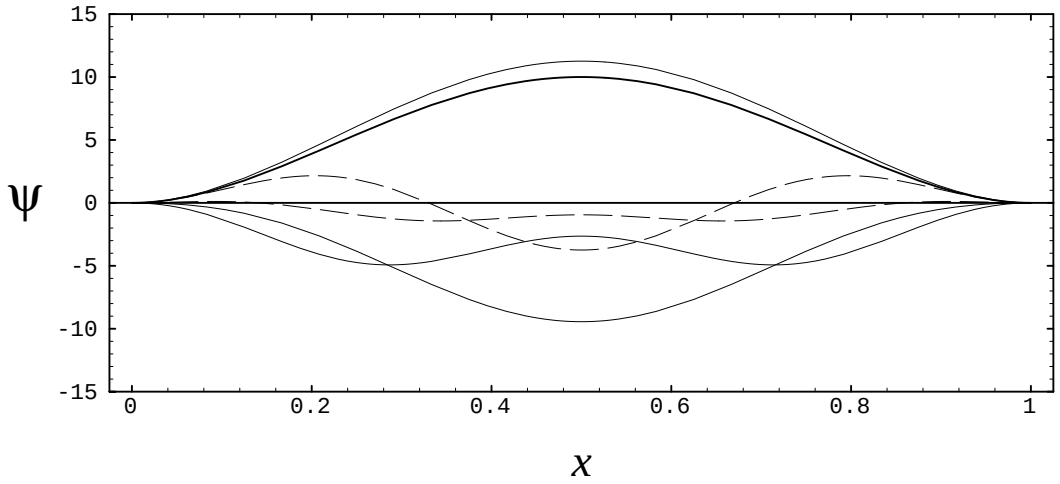

Figure 4.6: Post–buckling equilibria for $a = 10$ and $P_0 = 70$. The solid (dashed) lines denote the stable (unstable) solutions. The thick solid line indicates the initial configuration.

Substituting Eq. (4.35) into Eq. (4.34) yields

$$b^2 = 4(P_0 - P_c)/\pi^2 \tag{4.36}$$

This post–buckling solution is in agreement with that obtained by Nayfeh, Kreider, and Anderson (1995).

4.4 Null–Load Solutions

Structures that have equilibrium configurations other than the trivial one in absence of external loads are called *non–stiff structures* and the nontrivial equilibria are known as *everted states* (Antman and Srubshchik, 1996). The solutions corresponding to nontrivial equilibria are called *null–load solutions*. The problem of eversion is one of the central problems in nonlinear solid mechanics. In fact, an eversion represents the antithesis of infinitesimal deformations that typify not only linear elasticity, but also the many pertur-

bation solutions of the full nonlinear theory. Everted states are important because their existence means that snap–buckling can occur under some external perturbations.

The existence of null–load solutions was shown first by Biezeno (1935) in his investigation of the snap–through instability of a freely supported shallow spherical cap subject to a central concentrated load. Later, Vorovich (1957) put forward the possibility of the existence of nontrivial equilibria for shallow shells with sufficiently large curvatures in the absence of loads. Srubshchik (1967) pointed out that a characteristic property of a non–stiff shell is that its lowest critical load is negative. By using a two–phase asymptotic approach, he showed that a thin shallow spherical cap with hinged edge has another equilibrium configuration close to the mirror image. Later, Srubshchik(1972) treated the problem of non–stiff freely supported shallow shells. More recently, Antman and Srubshchik (1996) thoroughly treated the existence of eversion in axisymmetric elastic shells by using a general, geometrically exact nonlinear theory that accounts for extensional, flexural, and shear deformations. They found conditions for the existence of an everted state and expressed it in a matched asymptotic expansion, taking into account the boundary–layer effects. They considered free and hinged boundary conditions.

4.4.1 Non–Stiff Imperfect Beams

Everted states for imperfect beams are, by definition, nontrivial equilibrium configurations that exist in the absence of external applied loads. Therefore, these states are solutions of Eq. (4.1) with $F_0 = 0$ and $P_0 = 0$. That is, they are solutions of

$$\psi^{iv} + \frac{1}{2}\psi'' \int_0^1 (w_0'^2 - \psi'^2)dx = w_0^{iv} \tag{4.37}$$

subject to appropriate boundary conditions. Following a procedure similar to that in Section 4.1, we obtain the following nonlinear equation for the eigenvalues λ:

$$H(\lambda, w_0) = \lambda^2 + \frac{1}{2}\int_0^1 \left(\frac{d\psi(x;\lambda,w_0)}{dx}\right)^2 dx - \frac{1}{2}\int_0^1 \left(\frac{dw_0}{dx}\right)^2 dx = 0 \tag{4.38}$$

which can be obtained from Eq. (4.9) by setting $P_0 = 0$. If we assume an initial imperfection of the form in Eq. (4.12), then the null–load solution can be expressed by Eq. (4.15) with λ being given by Eq. (4.16) with $P_0 = 0$; that is,

$$H(\lambda, a) = \lambda^2 - \frac{\pi^2 a^2 \lambda^2 (\lambda^2 - 8\pi^2)}{4(\lambda^2 - 4\pi^2)^2} = 0 \tag{4.39}$$

Alternatively, we can express the null–load solution by Eq. (4.17), with b being given by Eq. (4.18) with $P_0 = 0$; that is,

$$b^3 - \Big(a^2 - 16\Big)b - 16a = 0 \tag{4.40}$$

Equation (4.40) admits the following closed–form solutions:

$$b = a \quad \text{and} \quad b = -\frac{1}{2}a \pm \sqrt{\frac{1}{4}a^2 - 16} \tag{4.41}$$

The first solution corresponds to a configuration that coincides with the imperfection. The latter two solutions exist only when $|a| \geq 8$.

To investigate in more details the null–load solutions for general imperfections and boundary conditions, we construct a pedestrian expansion of these solutions. To this end, we find it more convenient to introduce the nondimensionalization

$$w_0 = \frac{\hat{w}_0}{l}, \quad \psi = \frac{\hat{\psi}}{l} \tag{4.42}$$

Then, setting $F_0 = 0$ and $P_0 = 0$, we rewrite Eq. (4.1) as

$$\psi^{iv} + \frac{1}{2}\varrho^2 \psi'' \int_0^1 (w_0'^2 - \psi'^2) dx = w_0^{iv} \tag{4.43}$$

We consider a geometric imperfection of the form

$$w_0 = \frac{1}{2}a^*(1 - \cos 2\pi x) \tag{4.44}$$

We seek solutions of Eq. (4.43) other than the trivial solution w_0. To this end, we note that $\varrho^2 = (\ell/r)^2$ is large for very slender beams. Hence, we set

$$\epsilon = 1/\varrho^2 \tag{4.45}$$

and rewrite Eq. (4.43) as

$$\epsilon\psi^{iv} + \frac{1}{2}\psi'' \int_0^1 (w_0'^2 - \psi'^2)dx = \epsilon w_0^{iv} \tag{4.46}$$

We note that $\epsilon = 0$ (i.e., $\varrho^2 = \infty$) corresponds to an infinitely slender imperfect beam or a suspended cable. In this case, Eq. (4.46) reduces to

$$\frac{1}{2}\psi'' \int_0^1 (w_0'^2 - \psi'^2)dx = 0 \tag{4.47}$$

whose solutions, which satisfy the boundary conditions (4.10), are

$$\psi = 0 \quad \text{and} \quad \psi = \pm w_0 \tag{4.48}$$

where $\psi = 0$ is an unstable solution, $\psi = w_0$ corresponds to the trivial solution, whereas $\psi = -w_0$ represents an everted state of the system which is the mirror image of the trivial equilibrium. We note that the trivial solution $\psi = w_0$ is an exact solution of Eqs. (4.43) and (4.10) for all values of ϵ.

When $\epsilon \neq 0$, the null–load solution is a perturbation of the nontrivial solution $\psi = -w_0$. Because ϵ is multiplying the highest derivative, namely the fourth derivative, the problem is a singular–perturbation one. Hence, in general, *edge layers* are expected near the boundaries. The method of matched asymptotic expansions is one of the available methods

for treating such a problem. However, for the present form of the initial imperfection, a pedestrian expansion turns out to be uniformly valid over the whole domain. Therefore, there is no need for the method of matched asymptotic expansions.

We seek a pedestrian expansion of the solutions of Eqs. (4.43) and (4.10) in the form

$$\psi(x;\epsilon) = \psi_0(x) + \epsilon\psi_1(x) + ... \tag{4.49}$$

Substituting Eq. (4.49) into Eq. (4.43) and (4.10) and equating coefficients of like powers of ϵ yields

Order ϵ^0:

$$\frac{1}{2}\psi_0'' \int_0^1 (w_0'^2 - \psi_0'^2)dx = 0 \tag{4.50}$$

Order ϵ:

$$\frac{1}{2}\psi_1'' \int_0^1 (w_0'^2 - \psi_0'^2)dx - \psi_0'' \int_0^1 w_0'\psi_1' dx = w_0^{iv} - \psi_0^{iv} \tag{4.51}$$

$$\psi_i = 0 \ \text{ and } \ \psi_i' = 0 \ \text{ at } \ x = 0 \ \text{ and } \ 1 \tag{4.52}$$

for all i.

The solutions of Eqs. (4.50) and (4.52) are

$$\psi_0 \equiv 0 \ \text{ or } \ \psi_0 = \pm w_0 \tag{4.53}$$

When $\psi_0 = 0$, the solution of Eqs. (4.51) and (4.52) is

$$\psi_1 = -\frac{8}{a^*}(1 - \cos 2\pi x) \tag{4.54}$$

Hence,

$$\psi = -\frac{8}{a^*}\epsilon(1 - \cos 2\pi x) + \cdots \tag{4.55}$$

which is the unstable solution.

When $\psi_0 = -w_0$, Eq. (4.51) becomes

$$\int_0^1 \psi_1' \sin 2\pi x dx = \frac{8\pi}{a^*} \tag{4.56}$$

The solution of Eqs. (4.56) and (4.52) is

$$\psi_1 = \frac{8}{a^*}(1 - \cos 2\pi x) \tag{4.57}$$

Substituting for ψ_0 and ψ_1 in Eq. (4.49) yields an approximate expression for the null–load solution

$$\psi(x;\epsilon) = -\frac{1}{2}a^* \left(1 - \frac{16\epsilon}{a^{*2}}\right)(1 - \cos 2\pi x) + ... \tag{4.58}$$

Alternatively, we assume that the null–load solution can be represented in the form

$$\psi(x;\epsilon) = \frac{1}{2}b^*(\epsilon)(1 - \cos 2\pi x) \tag{4.59}$$

Substituting Eqs. (4.44) and (4.59) into Eq. (4.46) yields

$$b^{*3} - b^* a^{*2} = 16\epsilon(a^* - b^*) \tag{4.60}$$

whose solutions can be expressed as $b^* = a^*$ and $b^* = -\frac{1}{2}a^* \left[1 \pm \sqrt{1 - \frac{64\epsilon}{a^{*2}}}\right]$. The first solution corresponds to the trivial solution $\psi = w_0$, whereas the other two solutions correspond to null–load solutions. Null–load solutions exist when the discriminant of Eq. (4.60) is greater or equal to zero. That is,

$$\left(\frac{16\epsilon^2 - a^{*2}}{3}\right)^3 + 64\epsilon^4 a^{*2} \leq 0 \quad \text{or} \quad |a^*| \geq 8\epsilon$$

In terms of the original nondimensional imperfection amplitude, this inequality is expressed as $|a| \geq 8$. We note that the condition for everted states can be obtained alternatively by requiring that the lowest buckling load be less than or equal to zero. In Fig. 4.7, we show

the region of existence of null–load solutions in the $a^* - \varrho$ plane. Here, we considered a logarithmic scale for the ϱ–axis.

We note that, for very small slenderness, which is a common case for structural curved beams ($\varrho \approx 10^{-1} \div 10^{-2}$), the required imperfection amplitude for null–load solutions is considerably high. Null–load solutions do not exist for ordinary structural members because the required rise–to–span ratios are unrealistic. However, in the micro–electro–mechanical technology (MEMS), some micro curved beams are used as specific devices (switches, micro–bridges, etc.). Because these elements are designed to be very flexible, such everted states may be possible and the designers should be aware of them. Micro elements made of hyperelastic composite materials are being designed for endodontic applications. Everted states may exist for these elements.

In Fig. 4.8, we show variation of the nonlinear static response with the nondimensional load for $a = 0$, $a = 1$, and $a = 12$. When the load is zero, we observe that, for $a = 12$ ($a > 8$), there are three solutions: the trivial, unstable, and null–load solutions. Moreover, the buckling load is negative, in agreement with the results of Shrubshick (1967). In Fig. 4.9, we show these states of the beam and compare the exact null–load solution, Eqs. (4.59) and (4.60), with the approximate solution, Eq. (4.58). In this figure, the original nondimensional variables are used, as in Eq. (3.24).

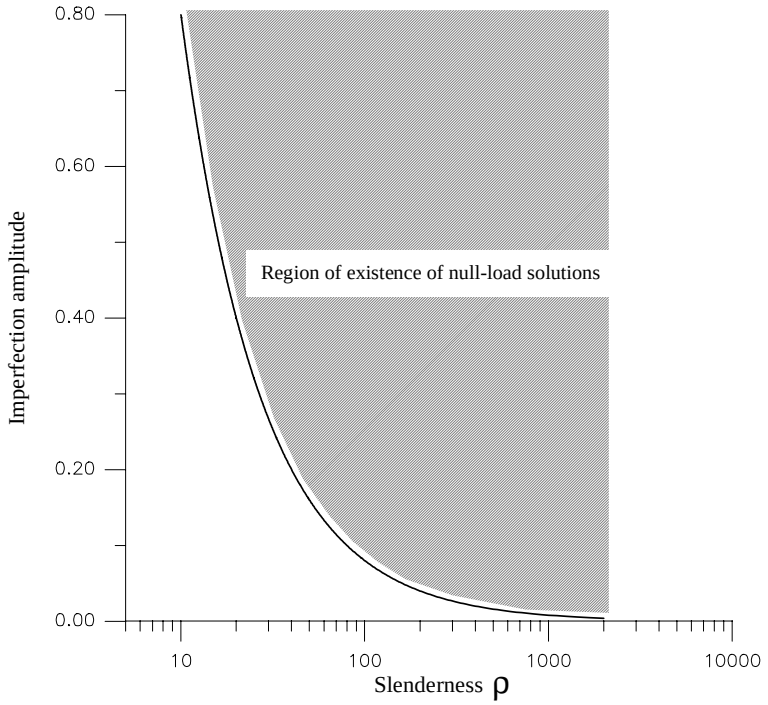

Figure 4.7: Region of existence of null–load solutions in the $a^* - \varrho$ plane.

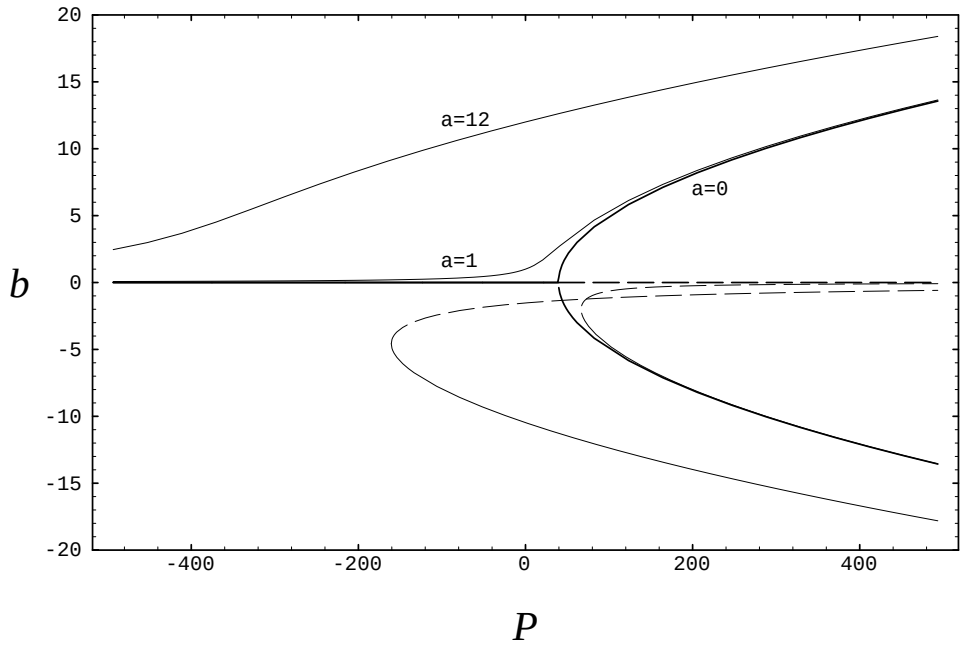

Figure 4.8: Bifurcation diagram: variation of the nonlinear static equilibrium with the nondimensional load for $a = 0$, $a = 1$, and $a = 12$.

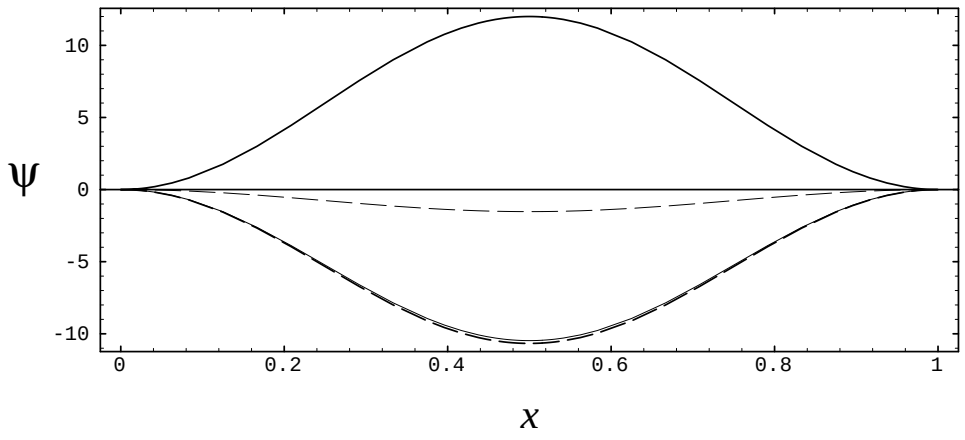

Figure 4.9: Null–load solution when $a = 12$. Solid (dashed) lines denote stable (unstable) solutions. The thick dashed line denotes the approximate null–load solution.

Chapter 5

Linear Vibrations

In this chapter, we study free oscillations of an initially imperfect beam around one of its nonlinear equilibria in either the pre–buckling or the post–buckling ranges. Nayfeh, Kreider, and Anderson (1995) studied linear vibrations of a straight beam around the symmetric post–buckling configurations and obtained an exact solution for the natural frequencies and mode shapes. Our analysis proceeds along the same lines. Here, we extend the work of Nayfeh, Kreider, and Anderson (1995) by including the effect of geometric imperfections and temperature changes. We obtain an exact solution with no a priori assumption on the pre– or post–buckling solutions. We show that accounting for initial geometric imperfections yields natural frequencies and mode shapes that agree with remarkable accuracy with the experimental results of Kreider (1995).

5.1 Analysis

By dropping the nonlinear, nonhomogeneous, and damping terms and putting $P(t) \equiv 0$ in Eq. (3.26), we obtain the following homogeneous differential equation governing linear vibrations around the nonlinear equilibrium configuration $\psi(x)$:

$$\ddot{v} + v^{iv} + v''\left[P_0 + \frac{1}{2}\int_0^1 (w_0'^2 - \psi'^2)dx\right] - \psi''\int_0^1 v'\psi' dx = 0 \tag{5.1}$$

To determine the natural frequencies and associated mode shapes, we seek solutions of Eq. (5.1) in the form $v(x,t) \propto e^{i\omega t}\phi(x)$. Hence, Eq. (5.1) becomes

$$\phi^{iv} + \zeta\phi'' - \psi''\int_0^1 \phi'\psi' dx = \omega^2\phi \tag{5.2}$$

where

$$\zeta = \left[P_0 + \frac{1}{2}\int_0^1 (w_0'^2 - \psi'^2)dx\right] \tag{5.3}$$

Equation (5.2) and the pertinent boundary conditions constitute an eigenvalue problem for the natural circular frequencies ω and eigenmodes ϕ. In the following, we present a general procedure to solve exactly the eigenvalue problem for arbitrary geometric imperfections and boundary conditions.

We note that the integral term $\int_0^1 \phi'\psi' dx$ in Eq. (5.2) is constant for any given solution of the eigenvalue problem. Hence $\psi''\int_0^1 \phi'\psi' dx$ can be treated as an inhomogeneous term. Accordingly, we let

$$c = \int_0^1 \phi'\psi' dx \tag{5.4}$$

Then, the general solution of Eq. (5.2) can be expressed as the superposition of the homogeneous solution ϕ_h and a particular solution ϕ_p; that is,

$$\phi = \phi_h + \phi_p[\psi''] \tag{5.5}$$

where

$$\phi_h = c_1 \sin \lambda_1 x + c_2 \cos \lambda_1 x + c_3 \sinh \lambda_2 x + c_4 \cosh \lambda_2 x \tag{5.6}$$

and the λ_i are related to the frequency ω by

$$\lambda_{1,2} = \left\{ \pm \frac{1}{2}\zeta + \sqrt{\frac{1}{4}\zeta^2 + \omega^2} \right\}^{\frac{1}{2}} \tag{5.7}$$

Substituting Eqs. (5.5) and (5.6) into the boundary conditions, Eq. (4.2), and adding Eq. (5.4) to the resulting set of equations, we obtain an algebraic eigenvalue problem that yields ω and the c_i. The result is

$$\begin{aligned}
&B_{11}[\phi_h]|_{x=0} + B_{11}[\phi_p]|_{x=0} = 0 \\
&B_{12}[\phi_h]|_{x=0} + B_{12}[\phi_p]|_{x=0} = 0 \\
&B_{21}[\phi_h]|_{x=1} + B_{21}[\phi_p]|_{x=1} = 0 \\
&B_{22}[\phi_h]|_{x=1} + B_{22}[\phi_p]|_{x=1} = 0 \\
&\int_0^1 \left(\phi_h' + \phi_p'[\psi''] \right) \psi' dx - c = 0
\end{aligned} \tag{5.8}$$

The characteristic equation is obtained by setting the determinant of the coefficient matrix in Eq. (5.8) equal to zero. To determine uniquely the c_i, we use the normalization condition

$$\int_0^1 \phi(x)^2 dx = 1 \tag{5.9}$$

In the case of clamped–clamped beams, the boundary conditions are given by

$$\phi = 0 \ \text{ and } \ \phi' = 0 \ \text{ at } \ x = 0 \ \text{ and } \ 1 \tag{5.10}$$

Hence, Eq. (5.8) becomes

$$c_2 + c_4 + \phi_p(0) = 0$$

$$\lambda_1 c_1 + \lambda_2 c_3 + \phi_p'(0) = 0$$

$$c_1 \sin\lambda_1 + c_2 \cos\lambda_1 + c_3 \sinh\lambda_2 + c_4 \cosh\lambda_2 + \phi_p(1) = 0$$

$$c_1\lambda_1 \sin\lambda_1 - c_2\lambda_1 \cos\lambda_1 + c_3\lambda_2 \sinh\lambda_2 + \lambda_2 c_4 \cosh\lambda_2 + \phi_p'(1) = 0$$

$$c_1\lambda_1 \int_0^1 \psi' \cos\lambda_1 x dx - c_2\lambda_1 \int_0^1 \psi' \sin\lambda_1 x dx + c_3\lambda_2 \int_0^1 \psi' \sinh\lambda_2 x dx + c_4\lambda_2 \int_0^1 \psi' \cosh\lambda_2 x dx + \int_0^1 \phi_p'\psi' dx - c = 0 \tag{5.11}$$

5.2 Clamped–Clamped Straight Beams

In this section, we determine the natural frequencies and mode shapes of a clamped–clamped initially straight beam around its first buckling mode shape. In this case,

$$\zeta = P_c = 4\pi^2 \ \text{ and } \ \psi(x) = \frac{1}{2} b(1 - \cos 2\pi x) \tag{5.12}$$

Hence, Eq. (5.2) becomes

$$\phi^{iv} + 4\pi^2\phi'' - \omega^2\phi - 2b^2\pi^3 \cos 2\pi x \int_0^1 \phi' \sin 2\pi x dx = 0 \tag{5.13}$$

In this case, the solution of Eqs. (5.13) and (5.10) can be expressed as

$$\phi = c_1 \sin\lambda_1 x + c_2 \cos\lambda_1 x + c_3 \sinh\lambda_2 x + c_4 \cosh\lambda_2 x + c_5 \cos 2\pi x \tag{5.14}$$

where

$$\lambda_{1,2} = \left\{ \pm 2\pi^2 + \sqrt{4\pi^4 + \omega^2} \right\}^{\frac{1}{2}} \tag{5.15}$$

and the c_i are governed by

$$c_2 + c_4 + c_5 = 0 \tag{5.16}$$

$$c_1\lambda_1 + c_3\lambda_2 = 0 \tag{5.17}$$

$$c_1 \sin\lambda_1 + c_2 \cos\lambda_1 + c_3 \sinh\lambda_2 + c_4 \cosh\lambda_2 + c_5 = 0 \tag{5.18}$$

$$c_1\lambda_1 \cos\lambda_1 - c_2\lambda_1 \sin\lambda_1 + c_3\lambda_2 \cos\lambda_2 + c_4\lambda_2 \sinh\lambda_2 = 0 \tag{5.19}$$

$$\begin{aligned}\frac{\lambda_1(\cos\lambda_1 - 1)}{\lambda_1^2 - 4\pi^2}c_1 - \frac{\lambda_1 \sin\lambda_1}{\lambda_1^2 - 4\pi^2}c_2 + \frac{\lambda_2(1 - \cosh\lambda_2)}{\lambda_2^2 + 4\pi^2}c_3 \\ - \frac{\lambda_2 \sinh\lambda_2}{\lambda_2^2 + 4\pi^2}c_4 + \frac{\omega^2 - 2b^2\pi^4}{4b^2\pi^4}c_5 = 0\end{aligned} \tag{5.20}$$

Equations (5.13)–(5.20) are in full agreement with those derived by Nayfeh, Kreider and Anderson (1995).

In Fig. 5.1, we show variation of the lowest four calculated nondimensional frequencies with the nondimensional end load for $P_0 > P_c$. Here, we made use of Eq. (4.34) to express the buckling level in terms of the nondimensional load.

5.3 Clamped–Clamped Imperfect Beams

In this section, we consider an initially curved clamped–clamped beam whose initial shape is given by Eq. (4.12). In this case, Eqs. (5.2) and (5.3) become

$$\phi^{iv} + \zeta\phi'' - \omega^2\phi - 2\pi^3 b^2 \cos 2\pi x \int_0^1 \phi' \sin 2\pi x dx = 0 \tag{5.21}$$

where

$$\zeta = 4\pi^2\left(1 - \frac{a}{b}\right) \tag{5.22}$$

and b represents the amplitude of the static nonlinear response given by Eq. (4.18). The particular solution can be expressed as

$$\phi_p = c_5 \cos 2\pi x \tag{5.23}$$

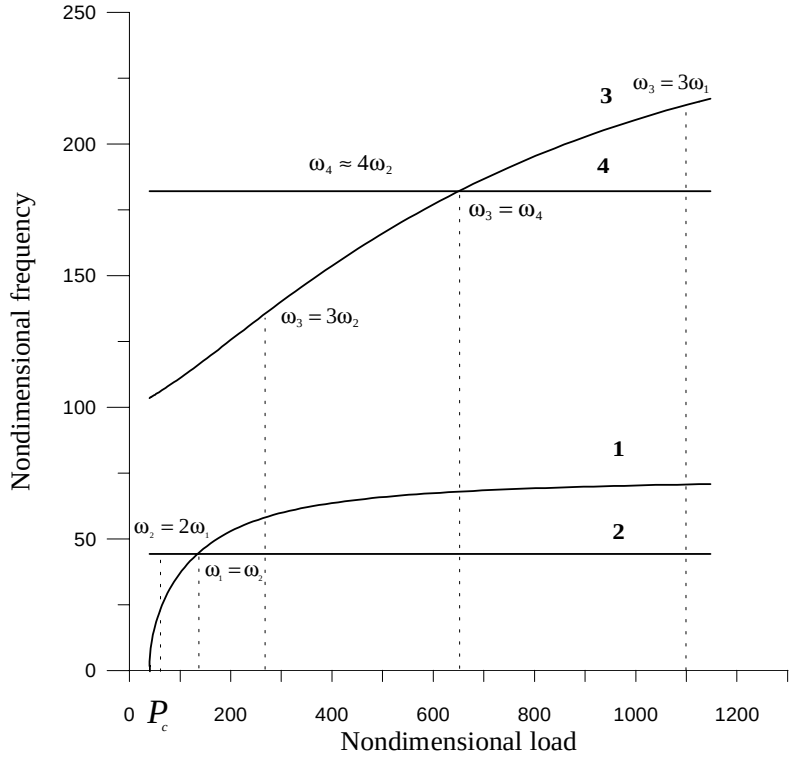

Figure 5.1: Variation of the lowest four natural frequencies of an initially straight beam with the applied end load.

Enforcing the boundary conditions, we obtain

$$c_2 + c_4 + c_5 = 0 \tag{5.24}$$

$$c_1\lambda_1 + c_3\lambda_2 = 0 \tag{5.25}$$

$$c_1 \sin\lambda_1 + c_2 \cos\lambda_1 + c_3 \sinh\lambda_2 + c_4 \cosh\lambda_2 + c_5 = 0 \tag{5.26}$$

$$c_1\lambda_1 \cos\lambda_1 - c_2\lambda_1 \sin\lambda_1 + c_3\lambda_2 \cosh\lambda_2 + c_4\lambda_2 \sinh\lambda_2 = 0 \tag{5.27}$$

$$\frac{\lambda_1(\cos\lambda_1 - 1)}{\lambda_1^2 - 4\pi^2}c_1 - \frac{\lambda_1 \sin\lambda_1}{\lambda_1^2 - 4\pi^2}c_2 + \frac{\lambda_2(1 - \cosh\lambda_2)}{\lambda_2^2 + 4\pi^2}c_3 - \frac{\lambda_2 \sinh\lambda_2}{\lambda_2^2 + 4\pi^2}c_4 + \frac{\omega^2 - 2b^2\pi^4 - 16\pi^4 a/b}{4b^2\pi^2}c_5 = 0 \tag{5.28}$$

where $\lambda_{1,2}$ is given by Eq. (5.7).

In Fig. 5.2, we show variation of the lowest three calculated nondimensional natural frequencies with the end load when $a = 1$. These frequencies are associated with linear undamped vibrations around either one of the two asymmetric stable equilibria - upper and lower equilibrium configurations. In Fig. 4.1, we display these nonlinear static responses for the considered level of imperfection. The associated buckling load given by Eq. (4.20) is 66.62. This value is higher than the buckling load $P_c = 4\pi^2$ for a straight beam. The frequency spectra in Fig. 5.2 exhibit interesting features. Comparing Figs. 5.1 and 5.2, we recognize how variations of the bifurcation patterns of the nonlinear static response with initial imperfection resulted in quantitatively as well as qualitatively different behaviors of the natural frequencies. First, the even modes are no longer independent of the applied load or buckling level. In fact, the eigenvalues, Eqs. (5.7) and (5.3), depend on the applied load for all modes. As P_0 decreases below P_c, the first natural frequency of vibration around the upper equilibrium decreases and then increases monotonically. In contrast, the first natural frequency of vibration around the lower equilibrium is zero at $P_0 = P_c$; it increases monotonically with increasing P_0, as in the case of an initially straight beam. For the other modes, there are significant quantitative as well as qualitative differences for low load levels. The frequencies of vibration around the upper and lower equilibria tend to the frequencies of the straight beam as the load increases. However, for high load levels, the present approximate theory of imperfect beams does not hold and the full nonlinear behavior of the beam must be taken into account, including large strains and displacements.

In Fig. 5.3, we contrast the lowest three natural frequencies of a straight with those of an imperfect beam when $a = 1$. Here, we consider the frequencies associated with the upper equilibrium. We note that the first crossover, $\omega_2 = \omega_1$, occurs for the initially straight beam at a lower load or buckling level.

On the other hand, the two–to–one internal resonance, $\omega_2 = 2\omega_1$, occurs for the imperfect beam at a load level that is lower than that required for the straight beam. Furthermore, the three–to–one internal resonance, $\omega_3 = 3\omega_1$, occurs for the straight beam only for high load levels, whereas for the imperfect beam it occurs for high as well as low load levels. We emphasize the fact that the initial imperfection considered is small; it is equal to the radius of gyration of the cross–section of the beam. For higher levels of imperfection and different geometric shapes, larger differences can be expected. In Fig. 5.4, we show comparison of the lowest six natural analytically obtained frequencies of a straight beam with those experimentally obtained (from Kreider, 1995). Comparing Figs. 5.3 and 5.4, we note that the presence of initial imperfection improves the agreement between analytically and experimentally obtained results for low buckling levels.

Next, we investigate the influence of distributed changes in temperature on the natural frequencies of the beam. To this end, we note from Eq. (3.27) that a change in temperature is equivalent to a nondimensional load according to

$$\Delta T = \frac{P_0}{\alpha \varrho^2} \tag{5.29}$$

Hence, the critical uniform change in temperature for buckling is

$$\Delta T_c = \frac{P_c}{\alpha \varrho^2} \tag{5.30}$$

In Fig. 5.5, we show variation of the lowest three nondimensional frequencies with uniform change in temperature when $a = 1$, $\varrho = 1197.29$, and the coefficient of thermal expansion, α, is $11.7\ 10^{-6}$. The slenderness ratio corresponds to a beam with $\ell = 279.20\ mm$, $A = 15.49\ mm^2$, $I = 0.83656\ mm^4$, and $r = 0.23239\ mm$. Comparing Figs. 5.3 and 5.4, we conclude that slender beams experience significant changes in their frequencies for low buckling levels.

Last, we calculated variation of the lowest four natural frequencies of the beam with the imperfection amplitude when the load is zero. The results are shown in Fig. 5.6. A

few internal resonances, such as one–to–one, two–to–one, and three–to–one resonance, are possible. We observe that at $a = a_c = 8$, null–load solutions are possible in the imperfect beam. Hence, we calculated the natural frequency of the first mode of vibration around the everted state. The result of this computation is shown in Fig. 5.6.

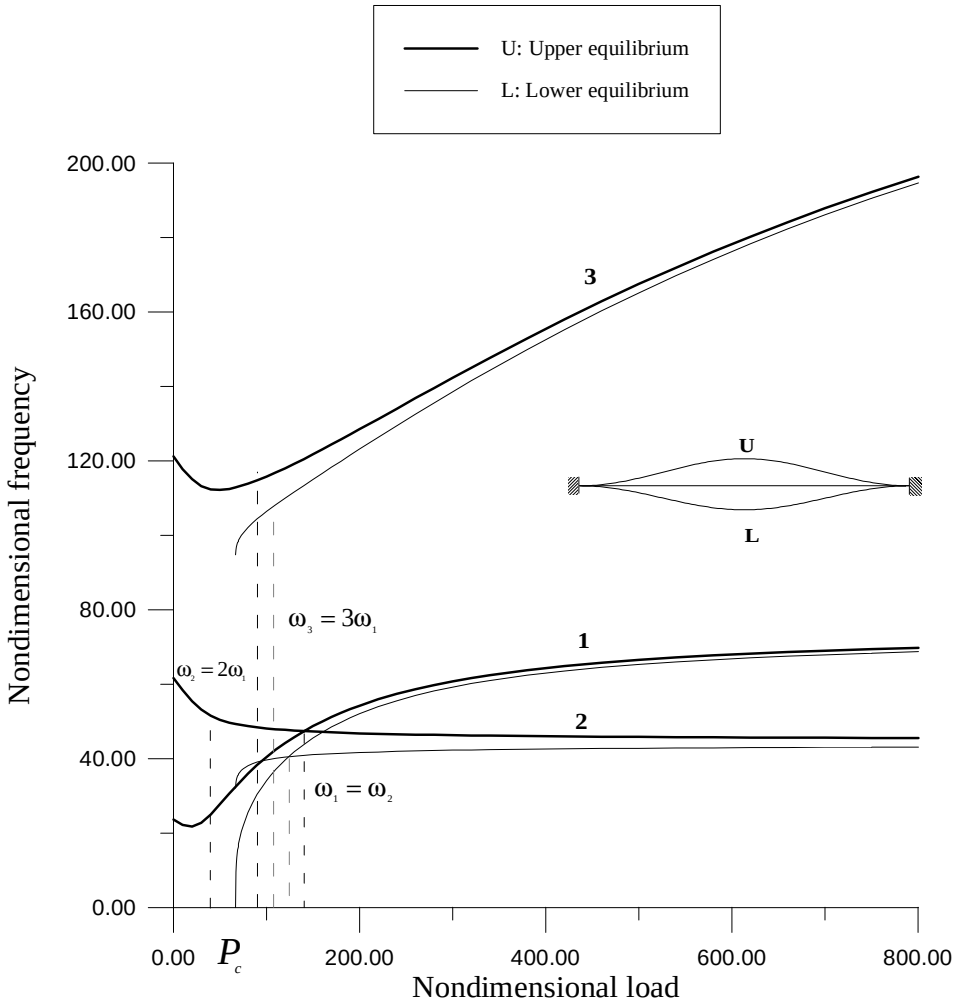

Figure 5.2: Variation of the lowest three natural frequencies of an imperfect beam with the end load when $a = 1$.

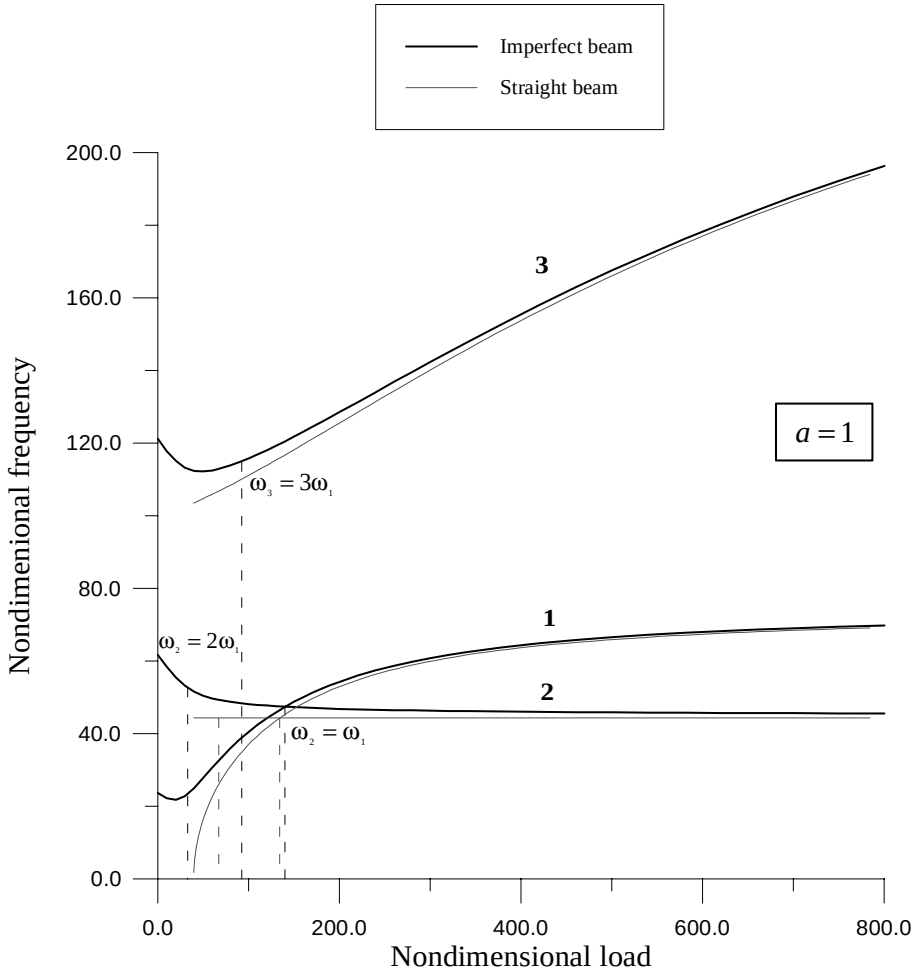

Figure 5.3: Comparison of the lowest three natural frequencies of a straight beam with those of an imperfect beam when $a = 1$.

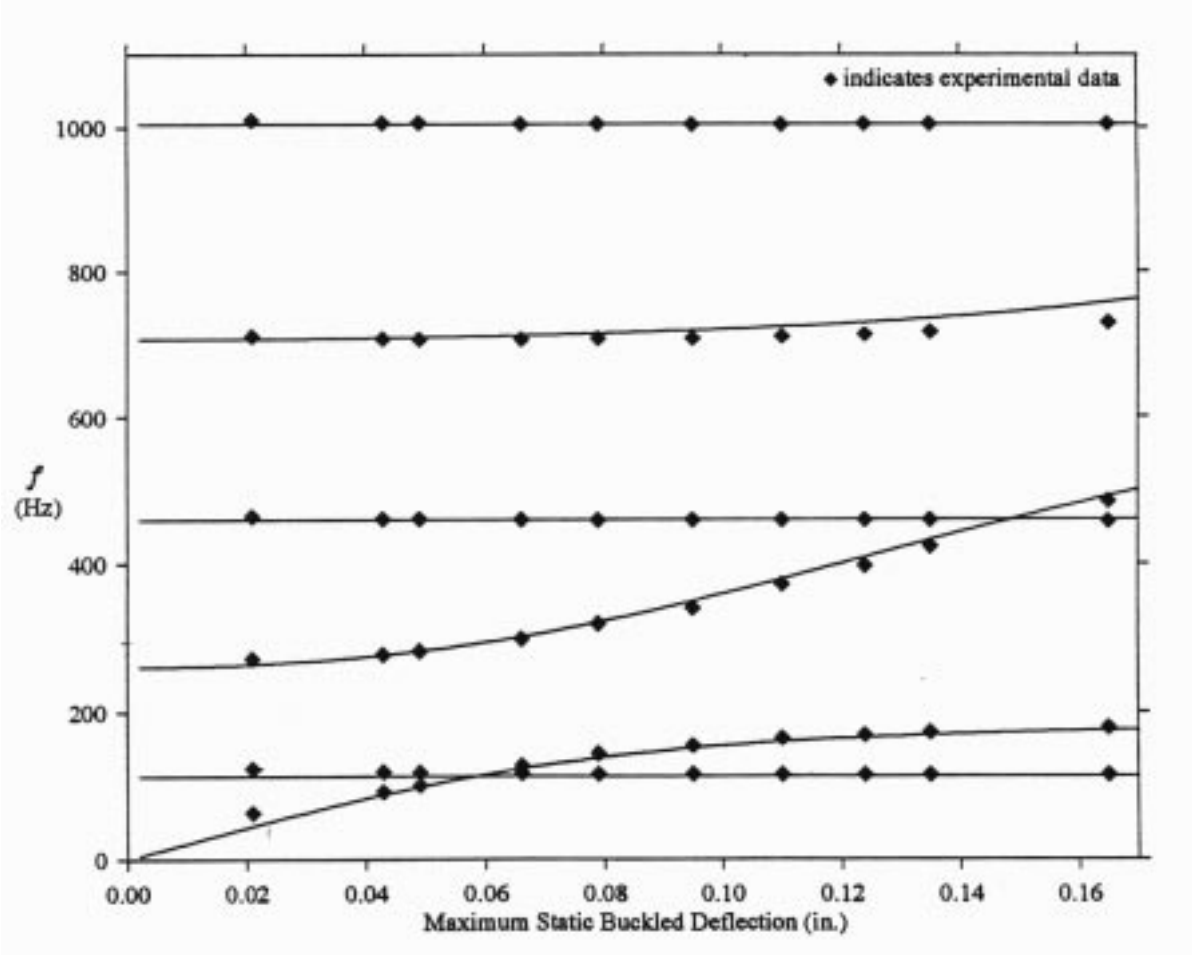

Figure 5.4: Comparison of the lowest six natural analytically obtained frequencies of a straight beam with those experimentally obtained (from Kreider, 1995)

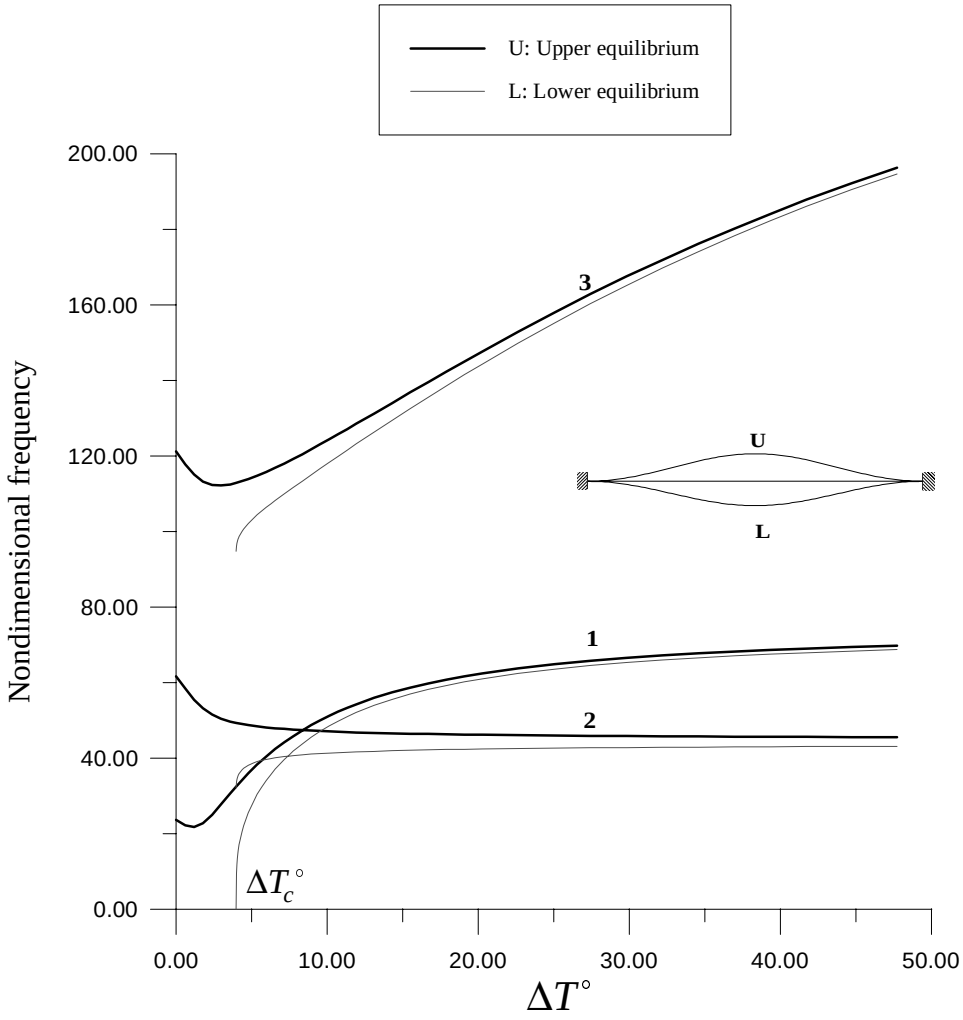

Figure 5.5: Variation of the lowest three natural frequencies of an imperfect beam with ΔT when $a = 1$, $\ell = 279.20\ mm$, $A = 15.49\ mm^2$, $I = 0.83656\ mm^4$, and $r = 0.23239\ mm$.

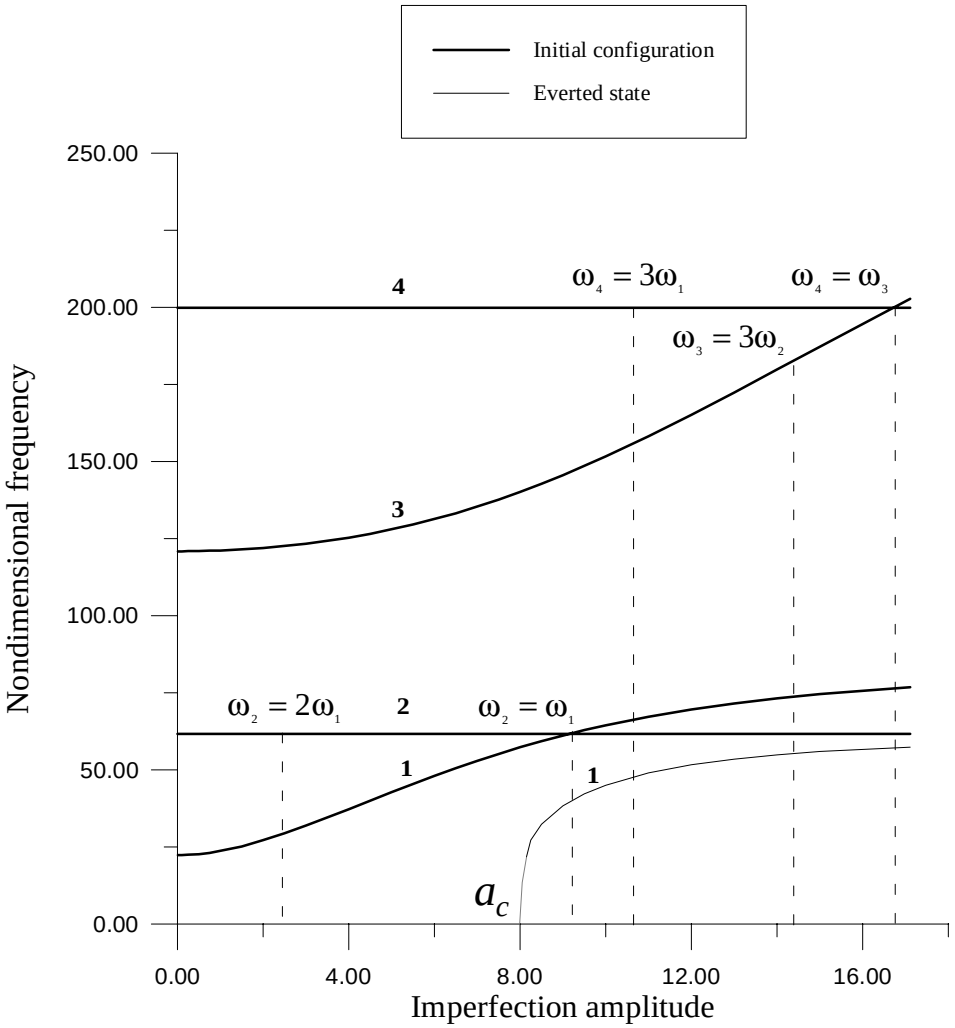

Figure 5.6: Variation of the lowest four natural frequencies of an imperfect beam with the imperfection amplitude when $P_0 = 0$.

Chapter 6

Single–Mode Responses: Theory

In this chapter, we analyze nonlinear vibrations of an initially straight, first–mode buckled beam about its first buckling mode shape. The boundary conditions are clamped–clamped. We investigate the case of primary resonance of the nth mode of the beam; that is, $\Omega \approx \omega_n$. We contrast approximate solutions obtained by using a single–mode discretization via the Galerkin method with those obtained by directly applying the method of multiple scales to the governing integro–partial–differential equation and boundary conditions. We compute the *effective nonlinearity* coefficient by using both approaches over a broad range of the buckling level (control parameter). For the second mode, both methods yield qualitatively similar but quantitatively different results in the whole range of the buckling level. On the other hand, for the first mode, there are ranges of the buckling level where the two approaches yield qualitatively as well as quantitatively different results.

6.1 Problem Formulation

To obtain the equation governing the nonlinear vibrations of an initially straight nth–mode buckled beam under a harmonic excitation, we put $w_0(x) \equiv 0$ and $P(t) \equiv 0$ in Eq. (3.26), use Eqs. (4.30) and (4.33), and obtain

$$\begin{aligned}\frac{\partial^2 v}{\partial t^2} + c\frac{\partial v}{\partial t} + \frac{\partial^4 v}{\partial x^4} + P_c\frac{\partial^2 v}{\partial x^2} - b^2\frac{\partial^2 \varphi}{\partial x^2}\int_0^1 \frac{\partial \varphi}{\partial x}\frac{\partial v}{\partial x}dx = \\ + \frac{1}{2}b\frac{\partial^2 \varphi}{\partial x^2}\int_0^1 \left(\frac{\partial v}{\partial x}\right)^2 dx + b\frac{\partial^2 v}{\partial x^2}\int_0^1 \frac{\partial \varphi}{\partial x}\frac{\partial v}{\partial x}dx \\ + \frac{1}{2}\frac{\partial^2 v}{\partial x^2}\int_0^1 \left(\frac{\partial v}{\partial x}\right)^2 dx + F(x)\cos(\Omega t) \qquad (6.1)\end{aligned}$$

where P_c and φ represent the nth Euler critical load and buckling mode shape. For a clamped–clamped beam, the first buckling load and corresponding mode shape are given by Eq. (4.35), where φ has been normalized such that $\varphi(\frac{1}{2}) = 1$. Then, in nondimensional form, nonlinear vibrations of a clamped–clamped beam about its first buckling mode are governed by

$$\begin{aligned}\ddot{v} + v^{iv} + 4\pi^2 v'' - 2b^2\pi^3 \cos 2\pi x \int_0^1 v' \sin 2\pi x dx \\ = -c\dot{v} + b\pi v''\int_0^1 v' \sin 2\pi x dx + b\pi^2 \cos 2\pi x \int_0^1 v'^2 dx \\ + \frac{1}{2}v''\int_0^1 v'^2 dx + F(x)\cos(\Omega t) \qquad (6.2)\end{aligned}$$

$$v = 0 \ \text{ and } \ v' = 0 \ \text{ at } \ x = 0 \ \text{ and } \ 1 \qquad (6.3)$$

The eigenvalue problem for the natural frequencies and mode shapes and their normalization condition are given by Eqs. (5.13)–(5.20) and Eq. (5.9), respectively. In Fig. 6.1, we show variation of the lowest four calculated nondimensional natural frequencies with the nondimensional buckling level. Inspecting Fig. 6.1, we note that the buckled beam possesses a few internal resonances, depending on the buckling level. In the following sections,

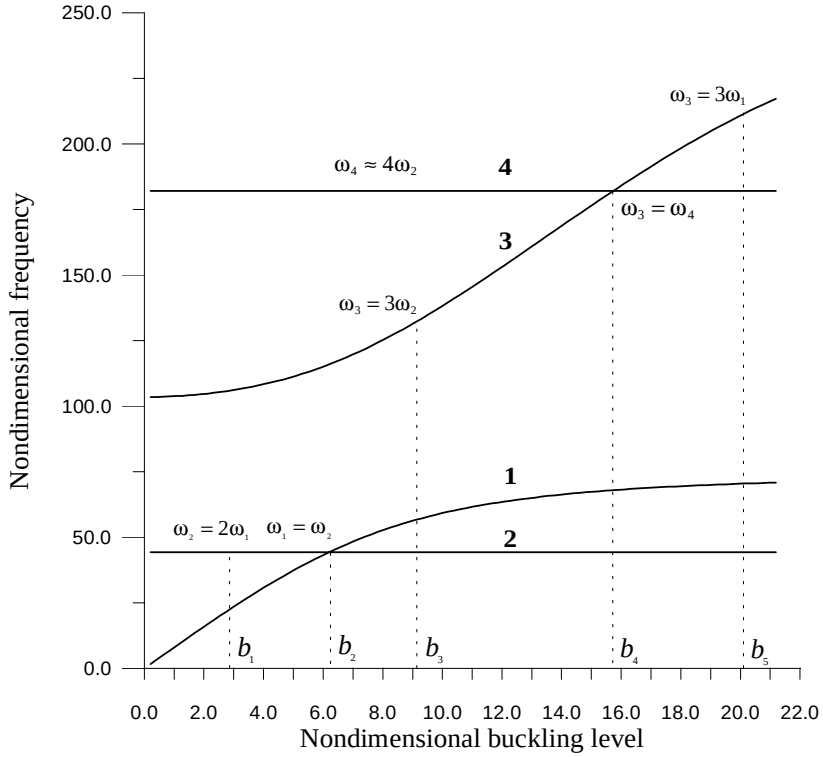

Figure 6.1: Variation of the lowest four nondimensional natural frequencies with the nondimensional buckling level.

we develop a uniform asymptotic expansion for the response of the beam to a primary resonance of a mode that is not involved in any internal resonance with any other mode.

6.1.1 Discretization Approach

To obtain a single–mode Galerkin discretization, we let

$$v(x,t) \approx \phi(x)q(t) \tag{6.4}$$

where $\phi(x)$ is the nth eigenmode given by Eq. (5.14). Substituting Eqs. (5.14) and (6.4) into Eq. (6.2), multiplying the result with $\phi(x)$, and integrating from $x = 0$ to $x = 1$, we

obtain the following nonlinear ordinary–differential equation governing the nth generalized coordinate:

$$\ddot{q} + \omega^2 q = -c\dot{q} + b\alpha_2 q^2 + \alpha_3 q^3 + f\cos(\Omega t) \tag{6.5}$$

where

$$\alpha_2 = \pi\left(\int_0^1 \phi' \sin 2\pi x dx\right)\left(\int_0^1 \phi''\phi dx\right) + \pi^2\left(\int_0^1 \phi\cos 2\pi x dx\right)\left(\int_0^1 (\phi')^2 dx\right) \tag{6.6}$$

$$\alpha_3 = \frac{1}{2}\left(\int_0^1 \phi''\phi dx\right)\left(\int_0^1 (\phi')^2 dx\right) = -\frac{1}{2}\left(\int_0^1 (\phi')^2 dx\right)^2 \tag{6.7}$$

and

$$f = \int_0^1 F(x)\phi(x)dx \tag{6.8}$$

For the case of primary resonance of the nth mode, we assume that Ω and ω differ only by a small detuning $\epsilon^2\sigma$; that is, $\Omega = \omega + \epsilon^2\sigma$. In order that the nonlinearity balance the effects of the damping and the excitation, we scale them so that they appear at the same time in the same modulation equations. Thus, we replace c and F with $\epsilon^2 c$ and $\epsilon^3 F$.

To determine a second–order uniform expansion of the solution of Eq. (6.5) by using the method of multiple scales, we introduce the time scales

$$T_0 = t,\ T_1 = \epsilon t,\ \text{ and }\ T_2 = \epsilon^2 t \tag{6.9}$$

We note that, because secular terms arise at $O(\epsilon^3)$, the solution does not depend on the scale T_1. Hence, we seek the solution of Eq. (6.5) in the form

$$q(t;\epsilon) = \epsilon q_1(T_0, T_2) + \epsilon^2 q_2(T_0, T_2) + \epsilon^3 q_3(T_0, T_2) + \ldots \tag{6.10}$$

In terms of the T_n, the time derivatives can be expressed as

$$\frac{d}{dt} = D_0 + \epsilon^2 D_2 + \ldots \ \text{ and } \ \frac{d^2}{dt^2} = D_0^2 + 2\epsilon^2 D_0 D_2 + \ldots \tag{6.11}$$

where $D_n \equiv \partial/\partial T_n$. Substituting Eqs. (6.9)–(6.11) into Eq. (6.5) and equating coefficients of like powers of ϵ yields

Order ϵ:

$$\mathcal{D}(q_1) = D_0^2 q_1 + \omega^2 q_1 = 0 \tag{6.12}$$

Order ϵ^2:

$$\mathcal{D}(q_2) = b\alpha_2 \; q_1^2 \tag{6.13}$$

Order ϵ^3:

$$\mathcal{D}(q_3) = -cD_0 q_1 - 2D_0 D_2 q_1 + 2b\alpha_2 q_1 q_2 + \alpha_3 q_1^3 + f\cos(\Omega T_0) \tag{6.14}$$

The solution of Eq. (6.12) can be written as

$$q_1(T_0, T_2) = A(T_2)e^{i\omega T_0} + \overline{A}(T_2)e^{-i\omega T_0} \tag{6.15}$$

where the overbar denotes the complex conjugate and the complex–valued amplitude A will be determined by imposing the solvability condition at third order. Substituting Eq. (6.15) into Eq. (6.13) yields

$$\mathcal{D}(q_2) = b\alpha_2 \; \left[A^2 e^{2i\omega T_0} + A\overline{A}\right] + cc \tag{6.16}$$

The solution of Eq. (6.16) can be expressed as

$$q_2(T_0, T_2) = -\frac{b\alpha_2 A^2}{3\omega^2} e^{2i\omega T_0} + \frac{b\alpha_2}{\omega^2} A\overline{A} + cc \tag{6.17}$$

Substituting Eqs. (6.15) and (6.17) into Eq. (6.14) yields

$$\begin{aligned}\mathcal{D}(q_3) = \Bigg\{ &- 2i\omega \left(D_2 A + \mu A\right) + \left(\frac{10b^2\alpha_2^2}{3\omega^2} + 3\alpha_3\right) A^2\overline{A} \\ &+ \frac{f}{2} e^{i\sigma T_2} \Bigg\} e^{i\omega T_0} + cc + NST\end{aligned} \tag{6.18}$$

where $2\mu = c$. Eliminating the terms that produce secular terms from Eq. (6.18) yields the complex–valued modulation equation

$$2i\omega\left(D_2 A + \mu A\right) = 8\omega\widetilde{\alpha}_e A^2\overline{A} + \frac{1}{2}fe^{i\sigma T_2} \tag{6.19}$$

where the effective nonlinearity coefficient $\tilde{\alpha}_e$ is given by

$$\widetilde{\alpha}_e = \frac{1}{8\omega}\left(\frac{10b^2\alpha_2^2}{3\omega^2} + 3\alpha_3\right) \tag{6.20}$$

Expressing A in the polar form $A = \frac{1}{2}ae^{i\beta}$, letting $\gamma = \sigma T_2 - \beta$, and separating real and imaginary parts in Eq. (6.19), we obtain the real–valued modulation equations

$$a' = -\mu a + \frac{f}{2\omega}\sin\gamma \tag{6.21}$$

$$a\gamma' = a\sigma + \widetilde{\alpha}_e a^3 + \frac{f}{2\omega}\cos\gamma \tag{6.22}$$

where the prime indicates the derivative with respect to T_2. In terms of a and γ, the deflection, to the second approximation, is expressed as

$$v(x,t) = \left\{a\cos(\Omega t - \gamma) + \frac{b\alpha_2}{6\omega^2}a^2\left[3 - \cos 2(\Omega t - \gamma)\right] + ...\right\}\phi(x) \tag{6.23}$$

The approximate nondimensional dynamic moment and shear force in the beam are given, respectively, by

$$M(x,t) = -\left\{a\cos(\Omega t - \gamma) + \frac{b\alpha_2}{6\omega^2}a^2\left[3 - \cos 2(\Omega t - \gamma)\right] + ...\right\}\phi''(x) \tag{6.24}$$

$$T(x,t) = -\left\{a\cos(\Omega t - \gamma) + \frac{b\alpha_2}{6\omega^2}a^2\left[3 - \cos 2(\Omega t - \gamma)\right] + ...\right\}\phi'''(x) \tag{6.25}$$

where the 'technical' convention for the signs was adopted. The relationships between the dimensional and nondimensional moment and shear force are, respectively,

$$\hat{M}(x,t) = \frac{EIr}{\ell^2}M \quad \text{and} \quad \hat{T}(x,t) = \frac{EIr}{\ell^3}T \tag{6.26}$$

Letting $a' = 0$ and $\gamma' = 0$ in Eqs. (6.21) and (6.22), we obtain the following frequency–response equation characterizing periodic responses:

$$\sigma = -\widetilde{\alpha}_e a^2 \pm \left(\frac{f^2}{4\omega^2 a^2} - \mu^2 \right)^{\frac{1}{2}} \tag{6.27}$$

We observe that the frequency–response curves exhibit a softening– or hardening–type behavior depending on whether $\widetilde{\alpha}_e$ is positive or negative.

6.1.2 Direct Approach

In this section, we apply the method of multiple scales directly to the integro–partial–differential equation and boundary conditions. We seek the solution of Eqs. (6.2) and (6.3) in the form

$$v(x,t;\epsilon) = \epsilon v_1(x,T_0,T_2) + \epsilon^2 v_2(x,T_0,T_2) + \epsilon^3 v_3(x,T_0,T_2) + \dots \tag{6.28}$$

Substituting Eq. (6.28) into Eqs. (6.2) and (6.3), using Eqs. (6.9) and (6.11), and equating coefficients of like powers of ϵ, we obtain

Order ϵ:

$$\mathcal{L}(v_1) = D_0^2 v_1 + v_1^{iv} + 4\pi^2 v_1'' - 2b^2\pi^3 \cos 2\pi x \int_0^1 v_1' \sin 2\pi x dx = 0 \tag{6.29}$$

Order ϵ^2:

$$\mathcal{L}(v_2) = b\pi v_1'' \int_0^1 v_1' \sin 2\pi x dx + b\pi^2 \cos 2\pi x \int_0^1 (v_1')^2 dx \tag{6.30}$$

Order ϵ^3:

$$\mathcal{L}(v_3) = -2D_0 D_2 v_1 - cD_0 v_1 + 2b\pi^2 \cos 2\pi x \int_0^1 v_1' v_2' dx$$

$$+b\pi\left[v_1''\int_0^1 v_2'\sin 2\pi x dx + v_2''\int_0^1 v_1'\sin 2\pi x dx\right]$$
$$+\frac{1}{2}v_1''\int_0^1 v_1'^2 dx + F(x)\cos(\Omega t) \tag{6.31}$$

The boundary conditions at all orders are given by

$$v_j = 0 \ \text{ and } \ v_j' = 0 \ \text{ at } \ x = 0 \ \text{ and } \ 1, \ \ j = 1, 2, 3. \tag{6.32}$$

The first–order problem, given by Eqs. (6.29) and (6.32), is identical to the linear eigenvalue problem. Because in the presence of damping all modes that are not directly or indirectly excited decay with time (Nayfeh and Mook, 1979), the solution of Eqs. (6.29) and (6.32) is assumed to consist of the directly excited mode only; that is,

$$v_1 = A(T_2)e^{i\omega T_0}\phi(x) + \overline{A}(T_2)e^{-i\omega T_0}\phi(x) \tag{6.33}$$

Substituting Eq. (6.33) into Eq. (6.30) yields

$$\mathcal{L}(v_2) = b\Big[A^2 e^{2i\omega T_0} + A\overline{A}\Big]\left\{\pi^2\cos 2\pi x\int_0^1(\phi')^2 dx + \pi\phi''\int_0^1\sin 2\pi x\phi' dx\right\} + cc \tag{6.34}$$

The solution of Eqs. (6.34) and (6.32) can be expressed as

$$v_2(x, T_0, T_2) = bA^2 e^{2i\omega T_0}\Psi_2(x) + bA\overline{A}\Psi_1(x) + cc \tag{6.35}$$

where $\Psi_1(x)$ and $\Psi_2(x)$ are solutions of the boundary–value problems

$$M(\Psi_i; 2\omega\delta_{2i}) = \kappa(x) \tag{6.36}$$

$$\Psi_i = 0 \ \text{ and } \ \Psi_i' = 0 \ \text{ at } \ x = 0 \ \text{ and } \ 1 \text{ for } i = 1 \text{ and } 2 \tag{6.37}$$

where δ_{ij} denotes the Kronecker delta. Here, the linear differential operator $M(\Psi;\omega)$ is defined by

$$M(\Psi;\omega) = \Psi^{iv} + 4\pi^2\Psi'' - \omega^2\Psi - 2b^2\pi^3\cos 2\pi x\int_0^1\Psi'\sin 2\pi x dx \tag{6.38}$$

and the right–hand side of Eq. (6.36) is given by

$$\kappa(x) = \pi^2 \cos 2\pi x \int_0^1 (\phi')^2 dx + \pi\phi'' \int_0^1 \sin 2\pi x \phi' dx \tag{6.39}$$

The solutions for Ψ_1 and Ψ_2 are determined by using the method of undetermined coefficients. The result is

$$\begin{aligned}\Psi_1(x) = {} & d_1 \sin 2\pi x + d_2 \cos 2\pi x + d_3 x + d_4 + d_5 x \sin 2\pi x \\ & - \frac{c_1 \pi}{\lambda_1^2 - 4\pi^2} \left(\int_0^1 \sin 2\pi x \phi' dx \right) \left\{ \sin \lambda_1 x + \frac{c_2}{c_1} \cos \lambda_1 x \right. \\ & \left. - \frac{c_3}{c_1} \frac{\lambda_1^2 - 4\pi^2}{\lambda_2^2 + 4\pi^2} \left(\sinh \lambda_2 x + \frac{c_4}{c_3} \cosh \lambda_2 x \right) \right\}\end{aligned} \tag{6.40}$$

$$\begin{aligned}\Psi_2(x) = {} & s_1 \sin \zeta_1 x + s_2 \cos \zeta_1 x + s_3 \sinh \zeta_2 x + s_4 \cosh \zeta_2 x + s_5 \cos 2\pi x \\ & - \frac{c_1 \lambda_1^2 \pi}{\lambda_1^4 - 4\pi^2 \lambda_1^2 - 4\omega^2} \left(\int_0^1 \sin 2\pi x \phi' dx \right) \left\{ \sin \lambda_1 x + \frac{c_2}{c_1} \cos \lambda_1 x \right. \\ & \left. - \frac{c_3 \lambda_2^2}{c_1 \lambda_1^2} \frac{\lambda_1^4 - 4\pi^2 \lambda_1^2 - 4\omega^2}{\lambda_2^4 + 4\pi^2 \lambda_2^2 - 4\omega^2} \left(\sinh \lambda_2 x + \frac{c_4}{c_3} \cosh \lambda_2 x \right) \right\}\end{aligned} \tag{6.41}$$

where

$$\zeta_{1,2} = \left\{ \pm 2\pi^2 + 2\sqrt{\pi^4 + \omega^2} \right\}^{\frac{1}{2}} \tag{6.42}$$

and the d_i and s_i are determined by solving linear algebraic equations obtained by requiring that Eqs. (6.40) and (6.41) satisfy the differential equations and the boundary conditions, Eqs. (6.36) and (6.37).

Substituting Eqs. (6.33) and (6.35) into Eq. (6.31) yields

$$\mathcal{L}(v_3) = -\left\{ 2i\omega \left(D_2 A + \mu A \right) - A^2 \overline{A} \chi(x) - \frac{1}{2} F(x) e^{i\sigma T_2} \right\} e^{i\omega T_0} + cc + NST \tag{6.43}$$

where

$$\begin{aligned}\chi(x) = {} & 2\pi^2 b^2 \cos 2\pi x \int_0^1 \phi' \left(2\Psi_1' + \Psi_2' \right) dx \\ & + \pi b^2 \phi'' \int_0^1 \sin 2\pi x \left(2\Psi_1' + \Psi_2' \right) dx + \frac{3}{2} \phi'' \int_0^1 (\phi')^2 dx \\ & + \pi b^2 \left(2\Psi_1'' + \Psi_2'' \right) \int_0^1 \sin 2\pi x \phi' dx\end{aligned} \tag{6.44}$$

The solvability condition of Eqs. (6.43) and (6.32) demands that the right–hand side of Eq. (6.43) be orthogonal to every solution of the adjoint of the corresponding homogeneous problem. Because the system is self–adjoint, the adjoints are given by $\phi_j(x)\,\exp(\pm i\omega_j T_0)$. Multiplying the right–hand side of Eq. (6.43) with $\phi_n(x)\exp(-i\omega_n T_0)$ and integrating the result from $x=0$ to $x=1$, we obtain the following solvability condition:

$$2i\omega\left(D_2A+\mu A\right)=8\omega\alpha_e A^2\overline{A}+\frac{1}{2}fe^{i\sigma T_2} \tag{6.45}$$

where f is given by Eq. (6.8) and the effective nonlinearity coefficient α_e is given by

$$\alpha_e=\frac{1}{8\omega}\int_0^1\chi(x)\phi(x)dx \tag{6.46}$$

Equation (6.46) can be rewritten as

$$\alpha_e=\frac{1}{8\omega}\left(b^2\int_0^1\varsigma(x)\phi(x)dx+3\alpha_3\right) \tag{6.47}$$

where

$$\begin{aligned}\varsigma(x)=\;&\varphi''\int_0^1\phi'\left(2\Psi_1'+\Psi_2'\right)dx+\phi''\int_0^1\varphi'\left(2\Psi_1'+\Psi_2'\right)dx\\&+\left(2\Psi_1''+\Psi_2''\right)\int_0^1\varphi'\phi'dx\end{aligned} \tag{6.48}$$

α_3 and φ are given by Eqs. (6.7) and (4.35), respectively. Again, the beam exhibits a softening or a hardening behavior, depending on whether α_e is positive or negative.

It follows from Eqs. (6.20) and (6.47) that the $\tilde{\alpha}_e$ and α_e consist of two terms: a term $3\alpha_3/8\omega$ that does not depend explicitly on the buckling level b and a term that is proportional to b^2. The first term $3\alpha_3/8\omega$ is the same in $\tilde{\alpha}_e$ and α_e, is caused by the cubic nonlinearity, and is negative; hence, it produces a hardening behavior. On the other hand, the second term is not the same, is caused by the quadratic nonlinearity, and is positive. Hence, it produces a softening behavior. The effective nonlinearity coefficient depends on the relative magnitudes of the hardening (cubic) and softening (quadratic) terms.

Consequently, there is a possibility of qualitative differences in the effective nonlinearity coefficients depending on whether they are computed by using the discretization or direct approach.

Expressing A in the polar form $A = \frac{1}{2}ae^{i\beta}$ and letting $\gamma = \sigma T_2 - \beta$, we obtain the real–valued modulation equations

$$a' = -\mu a + \frac{f}{2\omega}\sin\gamma \tag{6.49}$$

$$a\gamma' = a\sigma + \alpha_e a^3 + \frac{f}{2\omega}\cos\gamma \tag{6.50}$$

The deflection produced by the direct approach, to the second approximation, can be expressed as

$$v(x,t) = a\cos(\Omega t - \gamma)\phi(x) + \frac{1}{2}ba^2\Big[\Psi_1(x) + \cos 2(\Omega t - \gamma)\Psi_2(x)\Big] + ... \tag{6.51}$$

From Eq. (6.51), we obtain the approximate nondimensional dynamic moment and shear force in the beam as

$$M(x,t) = -\Big\{a\cos(\Omega t - \gamma)\phi''(x) + \frac{1}{2}ba^2\Big[\Psi_1''(x) + \cos 2(\Omega t - \gamma)\Psi_2''(x)\Big]\Big\} + ... \tag{6.52}$$

$$T(x,t) = -\Big\{a\cos(\Omega t - \gamma)\phi'''(x) + \frac{1}{2}ba^2\Big[\Psi_1'''(x) + \cos 2(\Omega t - \gamma)\Psi_2'''(x)\Big]\Big\} + ... \tag{6.53}$$

The frequency–response equation for periodic oscillations can be obtained from Eqs. (6.49) and (6.50). The result is

$$\sigma = -\alpha_e a^2 \pm \left(\frac{f^2}{4\omega^2 a^2} - \mu^2\right)^{\frac{1}{2}} \tag{6.54}$$

An approximation to the nonlinear normal mode that reduces to the nth linear mode as the nonlinearity vanishes (i.e., $\epsilon \to 0$) can be obtained from Eq. (6.51) by replacing Ω with ω_n, and a and γ with $a = a_0$ =constant and $\gamma = a_0^2\alpha_e t - \gamma_0$. The result is

$$\begin{aligned} V_n(x,t) = {} & \phi_n(x)a_0\cos\Big[(\omega_n - a_0^2\alpha_e)t + \gamma_0\Big] \\ & + \frac{1}{2}ba_0^2\Big\{\Psi_1(x) + \Psi_2(x)\cos 2\Big[(\omega_n - a_0^2\alpha_e)t + \gamma_0\Big]\Big\} + ... \end{aligned} \tag{6.55}$$

6.1.3 Numerical Results

Next, we contrast the frequency–response equation (6.27) obtained with the single–mode discretization with Eq. (6.54). The only difference is the *effective nonlinearity coefficient*. Using a symbolic manipulator (MATHEMATICA), we evaluated the integrals in Eqs. (6.6), (6.7), and (6.44) in closed form and then substituted the pertinent eigenvalues into the associated eigenmodes to minimize the effects of the numerical approximations. Then, we computed the effective nonlinearity coefficients by using Eqs. (6.20) and (6.46) over a broad range of the buckling level b for the first two modes.

In Fig. 6.2(a), we show variation of the effective nonlinearity coefficient with the nondimensional buckling level for the first mode. Both effective nonlinearity coefficients are positive for $b < 15.20$. We note that for low buckling levels, the natural frequency of the first mode is very small and the dynamic displacement is not necessarily small relative to the buckling deflection. Hence, the governing equation, Eq. (6.1), is not valid for describing resonant vibrations of the first mode for low buckling levels. However, for high buckling levels ($b > 15.20$), the discretization approach predicts a hardening–type nonlinearity in disagreement with the softening–type nonlinearity predicted by the direct approach. Then, we computed an equivalent α_2, denoted by $\hat{\alpha}_2$, that would make $\tilde{\alpha}_e = \alpha_e$. In Fig. 6.3(b), we show variation of $\hat{\alpha}_2$, α_2 and α_3 with the nondimensional buckling level. We note that at the buckling level (b =15.20) where the effective nonlinearity coefficient $\tilde{\alpha}_e$ obtained with the discretization approach changes sign, α_2 reaches a maximum. Above this buckling level, α_2 decreases, whereas $\hat{\alpha}_2$ increases monotonically. Hence, the discretization underestimates the softening effect in the beam for all buckling levels of interest. For $b < b_c$, this quantitative discrepancy results in a lower effective nonlinearity coefficient obtained with the discretization approach. For $b > b_c$, the consequence is a qualitative difference between the effective nonlinearity coefficients.

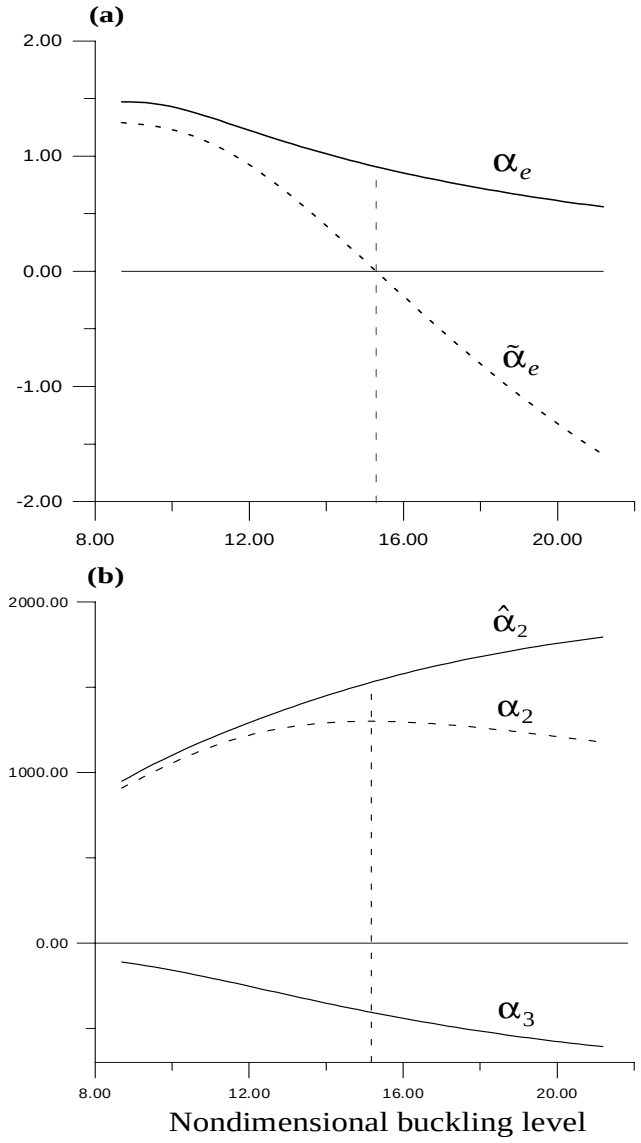

Figure 6.2: Primary resonance of the first mode. Variation of: (a) the effective nonlinearity coefficients and (b) the coefficients $\hat{\alpha}_2$, α_2, and α_3 with the nondimensional buckling level. Solid (dashed) lines denote results obtained with the direct (discretization) approach.

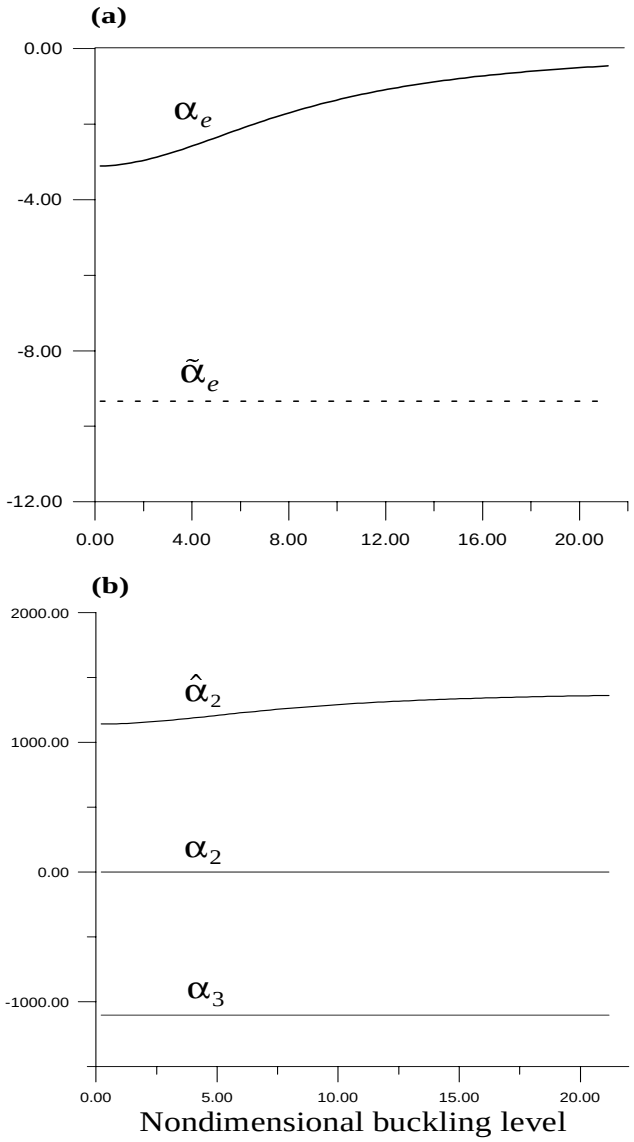

Figure 6.3: Primary resonance of the second mode. Variation of: (a) the effective nonlinearity coefficients and (b) the coefficients $\hat{\alpha}_2$, α_2, and α_3 with the nondimensional buckling level. Solid (dashed) lines denote results obtained with the direct (discretization) approach.

For the second mode, the effective nonlinearity coefficients obtained with both approaches are of the hardening–type, as evident from Fig. 6.3(a). We note that the effective nonlinearity coefficients obtained with discretization for all even modes are independent of the buckling level. In fact, α_2 in Eq. (6.20) is zero for even modes. In contrast, the effective nonlinearity coefficient obtained with the direct approach decreases with increasing buckling level for the second mode. This result is consistent with Fig. 6.3(b). We note, in fact, that $\hat{\alpha}_2$ increases monotonically with increasing buckling level.

In Fig. 6.4, we show the frequency–response curves obtained with the direct and discretization approaches for the case of primary resonance of the first mode when $b = 17.21$, $f = 10$, and $\mu = 0.1$. Because $b > 15.20$, consistent with Fig. 6.2(a), the direct approach predicts a softening–type curve, whereas the discretization approach predicts a hardening–type one. In Fig. 6.5(a)–(c), we contrast, respectively, the corresponding nonlinear dynamic response and the moment and shear force diagrams obtained with both approaches when $b = 17.21$, $f = 10$, $a = 1$, and $\mu = 0.1$. We observe that the highest quantitative differences are localized in the regions close to the boundaries.

In Fig. 6.6, we show the frequency–response curves obtained with the direct and discretization approaches for the case of primary resonance of the second mode when $b = 5.45$, $f = 10$, and $\mu = 0.1$. Both curves are of the hardening–type. However, the discretization greatly overestimates the effective nonlinearity coefficient of the beam. In Fig. 6.7(a)–(c), we show the corresponding nonlinear dynamic response and moment and shear diagrams when $b = 5.45$, $f = 10$, $a = 1$, and $\mu = 0.1$. In this case, the quantitative differences between the results obtained with both approaches are markedly larger than those found in the case of primary resonance of the first mode.

In Fig. 6.8, we contrast the frequency–response curves obtained with the direct and discretization approaches for the case of primary resonance of the third mode when $b = 5.45$,

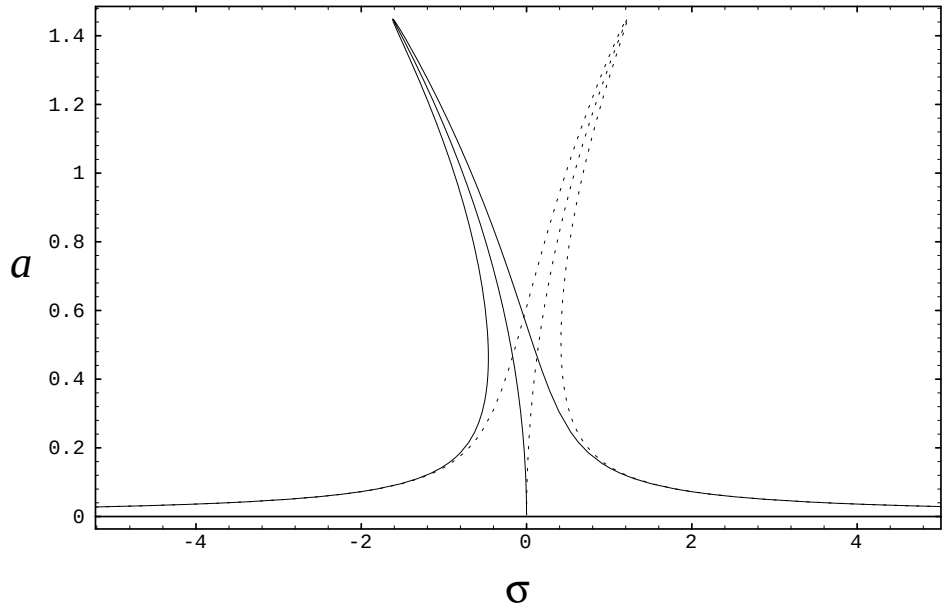

Figure 6.4: Frequency–response curves for the case of primary resonance of the first mode when $b = 17.21$, $f = 10$, and $\mu = 0.1$. Solid (dashed) lines indicate results obtained with the direct (discretization) approach.

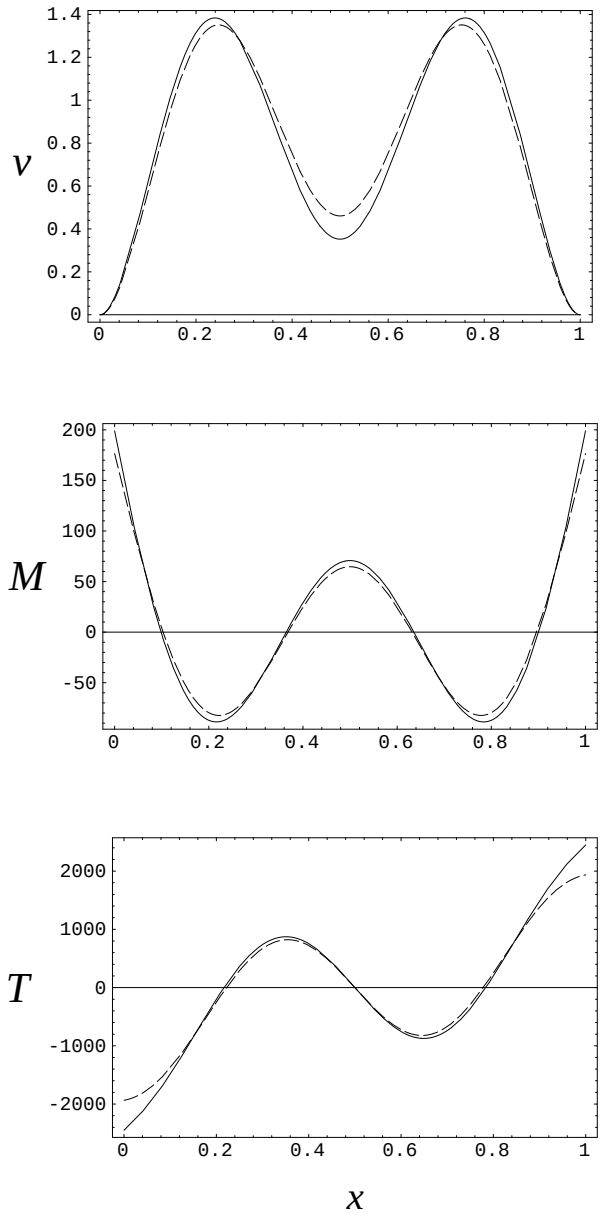

Figure 6.5: (a) Nonlinear response, (b) dynamic moment, and (c) dynamic shear force for the case of primary resonance of the first mode when $b = 17.21$, $f = 10$, $a = 1$, $\mu = 0.1$, and $(\Omega t - \gamma) = 2n\pi$, $n = 0, 1, 2, \cdots$. Solid (dashed) lines indicate results obtained with the direct (discretization) approach.

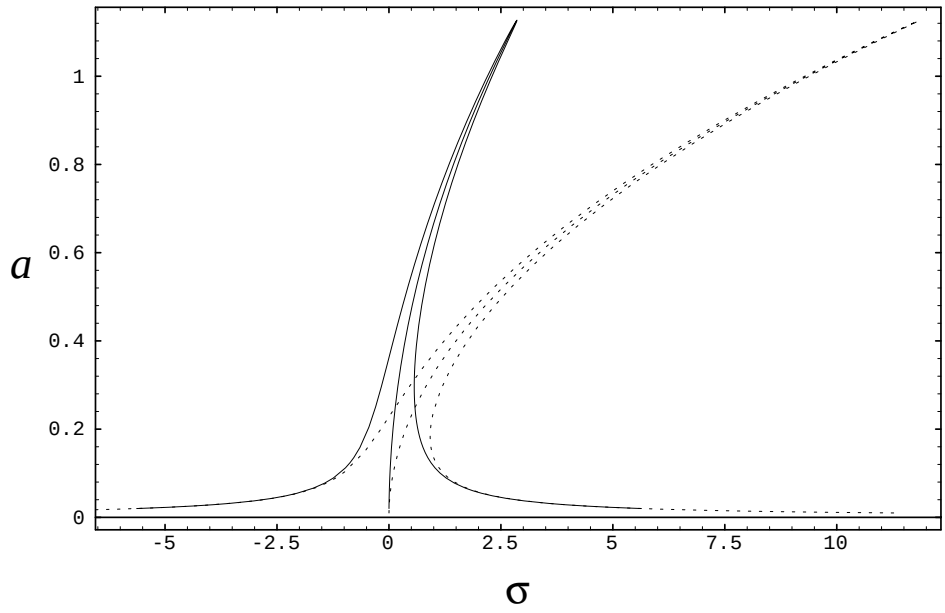

Figure 6.6: Frequency–response curves for the case of primary resonance of the second mode when $b = 5.45$, $f = 10$, and $\mu = 0.1$. Solid (dashed) lines indicate results obtained with the direct (discretization) approach.

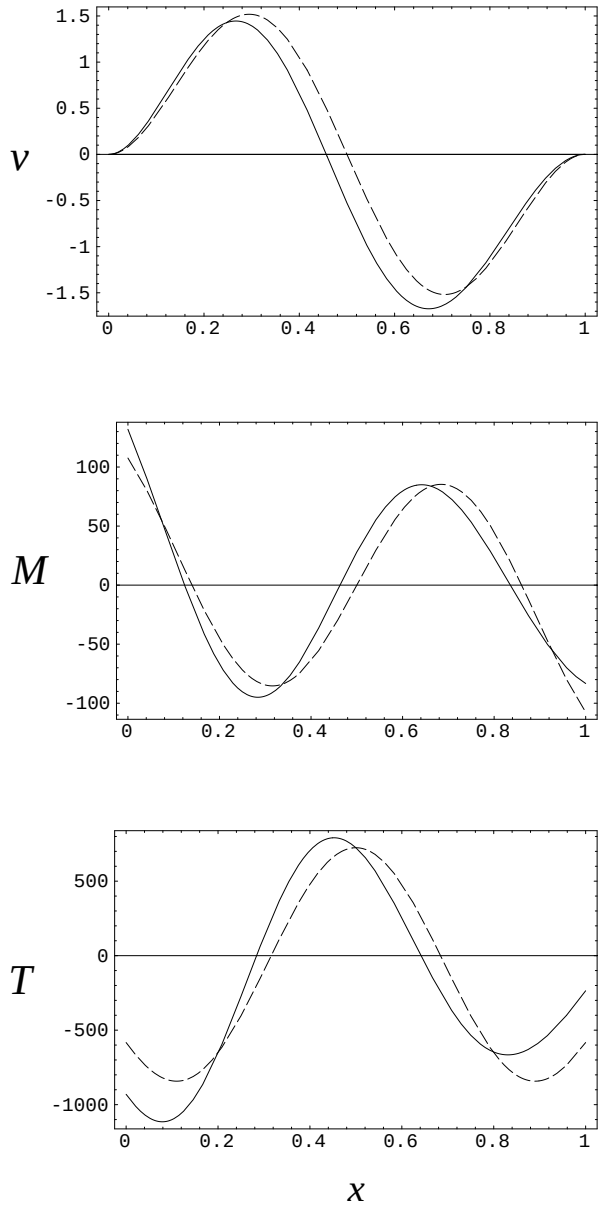

Figure 6.7: (a) Nonlinear response, (b) dynamic moment, and (c) dynamic shear force for the case of primary resonance of the second mode when $b = 5.45$, $f = 10$, $a = 1$, $\mu = 0.1$, and $(\Omega t - \gamma) = 2n\pi$, $n = 0, 1, 2, \cdots$. Solid (dashed) lines indicate results obtained with the direct (discretization) approach.

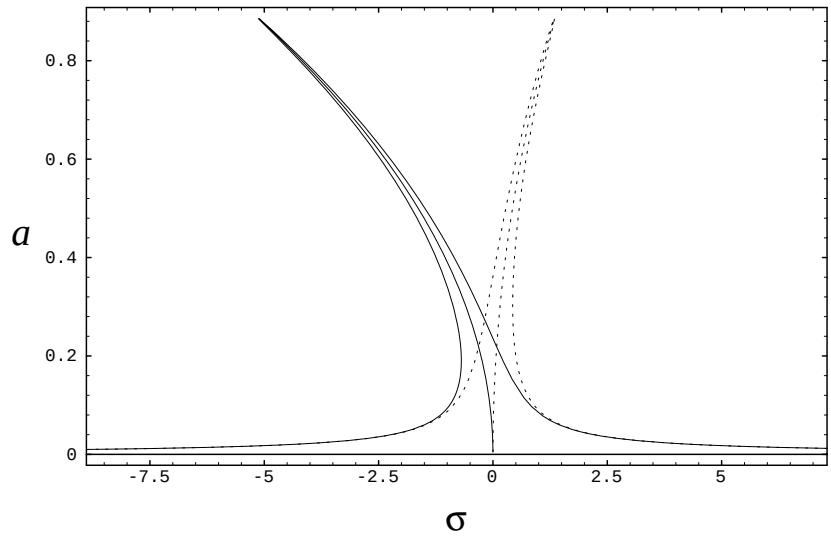

Figure 6.8: Frequency–response curves for the case of primary resonance of the third mode when $b = 5.45$, $f = 20$, and $\mu = 0.1$. Solid (dashed) lines indicate results obtained with the direct (discretization) approach.

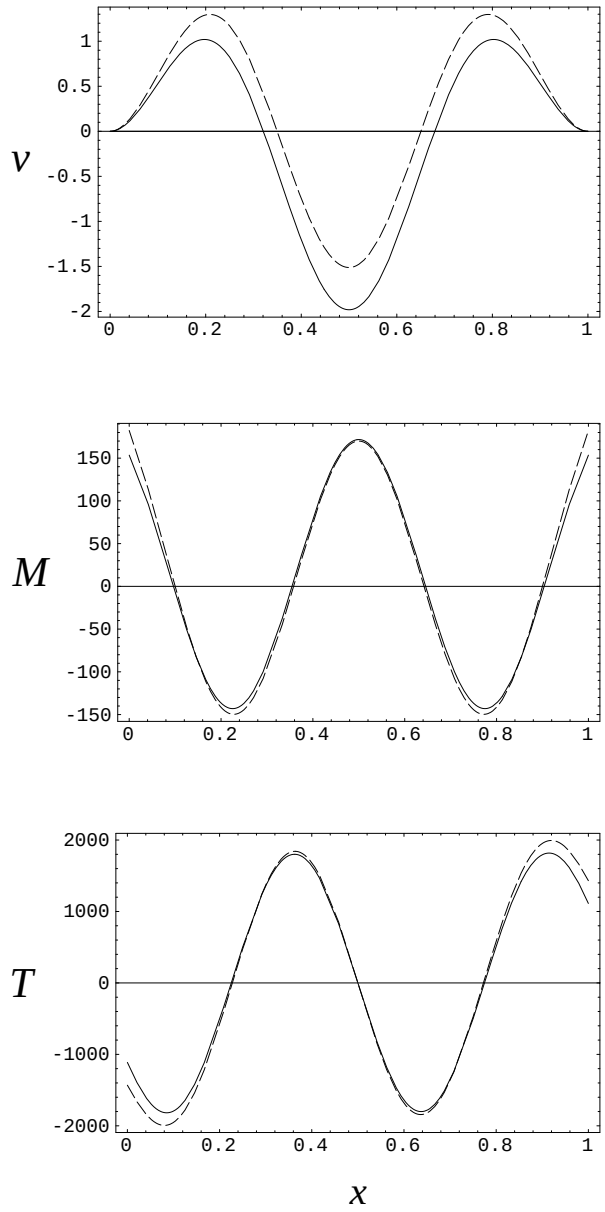

Figure 6.9: (a) Nonlinear response, (b) dynamic moment, and (c) dynamic shear force for the case of primary resonance of the third mode when $b = 5.45$, $f = 20$, $a = 0.8$, $\mu = 0.1$, and $(\Omega t - \gamma) = 2n\pi$, $n = 0, 1, 2, \cdots$. Solid (dashed) lines indicate results obtained with the direct (discretization) approach.

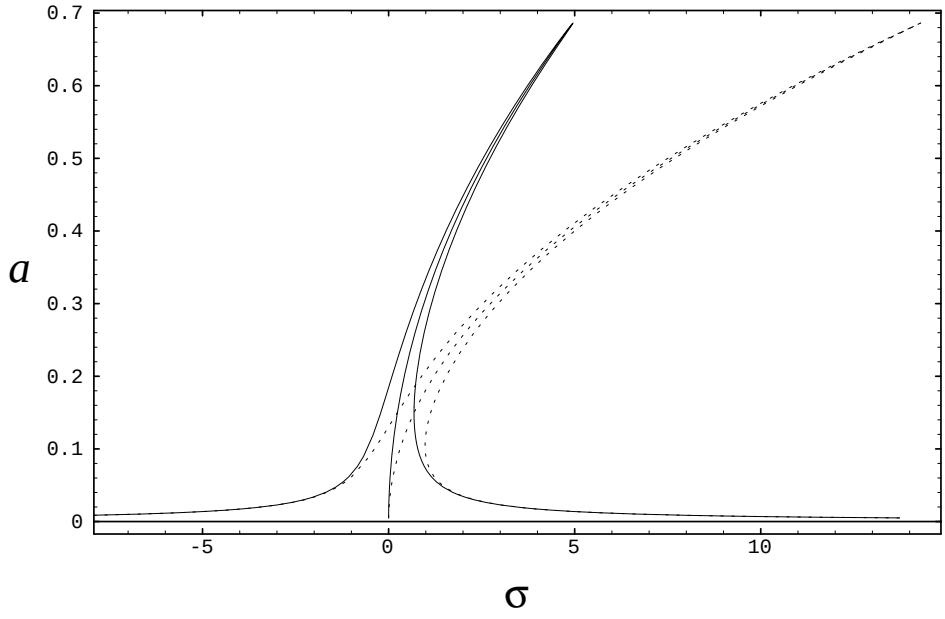

Figure 6.10: Frequency–response curves for the case of primary resonance of the fourth mode when $b = 5.45$, $f = 25$, and $\mu = 0.1$. Solid (dashed) lines indicate results obtained with the direct (discretization) approach.

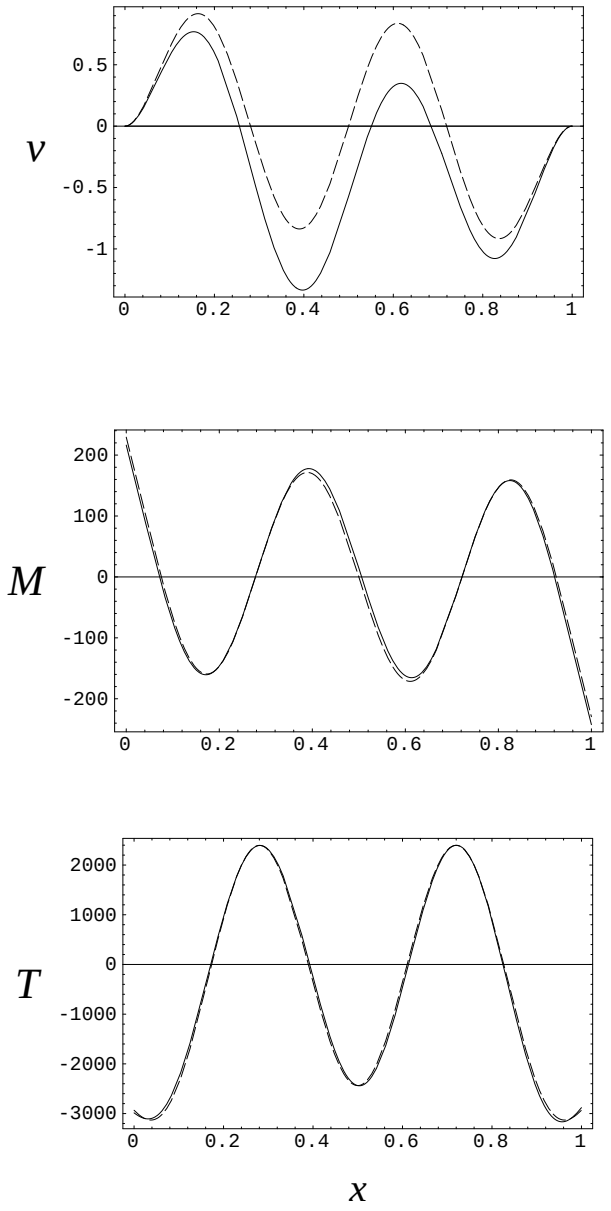

Figure 6.11: (a) Nonlinear response, (b) dynamic moment, and (c) dynamic shear force for the case of primary resonance of the fourth mode when $b = 5.45$, $f = 25$, $a = 0.6$, $\mu = 0.1$, and $(\Omega t - \gamma) = 2n\pi$, $n = 0, 1, 2, \cdots$. Solid (dashed) lines indicate results obtained with the direct (discretization) approach.

$f = 20$, and $\mu = 0.1$. The direct approach predicts a softening–type nonlinearity, whereas the discretization approach predicts a hardening–type nonlinearity. In Fig. 6.9(a)–(c), we show the corresponding nonlinear dynamic response and moment and shear diagrams when $b = 5.45$, $f = 20$, $a = 0.8$, and $\mu = 0.1$. In this case, as in the case of primary resonance of the first mode, the quantitative differences between the results obtained with both approaches are concentrated in some layers near the boundaries.

In Fig. 6.10, we show the frequency–response curves obtained with the direct and discretization approaches for the case of primary resonance of the fourth mode when $b = 5.45$, $f = 25$, and $\mu = 0.1$. Both approaches predict a hardening–type nonlinearity. However, as in the case of primary resonance of the second mode, the discretization approach predicts a larger effective nonlinearity coefficient. In Fig. 6.11(a)–(c), we show the corresponding nonlinear dynamic response and moment and shear diagrams when $b = 5.45$, $f = 25$, $a = 0.6$, and $\mu = 0.1$. Interestingly, in this case, the quantitative differences in the internal forces of the beam obtained by using the two approaches are not significant.

From these results it appears that the qualitative and quantitative differences patterns in the results obtained with the direct and discretization approaches are consistent for modes of the same character (symmetric or antisymmetric).

6.2 Direct Approach to Period–Doubling Bifurcation

We develop a theoretical model for predicting the onset of period–doubling bifurcations in single–mode responses because we observed such bifurcations experimentally. Kreider (1995) documented unstable period–doubled solutions and conjectured that single–mode periodic motions undergo a *subcritical* period–doubling bifurcation. Our experiments indicate that a period–doubling bifurcation is the most likely candidate for a bifurcation

route to single–mode chaotic motions. In fact, we observed that, by sweeping backward the excitation frequency, the periodic response became chaotic, with a peak at one–half the excitation frequency being clearly visible in the response spectrum. As the excitation frequency was decreased further, the chaotic response became periodic with twice the fundamental period. Therefore, we can reasonably conjecture a reverse period–doubling bifurcation from the chaotic response to the fundamental periodic motion. However, the transition from the periodic to the chaotic motion is not fully clear in the experiments.

In the literature, it has been a common practice to study period–doubling bifurcations in buckled beams by using discretized equations. The experiments were conducted at buckling levels where the discretization fails to predict the correct dynamics of the beam. Hence, to construct a reliable theoretical model for predicting the onset of the period–doubling bifurcation in this buckling range, we attack the original integro–partial–differential equation and boundary conditions.

6.2.1 The Variational Equations

The governing equation of motion and boundary conditions are given by Eqs. (6.2) and (6.3). We express the response that bifurcates from the fundamental periodic solution, Eq. (6.51), as

$$V(x,t) = v(x,t) + w(x,t) \tag{6.56}$$

Substituting Eq. (6.56) into Eqs. (6.2) and (6.3) yields

$$\begin{aligned}\ddot{w} + c\dot{w} + w^{iv} + 4\pi^2 w'' - 2\pi^3 b^2 \cos 2\pi x \int_0^1 \sin 2\pi x w' dx = \\ +2\pi^2 b \cos 2\pi x \int_0^1 v'w'dx + \frac{1}{2}w'' \int_0^1 (v')^2 dx + v'' \int_0^1 v'w'dx \\ +\pi b v'' \int_0^1 \sin 2\pi x w' dx + \pi b w'' \int_0^1 \sin 2\pi x v' dx\end{aligned}$$

$$+\pi b w'' \int_0^1 \sin 2\pi x w' dx + \pi^2 b \cos 2\pi x \int_0^1 w'^2 dx$$
$$+\frac{1}{2} v'' \int_0^1 w'^2 dx + w'' \int_0^1 v' w' dx + \frac{1}{2} w'' \int_0^1 (w')^2 dx \tag{6.57}$$

$$w = 0 \ \text{ and } \ w' = 0 \ \text{ at } \ x = 0 \ \text{ and } \ 1 \tag{6.58}$$

By dropping the nonlinear terms in Eq. (6.57), we obtain the linear variational equation

$$\ddot{w} + c\dot{w} + w^{iv} + 4\pi^2 w'' - 2\pi^3 b^2 \cos 2\pi x \int_0^1 \sin 2\pi x w' dx =$$
$$+2\pi^2 b \cos 2\pi x \int_0^1 v' w' dx + \frac{1}{2} w'' \int_0^1 (v')^2 dx + v'' \int_0^1 v' w' dx$$
$$+\pi b v'' \int_0^1 \sin 2\pi x w' dx + \pi b w'' \int_0^1 \sin 2\pi x v' dx \tag{6.59}$$

Using Floquet theory, we seek a solution of Eqs. (6.59) and (6.58) in the form:

$$w(x,t) = e^{\nu t} \eta(x,t) \tag{6.60}$$

Substituting Eq. (6.61) into (6.60) yields

$$\ddot{\eta} + \gamma_{11}\dot{\eta} + \gamma_{22}\eta + \eta^{iv} + 4\pi^2 \eta'' - 2\pi^3 b^2 \cos 2\pi x \int_0^1 \sin 2\pi x \eta' dx =$$
$$+\pi b \eta'' \int_0^1 \sin 2\pi x v' dx + 2\pi^2 b \cos 2\pi x \int_0^1 v' \eta' dx$$
$$+b\pi v'' \int_0^1 \sin 2\pi x \eta' dx + v'' \int_0^1 v' \eta' dx + \frac{1}{2} \eta'' \int_0^1 (v')^2 dx \tag{6.61}$$

where $\gamma_{11} = 2(\nu + \mu)$, $\gamma_{22} = \nu^2 + 2\nu\mu$, and $2\mu = c$. Because we are interested in period-doubled disturbances, we let

$$\eta(x,t) = \eta_1(x) \cos(\frac{1}{2}\Omega t - \frac{1}{2}\gamma) + \eta_2(x) \sin(\frac{1}{2}\Omega t - \frac{1}{2}\gamma) \tag{6.62}$$

Substituting Eqs. (6.62) and (6.51) into Eq. (6.61) and equating the coefficient of each of the harmonics on both sides yields

$$\mathcal{N}_1(\eta_1, \eta_2) = 2\pi^2 b \cos 2\pi x \Big\{ \pi b \int_0^1 \sin 2\pi x \delta \eta_1' dx + \frac{1}{2} b a^2 \int_0^1 \Psi_1' \eta_1' dx$$

$$+\frac{1}{2}a\cos\gamma\int_0^1\phi'\eta_1'dx\Big\}+\phi''\Big\{\frac{1}{8}ba^3\cos\gamma\int_0^1\eta_1'\Big[\Psi_2'+2\Psi_1'\Big]dx$$
$$+\frac{1}{2}\pi ba\cos\gamma\int_0^1\sin 2\pi x\eta_1'dx+\frac{1}{2}a^2\int_0^1\phi'\eta_1'dx\Big\}$$
$$+\frac{1}{4}ba^2\Psi_1''\Big\{a\cos\gamma\int_0^1\phi'\eta_1'dx+2\pi b\int_0^1\sin 2\pi x\eta_1'dx\Big\}$$
$$+\frac{1}{8}ba^3\Psi_2''\cos\gamma\int_0^1\phi'\eta_1'dx \tag{6.63}$$

$$\mathcal{N}_2(\eta_1,\eta_2)=2\pi^2b\cos 2\pi x\Big\{\pi b\int_0^1\sin 2\pi x\delta\eta_2'dx+\frac{1}{2}ba^2\int_0^1\Psi_1'\eta_2'dx$$
$$-\frac{1}{2}a\cos\gamma\int_0^1\phi'\eta_2'dx\Big\}-\phi''\Big\{\frac{1}{8}ba^3\cos\gamma\int_0^1\eta_2'\Big[\Psi_2'-2\Psi_1'\Big]dx$$
$$+\pi ba\cos\gamma\int_0^1\sin 2\pi x\eta_2'dx-\frac{1}{2}a^2\int_0^1\phi'\eta_2'dx\Big\}$$
$$-\frac{1}{4}ba^2\Psi_1''\Big\{a\cos\gamma\int_0^1\phi'\eta_2'dx-2\pi b\int_0^1\sin 2\pi x\eta_2'dx\Big\}$$
$$-\frac{1}{8}ba^3\Psi_2''\cos\gamma\int_0^1\phi'\eta_2'dx \tag{6.64}$$

$$\eta_i=0\ \text{ and }\ \eta_i'=0,\quad i=1,2 \tag{6.65}$$

where

$$\mathcal{N}_1(\eta_1,\eta_2)=\eta_1^{iv}+\Lambda_{11}\eta_1''+\Gamma_{11}\eta_1+\Gamma_{12}\eta_2 \tag{6.66}$$

$$\mathcal{N}_2(\eta_1,\eta_2)=\eta_2^{iv}+\Lambda_{22}\eta_2''+\Gamma_{11}\eta_2-\Gamma_{12}\eta_1 \tag{6.67}$$

$$\Lambda_{11}=4\pi^2-\frac{1}{2}b^2a^2\int_0^1\phi'\Psi_1'dx-\frac{1}{2}\pi ba\cos\gamma\int_0^1\sin 2\pi x\phi'dx$$
$$-\frac{1}{4}a^2\int_0^1(\phi')^2dx-\frac{1}{4}ba^3\cos\gamma\int_0^1\phi'\Psi_1'dx$$
$$-\frac{1}{8}ba^3\cos\gamma\int_0^1\phi'\Psi_2'dx \tag{6.68}$$

$$\begin{aligned}\Lambda_{22} = 4\pi^2 - \frac{1}{2}b^2a^2\int_0^1 \phi'\Psi_1' dx + \frac{1}{2}\pi ba\cos\gamma\int_0^1 \sin 2\pi x\phi' dx \\ -\frac{1}{4}a^2\int_0^1 (\phi')^2\, dx + \frac{1}{4}ba^3\cos\gamma\int_0^1 \phi'\Psi_1' dx \\ +\frac{1}{8}ba^3\cos\gamma\int_0^1 \phi'\Psi_2' dx\end{aligned} \tag{6.69}$$

$$\Gamma_{11} = \nu^2 + 2\nu\mu - \frac{1}{4}\Omega^2 \;\text{ and }\; \Gamma_{12} = (\nu+\mu)\Omega \tag{6.70}$$

We observe that the homogeneous boundary–value problems given by Eqs. (6.63) and (6.64) with the associated boundary conditions, Eq. (6.65), admit a nontrivial solution only if the *null space* of the differential problem is not empty. By imposing this condition we obtain an algebraic eigenvalue problem for ν. If $\nu \geq 0$, then the condition for the onset of the period–doubling instability is satisfied. On the other hand, if $\nu < 0$, the period–doubled disturbance decays with time, hence the period–doubling bifurcation does not occur.

The strategy for solving the coupled homogeneous boundary–value problems follows the line of attack we have used thus far in dealing with integro–differential boundary–value problems. First, we consider the associated homogeneous problem given by

$$\mathcal{N}_1(\eta_1, \eta_2) = 0 \tag{6.71}$$

$$\mathcal{N}_2(\eta_1, \eta_2) = 0 \tag{6.72}$$

In order to determine the eigenvalues of this differential problem, we rewrite Eqs. (6.71) and (6.72) as a set of first–order differential equations in the form

$$\mathbf{z}' = \mathcal{A}\mathbf{z} \tag{6.73}$$

and compute the eigenvalues of the matrix $\mathcal{A}$. Because the eigenvalues of the real matrix $\mathcal{A}$ exist in complex conjugate pairs, the homogeneous solutions for the η_i are an eight-term linear combination of the functions sin, cos, sinh, cosh . Upon inspection of the right–hand

sides of Eqs. (6.63) and (6.64), we conclude that their particular solutions can be expressed as

$$\begin{aligned}\eta_{i,p}(x) = {} & n_{i,9}\sin 2\pi x + n_{i,10}\cos 2\pi x + n_{i,11}x\sin 2\pi x + n_{i,12}\sin\lambda_1 x \\ & + n_{i,13}\cos\lambda_1 x + n_{i,14}\sinh\lambda_2 x + n_{i,15}\cosh\lambda_2 x + n_{i,16}\sin\zeta_1 x \\ & + n_{i,17}\cos\zeta_1 x + n_{i,18}\sinh\zeta_2 x + n_{i,19}\cosh\zeta_2 x, \qquad i = 1,2 \end{aligned} \tag{6.74}$$

where $\lambda_{1,2}$ and $\zeta_{1,2}$ are given by Eqs. (5.7) and (6.42). Hence, the general solutions of Eqs. (6.63) and (6.64) can be written as

$$\eta_i(x) = \eta_{i,h}(x) + \eta_{i,p}(x), \quad i = 1,2 \tag{6.75}$$

where the $\eta_{i,h}(x)$, $i = 1,2$ denote the homogeneous solutions. Next, we substitute Eqs. (6.75) into Eqs. (6.63) and (6.64), collect coefficients of like functions, and equate the results to zero. Then, we add, to the resulting algebraic equations, the equations that we obtain by imposing the boundary conditions. In the end, a set of thirty homogeneous algebraic equations in thirty unknowns is obtained. Requiring that the determinant of the matrix associated with these equations be zero yields the characteristic equation for the eigenvalue ν. Because a closed–form solution for the eigenvalues of the matrix A is not available for an arbitrary periodic solution $v(x,t)$ and an arbitrary ν, we implemented in MATHEMATICA a numerical algorithm that seeks the root of the determinant of the matrix in terms of ν by a guess and trial procedure. A symbolic manipulator is preferred because all the integrals involved in the integro–differential equations can be computed in closed form more efficiently than by means of numerical integration and no numerical approximation is introduced.

Chapter 7

Single–Mode Responses: Experiment

In this chapter, we present several frequency–response curves characterizing single–mode oscillations of a buckled beam around its first buckling mode shape for buckling levels where qualitative discrepancies between the discretization and direct approaches exist. These qualitative differences occur for high buckling levels. At high buckling levels, we showed (Fig. 5.3) that an initially straight beam and an imperfect beam with low levels of imperfections behave similarly. Hence, the assumption of the ideal model of an initially straight beam is justified in our theoretical analysis. At the same time, we assured that the unavoidable initial geometric imperfections in the test specimens were of sufficiently low amplitude. We start by discussing the experimental setup.

7.1 Experimental Apparatus

The experimental apparatus is a modified version of the one designed by Kreider (1995). In Figs. 7.1 and 7.2, we show a picture and a schematic of the experimental setup, respectively.

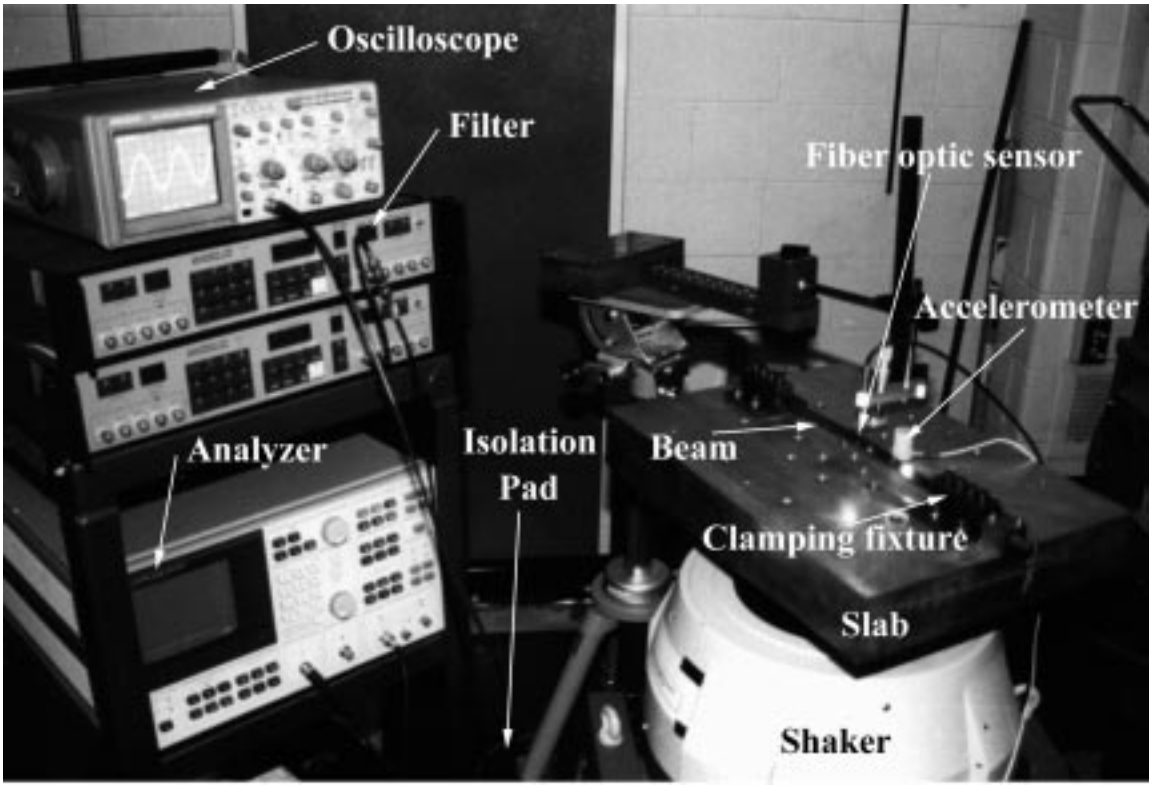

Figure 7.1: Picture of the experimental setup

The setup consists of the test specimen that is clamped to an aluminum slab which is, in turn, fixed on an electrodynamic shaker. A uniform base excitation (imposed displacement) is provided by a Ling Dynamic Systems (LDS) model V722 shaker, with a maximum output force of 922 lbf over the frequency range 5 – 4000 Hz.

To produce single–frequency excitations, we used a Wavetek model 178 waveform synthesizer to drive the shaker through a LDS model PA2000 linear amplifier. To measure the base acceleration, we used a PCB model 308 B02 accelerometer mounted on the slab (see Fig. 7.1), calibrated to produce 1 V per g of acceleration. To measure the displacement of the midspan of the beam, we used a Philtec Series 88, type D fiber optic displacement

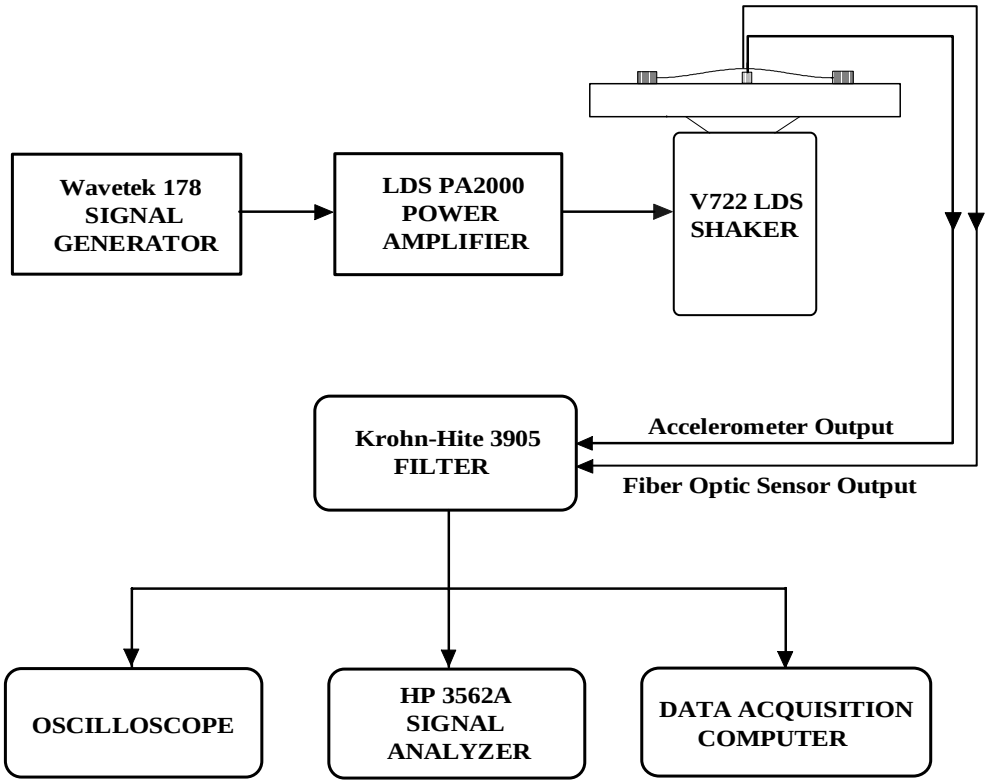

Figure 7.2: Schematic of the experimental setup

sensor, which was mounted by means of a magnetic base on a steel bar clamped on a tripod. The tripod, in turn, was placed on the isolation pad (see Fig. 7.1) so that external environmental vibrations were not likely to be captured by the sensor.

We used a Krohn–Hite model 3905 low–pass/high–pass elliptical filter to filter the 3.5 V DC offset of the fiber optic and the output of the accelerometer, respectively. We monitored time traces and the frequency content either of the excitation or of the beam displacement by using an oscilloscope and a Hewlett Packard 3562A dynamic signal analyzer. We recorded time traces of some of the experimental results on a Macintosh IIfx by using a National Instruments NB–MIO–16X analog–to–digital converter, which constitutes the

Table 7.1: Beam Properties

	Beam I	Beam II
Length, mm	279.171	279.171
Width, mm	19.050	12.700
Thickness, mm	0.808	0.508
Area, mm^2	15.387	6.452
Moment of inertia, mm^4	$8.365\ 10^{-1}$	$1.387\ 10^{-1}$
Radius of gyration, mm	0.233	0.147
Slenderness	1197.294	1903.697
Young modulus, GPa	207	207
Density, kg/m^3	7815	–
$\sqrt{\frac{EI}{m\ell^4}}$	2.451	1.541
Hardness, Vickers	183	555

data acquisition section of the setup. The test specimens are uniform beams with rectangular cross–sections made of two types of steel. Beam I is made of unhardened oil hardening flat stock steel; Beam II is made of blue–tempered steel. The geometric properties of the two beams are given in Table 7.1. The test specimen is clamped to the aluminum slab through the clamping fixture, as shown in Fig. 7.3. The clamping apparatus is a crucial part of the setup. Afaneh and Ibrahim (1993), Lee and Ibrahim (1993), and Kreider (1995) pointed out the fact that avoiding axial slipping in the clamps is very difficult if not completely unavoidable. This issue, which is closely related to the problem of the stationarity of the experimental conditions, is discussed in more details in Sec. 7.3.

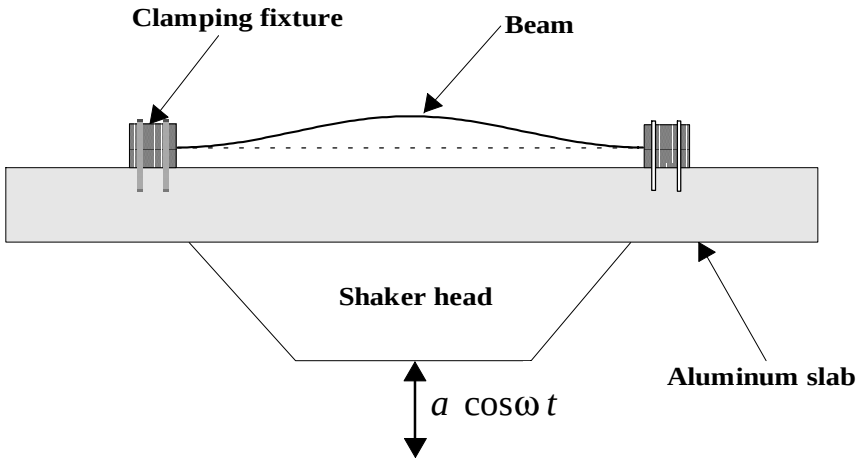

Figure 7.3: Clamping setup and excitation for the buckled beam.

7.1.1 The Excitation

The aluminum slab, which is the base for the specimen, has a thickness of 76.20 *mm*, a length of 508 *mm*, and a width of 381 *mm*. The ratio between the mass of the slab and that of Beam I is approximately 2880. This high ratio has been designed to minimize any feedback to the shaker. However, some feedback is inherent in the shaker–specimen coupled system. Therefore, we monitored the feedback by measuring its amplitude relative to the amplitude of the base acceleration. The base acceleration is assumed to be uniform (see Fig. 7.3). Nevertheless, some rocking–type modes of vibration of the shaker head may be possible either due to imbalances or imperfection in the fixtures of the shaker itself (McConnell, 1995). We tested for any rocking–type modes superimposed on the shaker vertical motion by checking the outputs of the accelerometers at two different locations on the slab, close to the clamps. Differences in amplitude would imply some rocking motion. The spectra of these outputs, with the full noise base, are shown in Fig. 7.4. These data were taken by exciting the first mode of Beam I with an excitation frequency of 164.1 Hz

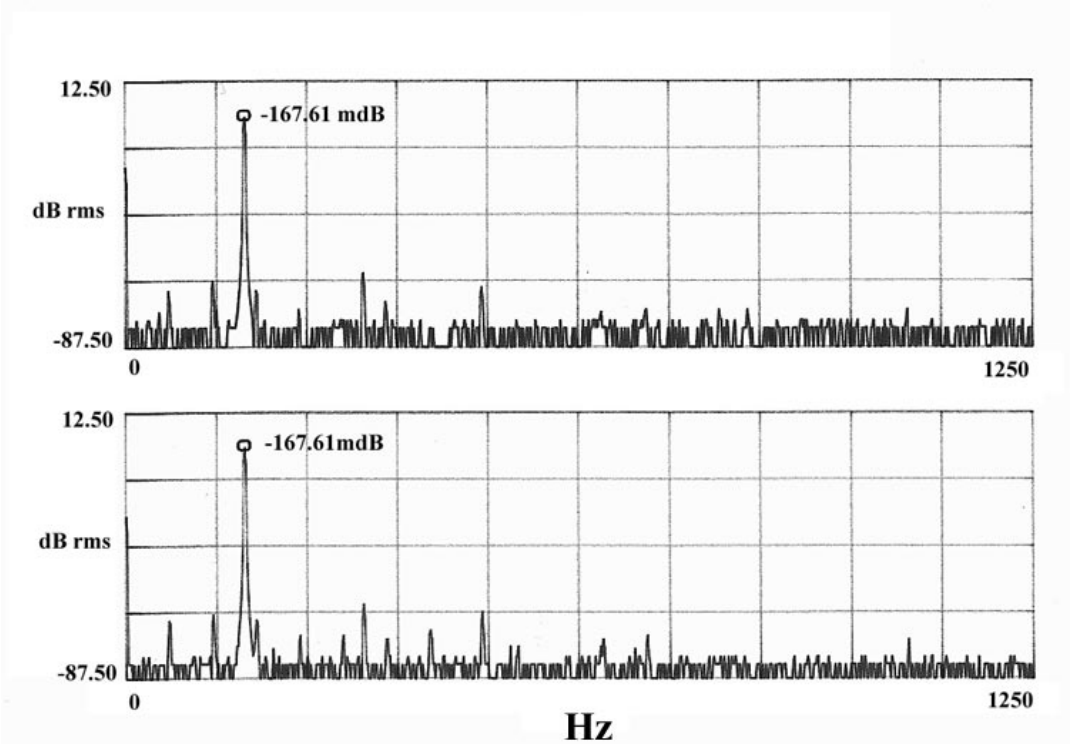

Figure 7.4: Power spectra of the outputs of the accelerometers at two different locations on the clamping platform

and an input voltage of 200 mV. Clearly, the signals are practically identical.

7.2 Measurements

In this section, we discuss the use of a displacement sensor rather than strain–gauges or velocitometers. To obtain frequency–response curves, we need measurements of the displacements. Velocitometers, such as laser vibrometers, could have been used because a conversion from velocities to displacements can be made by using an analog or digital integrator. However, the integration, whether analog or digital, is a further source of error. On the other hand, strain gauges are not suitable at all, because by measuring strains on

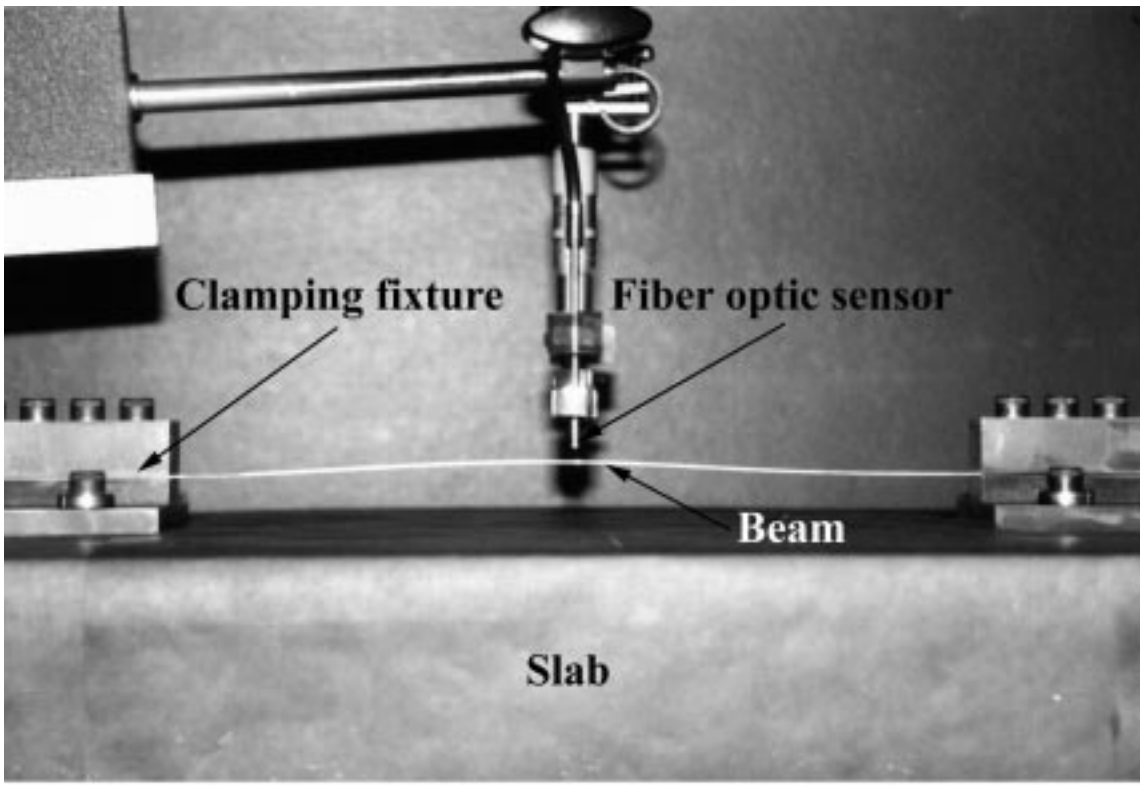

Figure 7.5: Setup for the fiber optic displacement sensor

the outer surface of the beam, we could not relate linearly the strains to the displacements. In fact, because we were exciting geometric nonlinear vibrations of the beam, the strain–displacement relation was not linear during the experiments. We do not know exactly this relation. Using of an approximate relation would introduce an additional source of measurement error.

Next, we discuss the setup of the fiber optic displacement sensor, as shown in Fig. 7.5. There are two key steps in the use of a fiber optic displacement sensor to obtain accurate measurements of motion displacements: the proper choice of the target surface and the calibration procedure. First, accurate measurements depend on precise and consistent

reflection of rays of light from the target surface. To achieve this result requires the target surface to be clean and smooth and the relative orientation of the sensor tip and the target surface to be preserved during the motion. It is also required that the sensor tip be placed perpendicular to the target surface at the beginning of the calibration procedure. We chose the midspan of the beam as the target area to keep the sensor tip perpendicular to the moving target surface (see Fig. 7.5). In fact, first–mode nonlinear responses were excited in primary resonance. Due to symmetry, the originally flat midspan of the beam remained flat during the single–mode symmetric motions.

The calibration process is an important step to convert the output voltage of the amplifier of the sensor to the pertinent units of displacement. Typically, the characteristic curve, shown in Fig. 7.6, having the output voltage as the ordinate and the gap between the sensor and the target as the abscissa, is a nonlinear curve except for a linear range above the optical peak. The factory supplied calibration curves give sensitivity values for near side and a far side linear range slopes.

When the sensor operation falls within the bounds of a near or far side linear range, the readings in peak–to–peak voltage can be converted to peak–to–peak displacement by multiplying the output voltage by the given sensitivity value of units of displacement per units of voltage. This conversion can be applied if the calibration procedure is carefully followed. To have a reliable accuracy in the measurements, we constructed calibration curves for each experimental session by varying the gap between the sensor and the target and reading the corresponding output voltage of the sensor. By using a polynomial fit, we found that the nonlinear range for large gaps is dominated by quadratic nonlinearities. Clearly it is important to check whether, in each experimental run, the peak amplitude of the motion was within the linear range so that use of the conversion factor was justified. Otherwise the fitted nonlinear calibration curve had to be used. However, this was never the case.

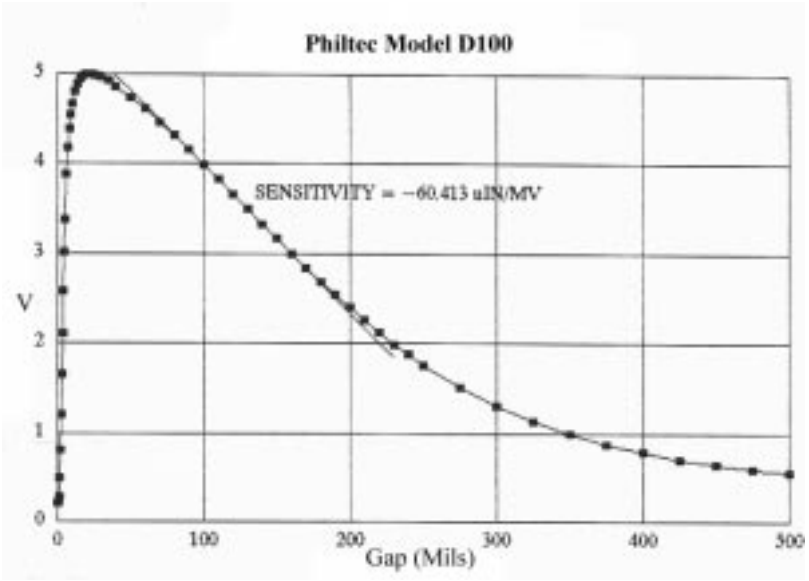

Figure 7.6: Characteristic curve for a Philtec, Series 88, type D fiber optic displacement sensor

7.3 Stationarity of the Experimental Conditions

Kreider (1995) pointed out the critical issue of stationarity of the experimental conditions. He concluded that static slipping occurred, even after designing different versions of the clamps. Furthermore, random temperature fluctuations were such that they could affect significantly the buckling level in the beam and, hence, the natural frequencies.

For each experimental session, the initial imperfection amplitudes could vary. The importance of these effects on the static, linear and nonlinear vibration behavior of the beam has been shown in Chapter 5. However, the natural frequencies proved consistently to be lower after the experimental sessions. Therefore, the slipping was assumed to be the dominant cause. He also concluded that monitoring the power spectrum of the beam free response to a tap proved to be the best and quickest method of measuring the natural frequencies. We also used this method to measure the natural frequencies, because, other

methods, even if more accurate, are more time–consuming.

Experiments aimed at detecting and characterizing chaotic motions in buckled beams were conducted by Nagai (1990) and Nagai and Yamaguchi (1994), Yamaguchi and Nagai (1994). In their experimental setup, they used a room temperature controller (effective within 0.25° Celsius) to buckle the beam thermally and then keep the temperature constant.

We also observed that, in particular days when the temperature dropped at night, the frequencies experienced significant changes on the order of a Hertz. In general, within the time range of an experimental session that can extend up to ten hours, major causes for temperature changes are environmental and fluctuations due to the additional heating produced mainly by the shaker and the rest of the instrumentation. Kreider (1995) mentioned that, even by putting accidentally his hands close to the beam, he could affect appreciably the frequencies of the beam. This circumstance occurred consistently for low buckling levels (see Fig. 5.4).

We observed the same pattern characterized by a consistent drop of the frequencies after each experimental session, confirming the general conclusions drawn by Kreider about the dominance of the slipping effects.

7.4 Experimental Procedure

To obtain experimentally frequency–response curves for a certain buckling level, we swept the excitation frequency around the first natural frequency, and for each frequency we determined the corresponding peak in the power spectrum of the output of the displacement sensor. We calculated the input amplitude by converting the amplitude in the power spectrum of the accelerometer output to the proper units by using the accelerometer calibration

parameter.

Several issues are related to the task of obtaining accurate and reliable frequency–response curves. A frequency–response curve is generated by collecting the peaks of the dynamic response versus a quasistatic variation of the excitation frequency while keeping the amplitude of the input constant. Therefore, the stationarity of the excitation amplitude is a critical factor that is, in turn, connected to the problem of feedback. For Beam I, at high excitation levels, the feedback caused the excitation amplitude to vary slightly in the region of maximum dynamic amplification of the response. For Beam II the measured input was reasonably constant during the excitation frequency sweeps. Beam II is thinner and narrower, and hence it produces inertial forces of lower amplitude and most likely lower feedback.

We controlled the excitation level by observing the power spectrum of the accelerometer output and adjusting the voltage of the input exciter. We suggest a feedback controller for the excitation level to produce fixed–amplitude excitations for future experiments.

The quasistatic character of the frequency sweep is important. It produces stationary rather than nonstationary responses and it prevents any premature jump to other motions, such as chaos, in the multivalued ranges of the frequency–response curve. Moreover, if the frequency is varied very slowly, transition to adjacent motions is quicker because transients die out faster. To achieve this result, we set the frequency sweep step at 0.01 Hz and recorded data every 0.5 Hz, waiting long enough for the transients to die out. The frequency range of the analyzer was set at 20 Hz for all tests. Both channels were set to the averaging mode (stable mean), with the number of averages being equal to three.

It is worth mentioning that, by following meticulously this experimental procedure, it took, on the average, six to ten hours to obtain one frequency–response curve.

We tested both Beams I and II and present the obtained experimental results in the next section.

7.4.1 Experimentally obtained Frequency–Response Curves for Beams I and II

In Fig. 7.8, we show the frequency–response curve obtained in the range 165 Hz to 178 Hz for Beam I. The buckling level was 5.842 mm, the measured first natural frequency before conducting the experiment was 174 Hz, and the base acceleration was set at 0.332 g. For this buckling level and these excitation frequencies, internal resonances were not activated. The discretization approach predicts a hardening behavior, whereas the direct approach predicts a softening behavior, as shown in Fig. 7.7(a). In the forward sweep, the response was initially linear. As the excitation frequency was increased beyond approximately 171.5 Hz, the response jumped up to a nonlinear motion, containing the fundamental frequency and its second and third harmonics, indicating that both quadratic and cubic nonlinearities were activated. The jump up occurred at approximately 171.5 Hz. The arrow indicates the jump direction.

In the reverse sweep, we observed the same motions as those observed in the forward sweep up to 171.5 Hz. Below this frequency, the response underwent a period–doubling bifurcation. The period–doubled motion persisted over a narrow range and then became chaotic. We conjecture that the route to chaos is a period–doubling sequence (Nayfeh and Balachandran, 1995), even though we could not capture experimentally higher–order period–doubling bifurcations. The chaotic response persisted over an extended frequency range. Then, we observed a period-doubled motion. We conjecture the occurrence of a reverse period-doubling sequence. This motion persisted until the response jumped down at approximately 165.6 Hz to a low–amplitude motion. The up and down jumps oc-

curred below the first natural frequency, and hence, the frequency–response curve is of the softening-type.

At the end of the experiment, we found that the first natural frequency was approximately 173.34 Hz. Hence, a shift of 0.66 Hz was experienced by the beam most likely due to slipping effects. However, this does not affect our conclusion about the softening character of the frequency–response curve.

In Fig. 7.9, we show the frequency–response curve obtained for Beam I for the same buckling level, but at the lower excitation amplitude 0.209 g. The measured first natural frequency was 174.27 Hz. The overall characteristics of the motions are similar to those observed at the higher excitation level. However, the jumps occurred at slightly different frequencies: the jump up occurred at approximately 172.70 Hz, and the jump down occurred at 165.25 Hz. This implies that the multivalued range of the frequency–response curve is shifted to the right of that obtained for the higher excitation level.

In Fig. 7.10, we show the frequency–response curve for Beam I for approximately the same buckling level used thus far and a lower excitation level; namely, 0.137 g. The experimentally determined first natural frequency was 174.39 Hz. The jump up occurred at approximately 173.25 Hz, and the jump down occurred at about 170.20 Hz. A distinguished feature of this frequency–response curve, in this case, is the absence of chaotic motion. The low excitation amplitude did not provide enough energy to destabilize the periodic motions and transform them into irregular responses. All three frequency-response curves consistently exhibit a softening character even though they were generated for different excitation amplitudes. These results are in qualitative agreement with those obtained with the direct approach and in disagreement with those obtained with the discretization approach.

Next, we tested Beam II for a buckling level of 3.302 mm, an excitation level of

0.149 g, and the frequency range 96 Hz to 112 Hz. The experimentally obtained first natural frequency before the experiments was 106.06 Hz. Again, no internal resonances were activated. The discretization and direct approaches predict hardening– and softening–type behaviors, respectively, as shown in Fig. 7.11(a). The experimentally obtained frequency–response curve is shown in Fig. 7.12. The jump up occurred at approximately 104.23 Hz, whereas the jump down occurred at about 100.43 Hz. In this case, an interesting phenomenon occurred during the jump up. The large–amplitude motion to which the beam response jumped exhibited a long irregular transient, due to light damping in the beam, that decayed after about an hour, and the motion settled down to a periodic nonlinear response. In the reverse sweep, a chaotic range was also encountered. The transition from periodic to chaotic single–mode motion is not fully clear. Right before the onset of the irregular responses, we observed a period–doubled peak in the power spectrum of the displacement sensor output, but it was not stable, because eventually, after some time, the response spectrum developed into a broadband spectrum. In our opinion, there is not enough evidence and control of the stationarity of the overall experimental conditions to assess whether a subcritical period–doubling occurred. It can be conjectured that the period–doubled motions have a very small range of stability, thus any small perturbation or variation in the system conditions renders this response unstable, leading the response to settle to a more stable attractor, which in this case is a chaotic motion. Following this line of thought, we conjecture that the response encountered a period–doubling route to chaos, where the cascade of period–doublings occurred in a very small range that it could not be observed experimentally, even by decreasing further the frequency step. The experimental nonconclusive statements can be made from the present experimental data. However, the overall behavior of the frequency–response curve is of the softening–type, in qualitative agreement with predictions of the direct approach and in disagreement with predictions of the discretization approach.

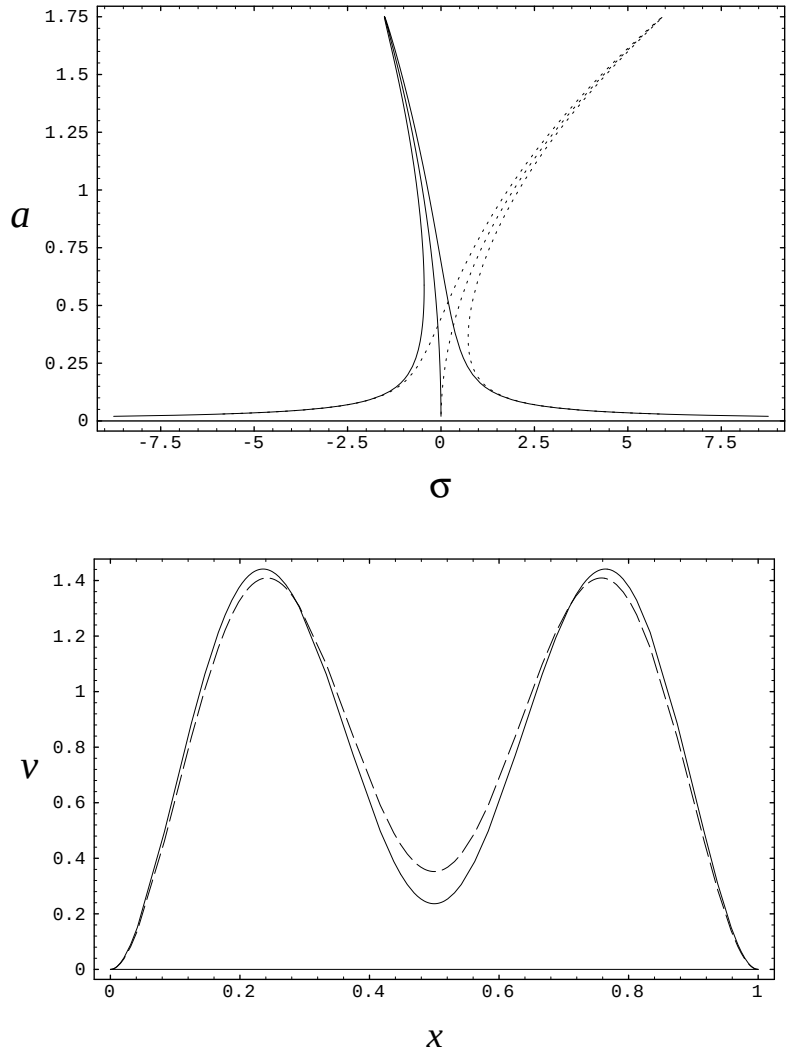

Figure 7.7: Theoretically obtained results for the case of primary resonance of the first mode for Beam I when $\hat{b} = 5.842\ mm$, $f = 25$, and $\mu = 0.1$: (a) frequency–response curve and (b) nonlinear response. Solid and dashed lines indicate results obtained with the direct and discretization approaches, respectively.

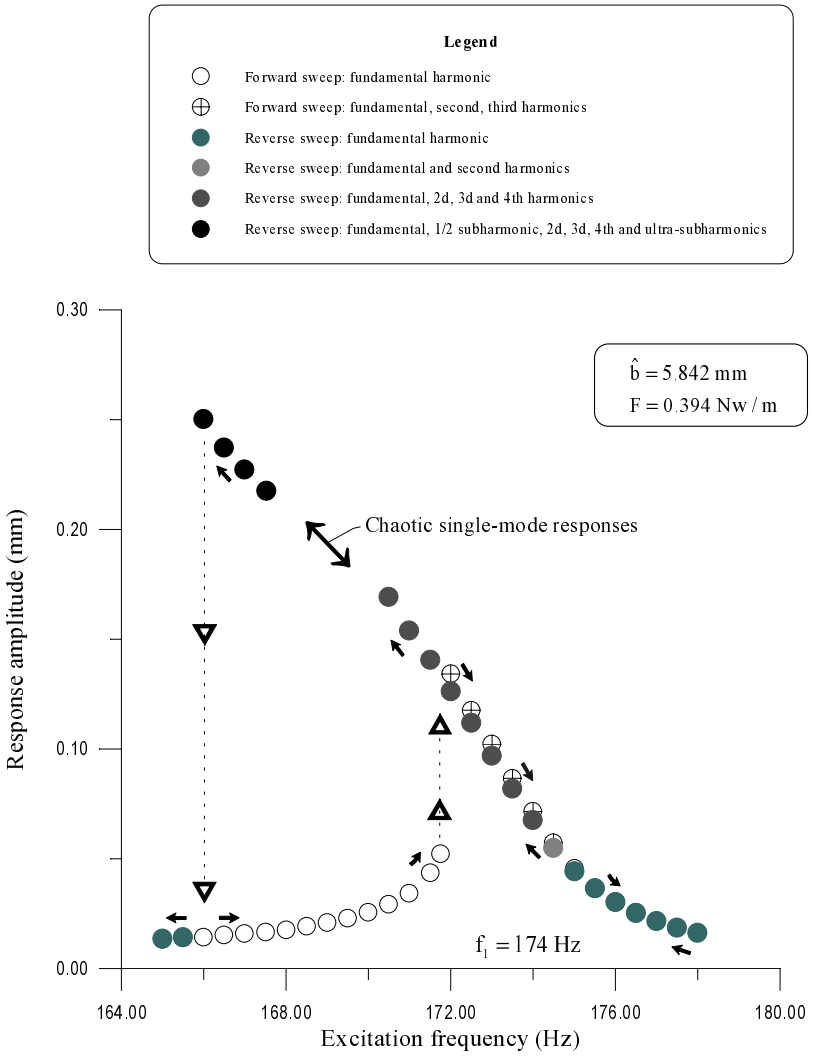

Figure 7.8: Experimentally obtained frequency-response curve for Beam I when $\hat{b}$ is 5.842 *mm* and the excitation amplitude is 0.332 *g*.

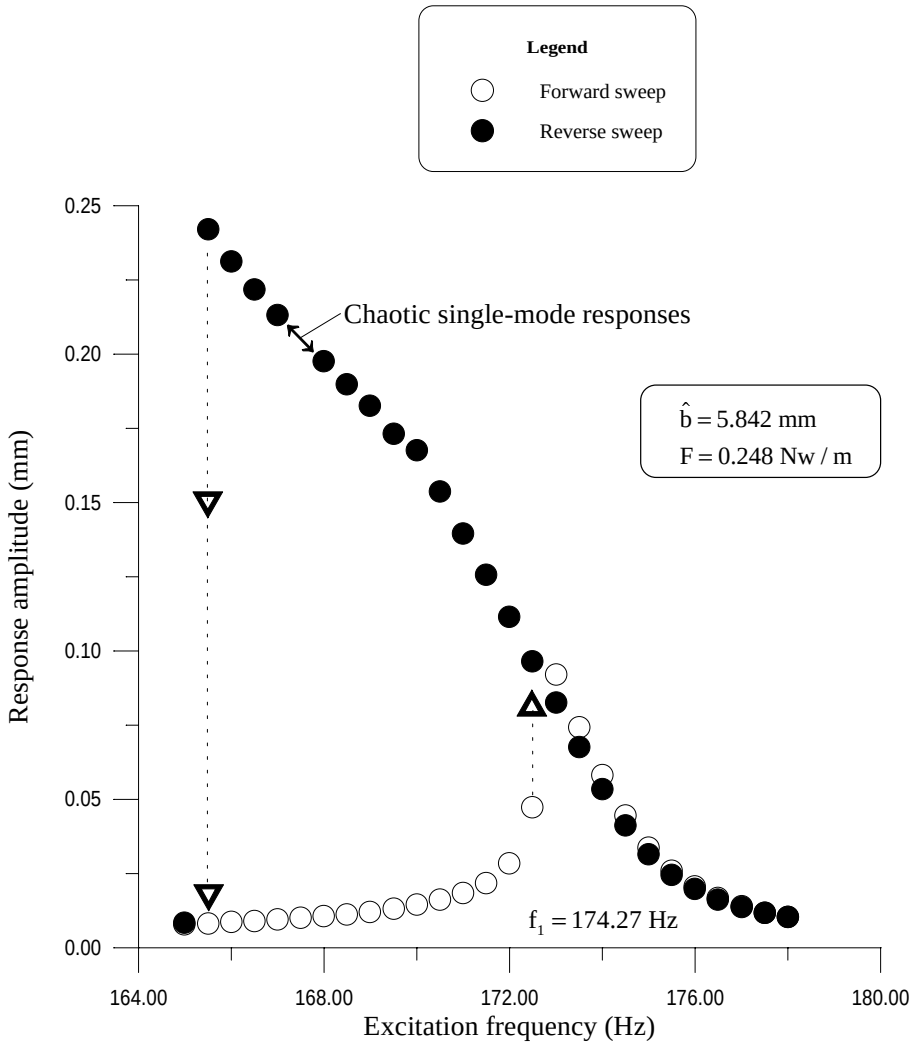

Figure 7.9: Experimentally obtained frequency–response curve for Beam I when $\hat{b}$ is 5.842 *mm* and the excitation amplitude is 0.209 *g*.

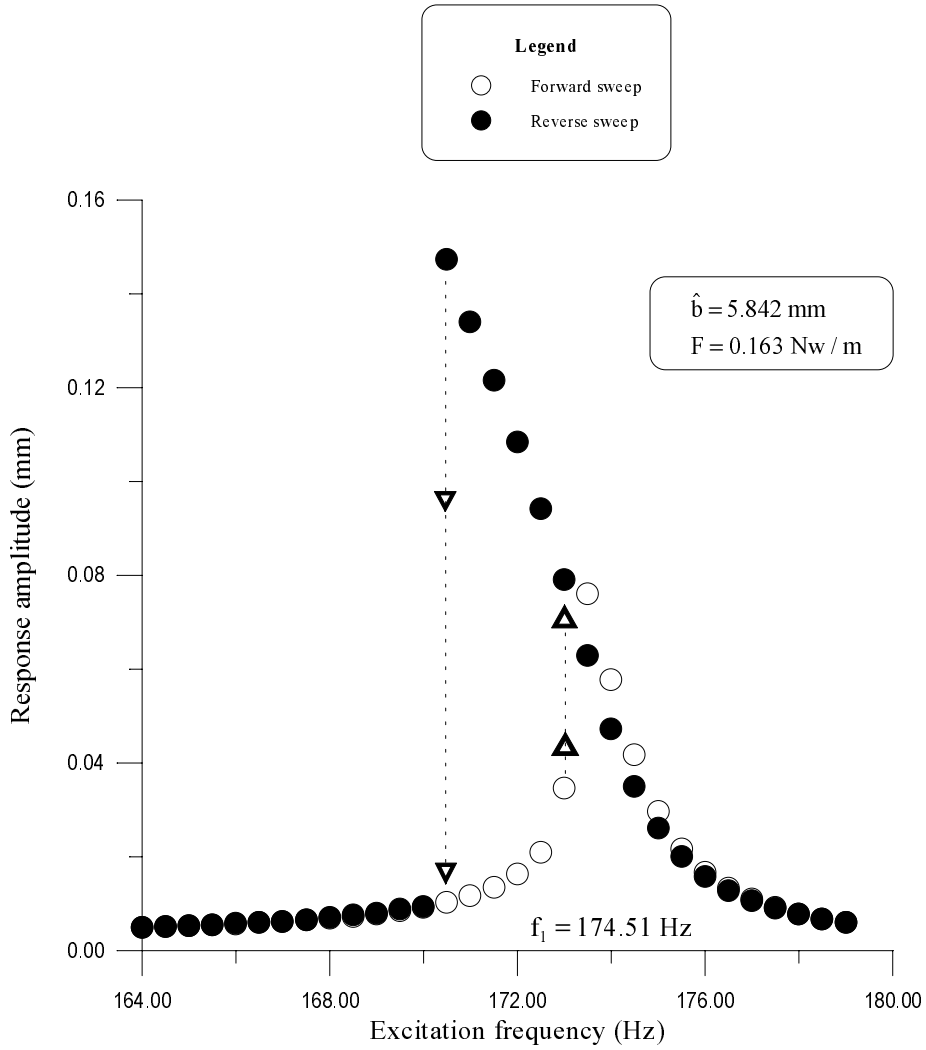

Figure 7.10: Experimentally obtained frequency–response curve for Beam I when $\hat{b}$ is 5.842 *mm* and the excitation amplitude is 0.137 *g*.

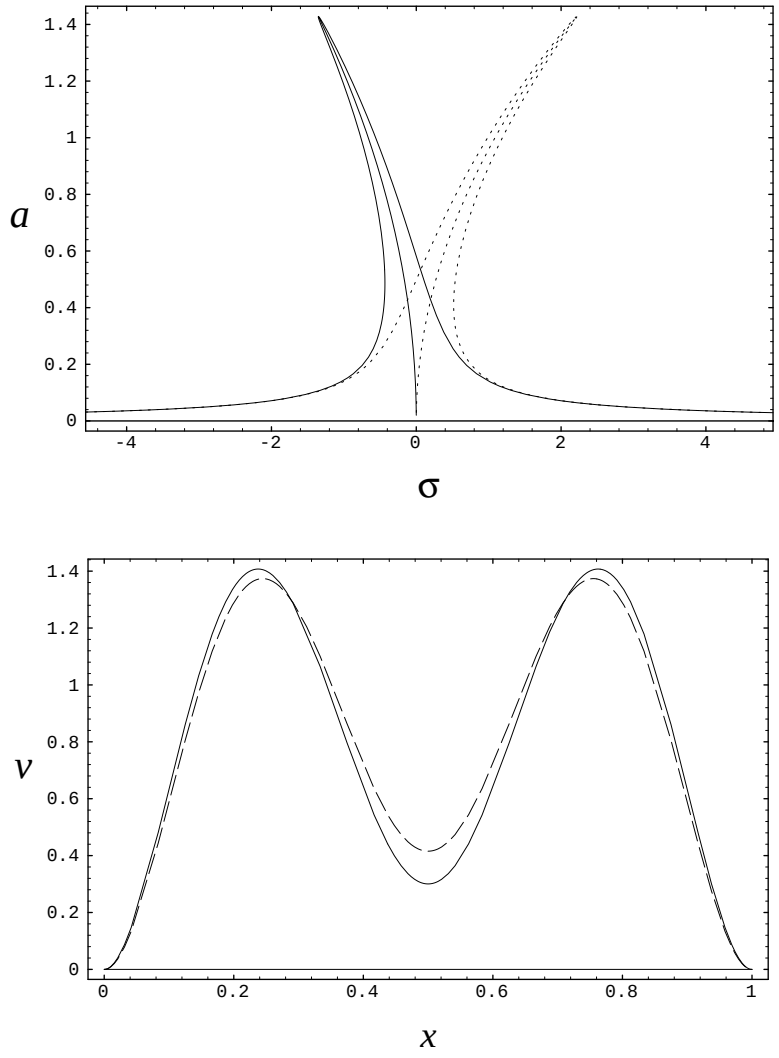

Figure 7.11: Theoretically obtained results for the case of primary resonance of the first mode for Beam II when $\hat{b} = 3.302\ mm$, $f = 20$, and $\mu = 0.1$: (a) frequency–response curve and (b) nonlinear response. Solid and dashed lines indicate results obtained with the direct and discretization approaches, respectively.

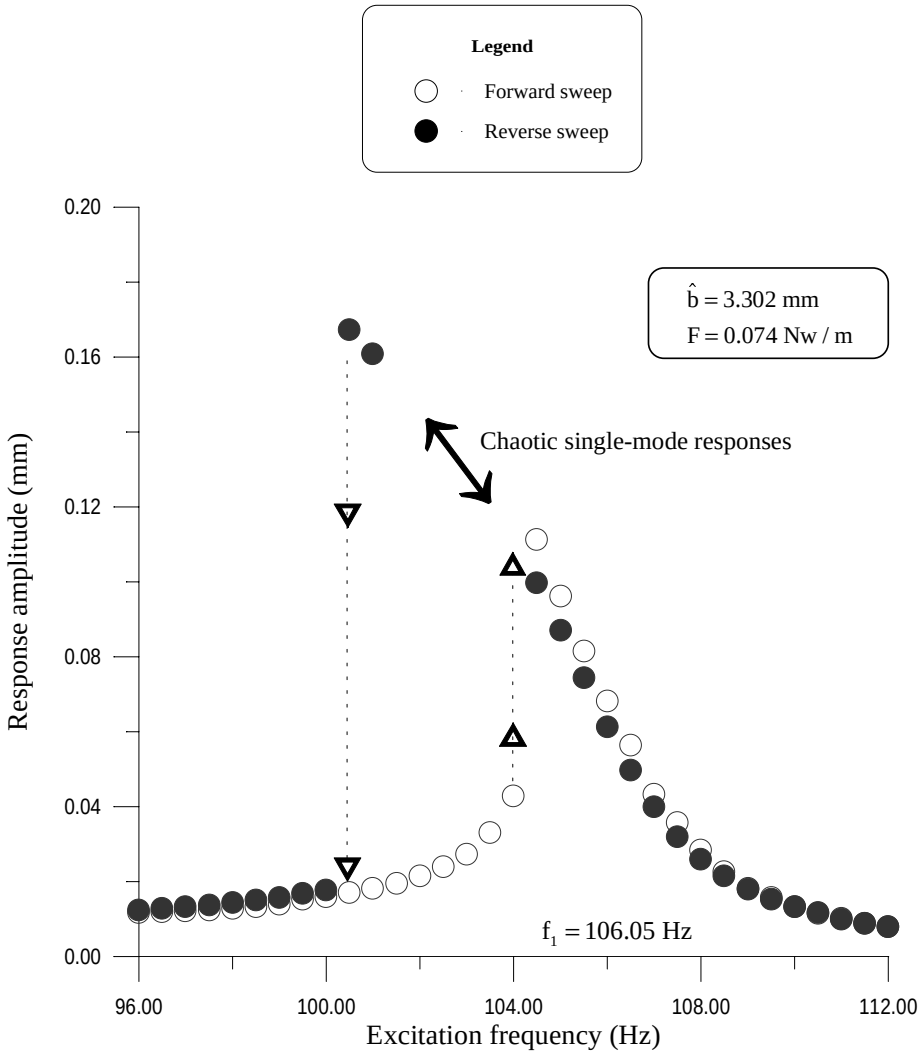

Figure 7.12: Experimentally obtained frequency–response curve for Beam II when $\hat{b}$ is 3.302 mm and the excitation amplitude is 0.149 g.

Chapter 8

Nonlinear Multimodal Interactions

In this chapter, asymptotic expansions of the responses for the cases of three–to–one, one–to–one and simultaneous resonances are presented. The motivation for these results comes from the repeated experimental observation of three–to–one and simultaneous resonances. We present some of the experimental power spectra corresponding to these resonances. The boundary–value problems related to the direct perturbation procedure are thoroughly discussed in terms of their mathematical and numerical implications.

8.1 Internal Resonances

A few internal resonances can be activated in buckled beams. By inspection of Fig. 6.1, we note that a two–to–one internal resonance between the first and second modes may be activated when $b = b_1 \approx 2.860$; this case was treated analytically by Kreider, Chin, and Nayfeh (1995). One–to–one internal resonances between the first and second modes and between the third and fourth modes may be activated when b is near $b_2 \approx 6.210$ and

Table 8.1: Internal Resonances

Type	*Resonance Conditions*	b
1:1	$\omega_1 = \omega_2$	6.210
1:1	$\omega_3 = \omega_4$	15.784
2:1	$2\omega_1 = \omega_2$	2.860
3:1	$\omega_3 = 3\omega_2$	9.216
3:1	$\omega_3 = 3\omega_1$	20.153
Simultaneous	$\omega_4 \approx 4\omega_2$ and $\omega_3 \approx \omega_2 + \omega_4$	23.312

$b_4 \approx 15.784$, respectively. Three–to–one internal resonances between the third and second modes and between the third and first modes may be activated when b is near $b_3 \approx 9.216$ and $b_5 \approx 20.153$, respectively. Also, the second, fourth, and fifth modes may be activated simultaneously when $b = 23.312$ and the excitation frequency, Ω, is approximately twice the frequency of the second mode. At this buckling level, $\omega_4 \approx 4\omega_2$ and $\omega_3 \approx \omega_2 + \omega_4$. Consequently, there are three possible simultaneous resonances: a subharmonic resonance of order one–half of the first antisymmetric mode, a superharmonic resonance of order two of the second antisymmetric mode, and a subcombination resonance involving the second and third modes.

In the following sections, we consider three–to–one, one–to–one, and simultaneous resonances when one of the interacting modes is excited by a primary or a subharmonic resonance of order one–half. The results of the analytical and numerical analyses show that the three–to–one resonance at $b = b_4$ between the first antisymmetric and second symmetric modes cannot be activated. These modes are not coupled in the nonlinear sense. In fact, we could never activate this resonance in the experiments.

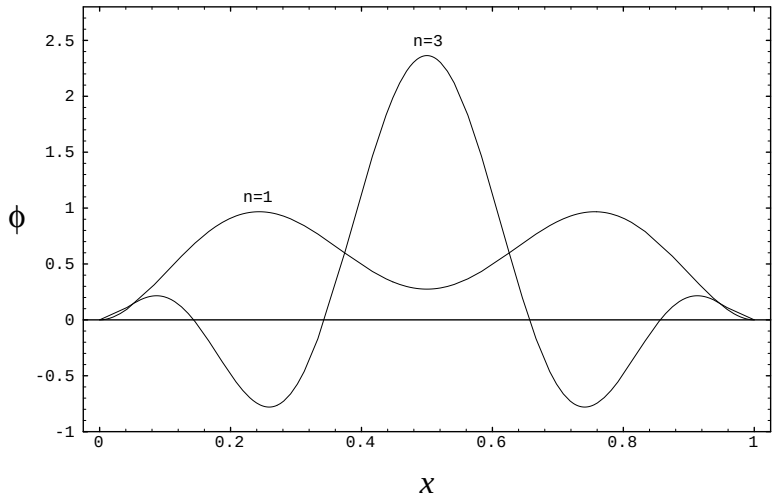

Figure 8.1: The first and third mode shapes when $b = b_5$.

8.2 Three–to–One Internal Resonance

In this section, we determine a second–order uniform expansion for the solutions of Eqs. (6.2) and (6.3) when b is near either b_3 or b_5. In Fig. 8.1, we show the first and third mode shapes when $b = b_5$. In Fig. 8.2, we show the power spectra of the response and the excitation when the excitation frequency and amplitude are, respectively, 168.75 Hz and 0.045 g. Clearly, a three–to–one internal resonance between the first and third modes is activated when the first mode is directly excited with a primary resonance. In Fig. 8.3, we show the power spectra of the response and excitation when the excitation frequency and amplitude are, respectively, 167.97 Hz and 0.065 g. We note the side-band structure in the response. The beam seems to have undergone a Hopf bifurcation and the response seems to be quasiperiodic (Nayfeh and Balachandran, 1995).

We use the method of multiple scales to attack directly the integro–partial–differential system because discretization would lead to erroneous results as shown for the case of

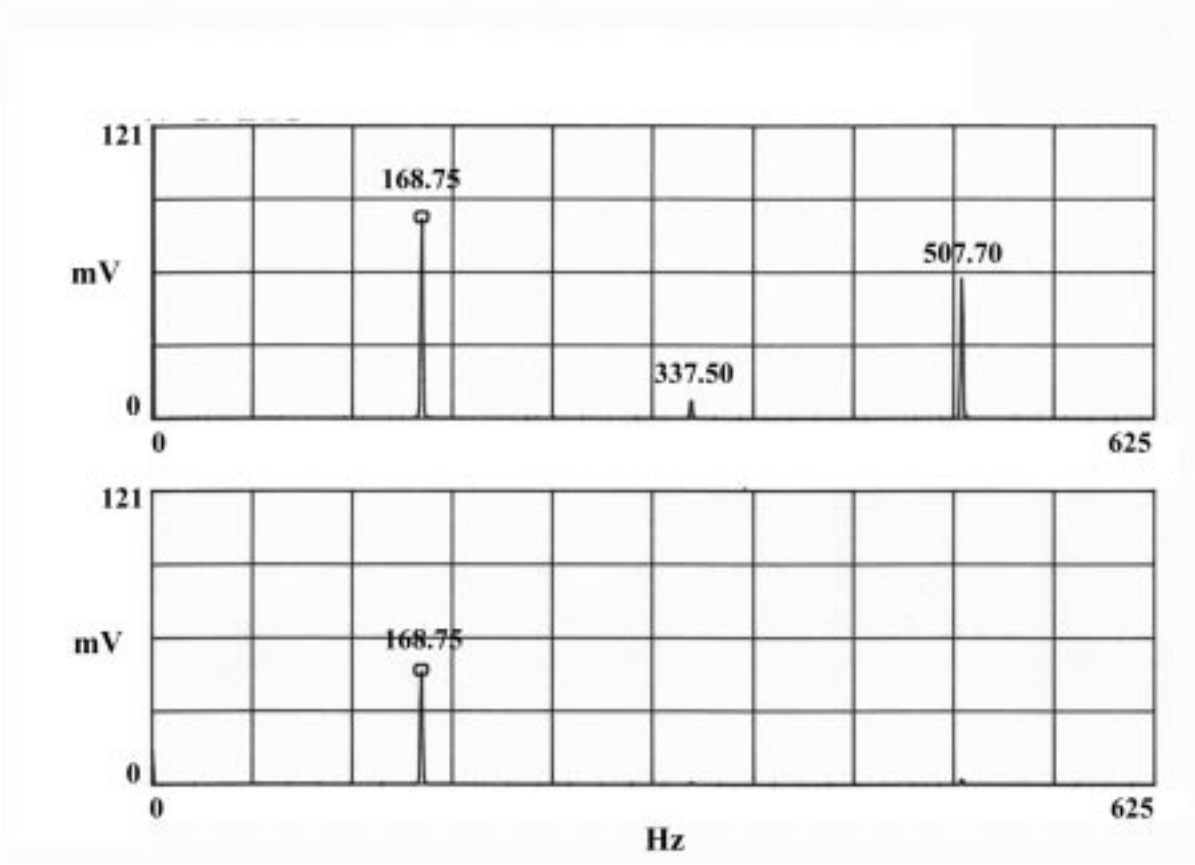

Figure 8.2: Power spectra of the response and excitation for the case of three–to–one internal resonance for Beam I when the excitation frequency and amplitude are, respectively, 168.75 Hz and 0.045 g.

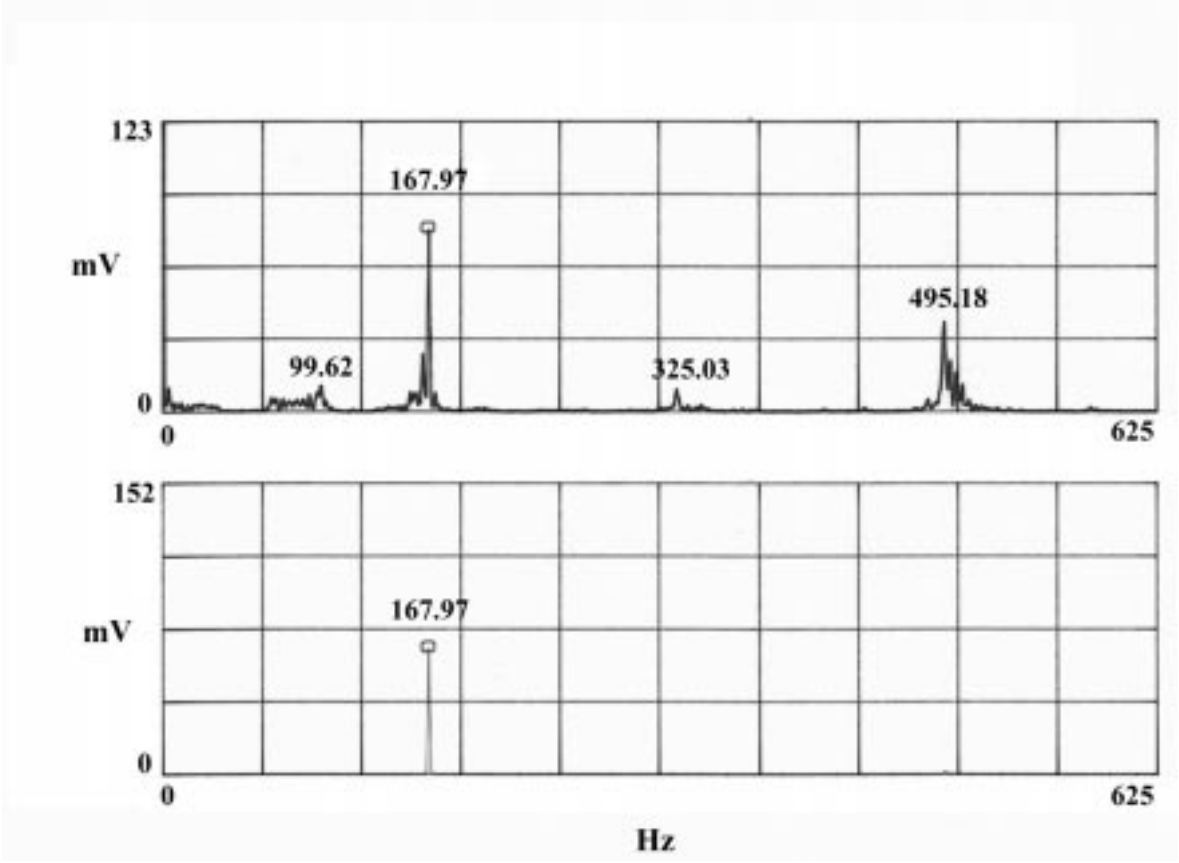

Figure 8.3: Power spectra of the response and excitation for the case of three–to–one internal resonance for Beam I when the excitation frequency and amplitude are, respectively, 167.97 Hz and 0.065 g.

single–mode responses. Thus, we seek a second–order uniform expansion in the form of Eq. (6.28). We note that $v(x,t)$ does not depend on T_1 because secular term arise at $O(\epsilon^3)$. Because in the presence of damping all modes that are not directly or indirectly excited decay with time, the solution of the first–order problem, Eqs. (6.29) and (6.32), is assumed to consist of the two interacting modes; that is,

$$v_1 = A_n(T_2)\phi_n(x)e^{i\omega_n T_0} + A_m(T_2)\phi_m(x)e^{i\omega_m T_0} + cc \tag{8.1}$$

where the complex–valued functions A_n and A_m are determined by imposing the solvability conditions at third order, and the subscripts m and n indicate the two modes involved in the internal resonance.

Substituting Eq. (8.1) into Eq. (6.30) yields

$$\begin{aligned}\mathcal{L}(v_2) = {} & h_{1n}(x)A_n^2 e^{2i\omega_n T_0} + h_{1m}(x)A_m^2 e^{2i\omega_m T_0} + h_{nm}(x)\Big[A_n A_m e^{i(\omega_n+\omega_m)T_0} \\ & + A_n\bar{A}_m e^{i(\omega_n-\omega_m)T_0}\Big] + h_{1n}(x)A_n\bar{A}_n + h_{1m}(x)A_m\bar{A}_m + cc\end{aligned} \tag{8.2}$$

where

$$h_{1i} = b\pi\phi_i''\int_0^1 \phi_i' \sin 2\pi x dx + b\pi^2 \cos 2\pi x \int_0^1 \phi_i'^2 dx \tag{8.3}$$

$$\begin{aligned}h_{nm} = {} & b\pi\Big[\phi_n''\int_0^1 \phi_m' \sin 2\pi x dx + \phi_m''\int_0^1 \phi_n' \sin 2\pi x dx \\ & + 2\pi\cos 2\pi x \int_0^1 \phi_n'\phi_m' dx\Big]\end{aligned} \tag{8.4}$$

A particular solution of Eqs. (8.2) and (6.32) can be expressed as

$$\begin{aligned}v_2 = {} & \Gamma_{1n}(x)A_n^2 e^{2i\omega_n T_0} + \Gamma_{1m}(x)A_m^2 e^{2i\omega_m T_0} + \Gamma_3(x)A_n A_m e^{i(\omega_n+\omega_m)T_0} \\ & + \Gamma_4(x)A_n\bar{A}_m e^{i(\omega_n-\omega_m)T_0} + \Gamma_{2n}(x)A_n\bar{A}_n + \Gamma_{2m}(x)A_m\bar{A}_m + cc\end{aligned} \tag{8.5}$$

where the Γ_{ij} are given by

$$M(\Gamma_{1i}; 2\omega_i) = h_{1i}(x) \tag{8.6}$$

$$M(\Gamma_3;\omega_n+\omega_m)=h_{nm}(x) \tag{8.7}$$

$$M(\Gamma_4;\omega_n-\omega_m)=h_{nm}(x) \tag{8.8}$$

$$M(\Gamma_{2i};0)=h_{1i}(x) \tag{8.9}$$

the operator $M(\Gamma;\omega)$ is defined by Eq. (6.38), and the boundary conditions on the Γ's are given by Eq. (6.37). We solved the six fourth-order integro-differential boundary-value problems, Eqs. (8.6)–(8.9) and (6.37), by using the method of undetermined coefficients and obtained closed-form solutions for the Γ_{ij}. In Fig. 8.4, we show the functions Γ_{ij} for the case of a three–to–one internal resonance between the first and third modes when $b=b_5$. In Figs. 8.5 and 8.6, we show the functions Γ_{ij} for the cases of one–to–one internal resonance between the first and second modes when $b=b_2$ and between the third and fourth modes when $b=b_4$, respectively.

Substituting Eqs. (8.1) and (8.5) into Eq. (6.31) and considering the case $\omega_n\approx 3\omega_m$ and $\Omega\approx\omega_n$ or ω_m, we obtain

$$\begin{aligned}\mathcal{L}(v_3)=&-\left[2i\omega_n\left(A_n'+\mu A_n\right)\phi_n-\chi_{1n}A_n^2\bar{A}_n-\chi_{nm}A_nA_m\bar{A}_m\right]e^{i\omega_nT_0}\\&-\left[2i\omega_m\left(A_m'+\mu A_m\right)\phi_m-\chi_{1m}A_m^2\bar{A}_m-\chi_{mn}A_mA_n\bar{A}_n\right]e^{i\omega_mT_0}\\&+\chi_5A_m^3e^{3i\omega_mT_0}+\chi_6A_n\bar{A}_m^2e^{i(\omega_n-2\omega_m)T_0}+\frac{1}{2}Fe^{i\Omega T_0}+cc+NST\end{aligned} \tag{8.10}$$

where

$$\begin{aligned}\chi_{1i}=&\,b\pi\left[(\Gamma_{1i}''+2\Gamma_{2i}'')\int_0^1\phi_i'\sin 2\pi x dx+\phi_i''\int_0^1(\Gamma_{1i}'+2\Gamma_{2i}')\sin 2\pi x dx\right]\\&+2b\pi^2\cos 2\pi x\int_0^1(\Gamma_{1i}'+2\Gamma_{2i}')\phi_i' dx+\frac{3}{2}\phi_i''\int_0^1\phi_i'^2dx\end{aligned} \tag{8.11}$$

$$\begin{aligned}\chi_{ij}=&+b\pi\left[2\Gamma_{2j}''\int_0^1\phi_i'\sin 2\pi x dx+(\Gamma_3''+\Gamma_4'')\int_0^1\phi_j'\sin 2\pi x dx\right]\\&+b\pi\left[2\phi_i''\int_0^1\Gamma_{2j}'\sin 2\pi x dx+\phi_j''\int_0^1(\Gamma_3'+\Gamma_4')\sin 2\pi x dx\right]\\&+2b\pi^2\cos 2\pi x\int_0^1\left[2\phi_i'\Gamma_{2j}'+\phi_j'(\Gamma_3'+\Gamma_4')\right]dx\\&+\phi_i''\int_0^1\phi_j'^2dx+2\phi_j''\int_0^1\phi_i'\phi_j'dx\end{aligned} \tag{8.12}$$

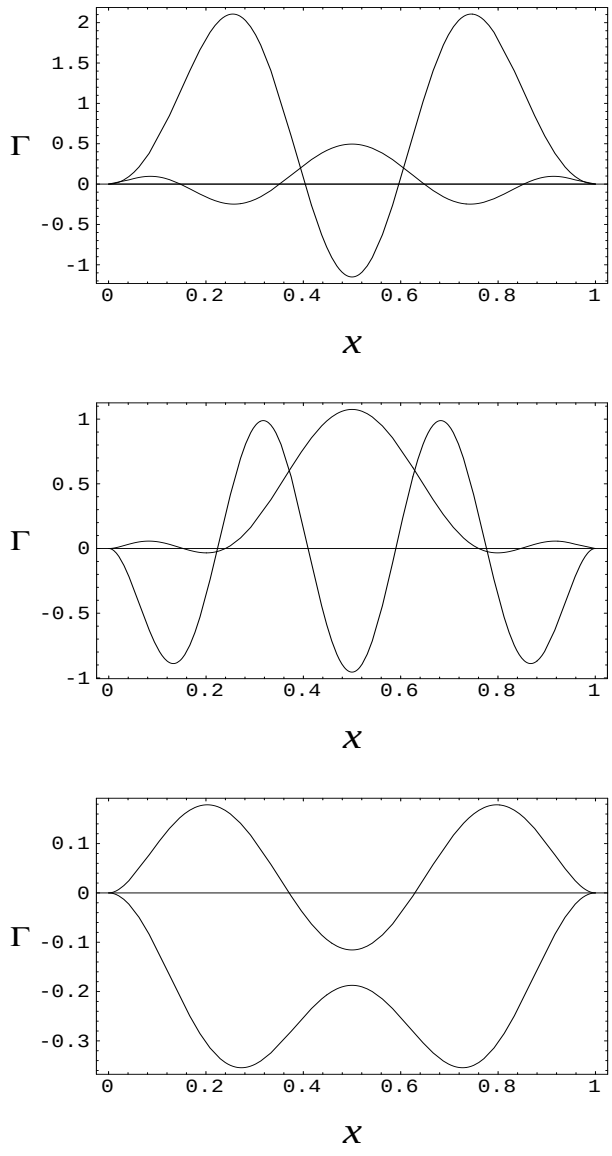

Figure 8.4: The functions Γ_{ij} for the case of three-to-one internal resonance between the first and third modes when $b = b_5$.

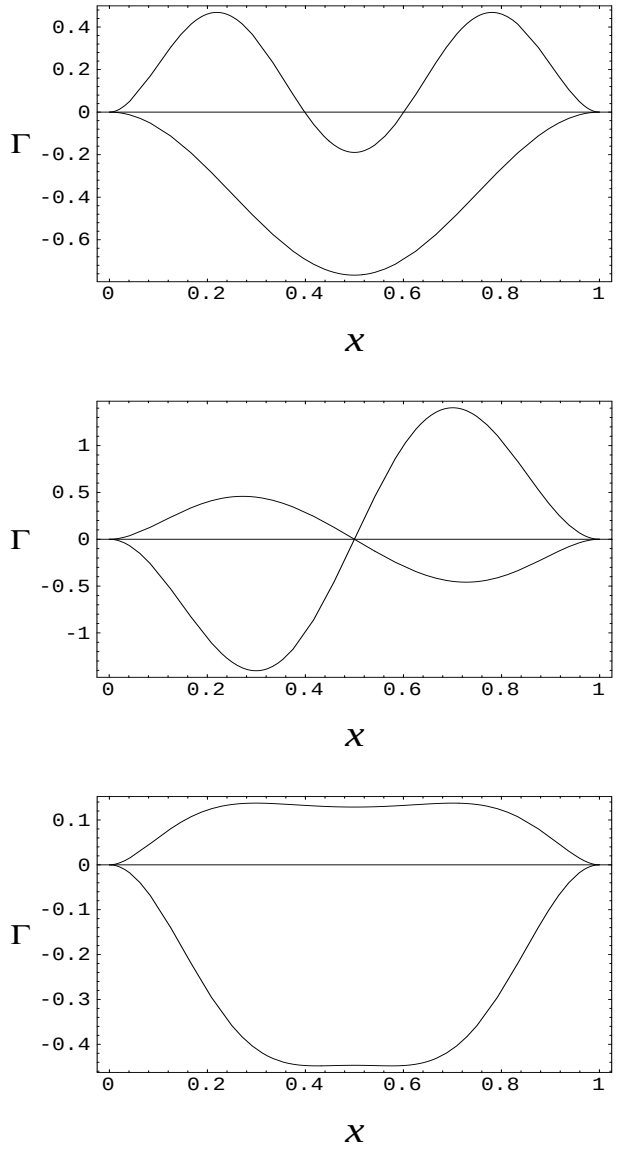

Figure 8.5: The functions Γ_{ij} for the case of one-to-one internal resonance between the first and second modes when $b = b_2$.

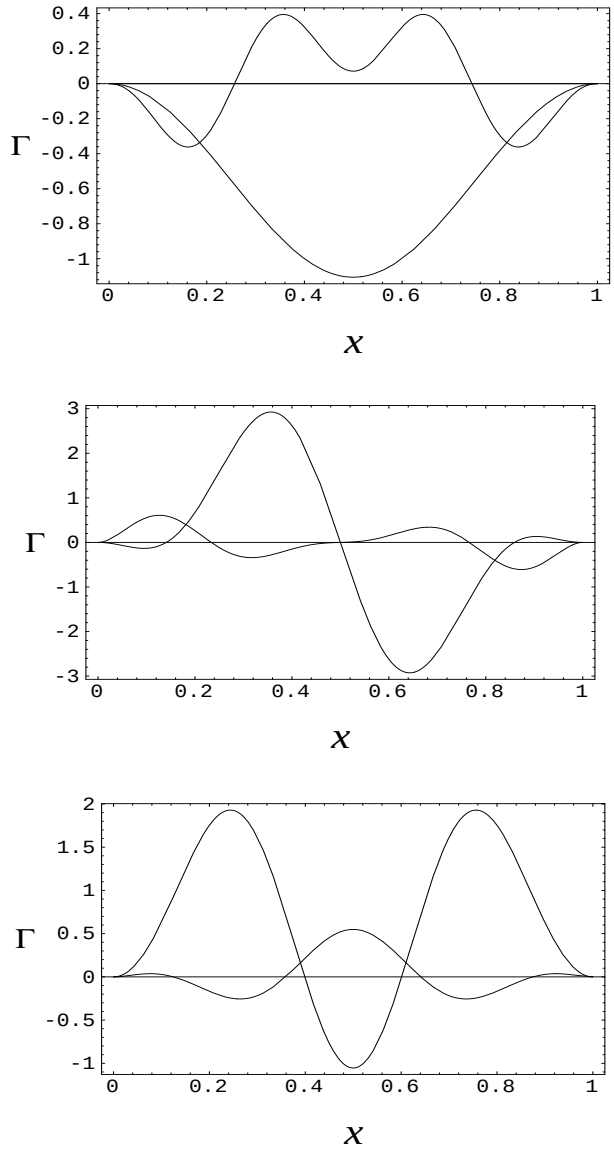

Figure 8.6: The functions Γ_{ij} for the case of one-to-one internal resonance between the third and fourth modes when $b = b_4$.

$$\chi_5 = +b\pi\left[\Gamma''_{1m}\int_0^1 \phi'_m \sin 2\pi x dx + \phi''_m \int_0^1 \Gamma'_{1m}\sin 2\pi x dx\right] +2b\pi^2\cos 2\pi x \int_0^1 \phi'_m\Gamma'_{1m}dx + \frac{1}{2}\phi''_m\int_0^1 \phi'^2_m dx \tag{8.13}$$

$$\begin{aligned}\chi_6 = &+b\pi\left[\Gamma''_{1m}\int_0^1 \phi'_n \sin 2\pi x dx + \phi''_n \int_0^1 \Gamma'_{1m}\sin 2\pi x dx\right.\\ &\left.+\Gamma''_4\int_0^1 \phi'_m \sin 2\pi x dx + \phi''_m\int_0^1 \Gamma'_4 \sin 2\pi x dx\right]\\ &+2b\pi^2\cos 2\pi x\int_0^1 \left(\phi'_n\Gamma'_{1m}+\Gamma'_4\phi'_m\right)dx\\ &+\phi''_m\int_0^1 \phi'_n\phi'_m dx + \frac{1}{2}\phi''_n\int_0^1 \phi'^2_m dx\end{aligned} \tag{8.14}$$

To describe the nearness of ω_n to $3\omega_m$ and Ω to either ω_n or ω_m, we introduce the detuning parameters σ_1 and σ_2 defined by

$$\omega_n = 3\omega_m + \epsilon^2\sigma_1 \ \text{ and } \ \Omega = \omega_i + \epsilon^2\sigma_2 \tag{8.15}$$

Because the homogeneous problem governing v_3 has a nontrivial solution, the corresponding nonhomogeneous problem has a solution only if the right–hand side of Eq. (8.10) is orthogonal to every solution of the adjoint homogeneous problem governing v_3. Since this problem is self–adjoint, the adjoints are given by $\phi_j(x)\exp(\pm i\omega_j T_0)$. Demanding that the right–hand side of Eq. (8.10) be orthogonal to $\phi_n(x)\exp(-i\omega_n T_0)$ and $\phi_m(x)\exp(-i\omega_m T_0)$ and using Eq. (8.15), we obtain the solvability conditions

$$\begin{aligned}2i\omega_n\left(A'_n+\mu A_n\right) = &\,8S_{nn}A_n^2\bar{A}_n + 8S_{nm}A_nA_m\bar{A}_m + 8\Lambda_n A_m^3 e^{-i\sigma_1 T_2}\\ &-\frac{1}{2}f_n\delta_{in}e^{i\sigma_2 T_2}\end{aligned} \tag{8.16}$$

$$\begin{aligned}2i\omega_m\left(A'_m+\mu A_m\right) = &\,8S_{mm}A_m^2\bar{A}_m + 8S_{mn}A_mA_n\bar{A}_n + 8\Lambda_m A_n\bar{A}_m^2 e^{i\sigma_1 T_2}\\ &-\frac{1}{2}f_m\delta_{im}e^{i\sigma_2 T_2}\end{aligned} \tag{8.17}$$

where

$$f_i = \int_0^1 F(x)\phi_i(x)dx \tag{8.18}$$

$$8S_{ii} = \int_0^1 \chi_{1i}\phi_i dx, \;\; 8S_{ij} = \int_0^1 \chi_{ij}\phi_i dx \;\; \text{for} \;\; i \neq j \tag{8.19}$$

$$8\Lambda_n = \int_0^1 \chi_5 \phi_n dx \;\; \text{and} \;\; 8\Lambda_m = \int_0^1 \chi_6 \phi_m dx \tag{8.20}$$

We note that, except for the damping terms, the system is conservative and hence Eqs. (8.16) and (8.17) must be derivable from the Lagrangian

$$\begin{aligned}\mathcal{L} = {} & i\omega_n \left(A_n \bar{A}_n' - \bar{A}_n A_n'\right) + i\omega_m \left(A_m \bar{A}_m' - \bar{A}_m A_m'\right) \\ & + 4S_{nn} A_n^2 \bar{A}_n^2 + 4S_{mm} A_m^2 \bar{A}_m^2 + 8S_{mn} A_n \bar{A}_n A_m \bar{A}_m \\ & + \left[8\Lambda_n A_n \bar{A}_m^3 e^{i\sigma_1 T_2} - \frac{1}{2} f_n \delta_{in} \bar{A}_n e^{i\sigma_2 T_2} - \frac{1}{2} f_m \delta_{im} \bar{A}_m e^{i\sigma_2 T_2} + cc\right]\end{aligned} \tag{8.21}$$

Consequently,

$$S_{mn} = S_{nm} \;\; \text{and} \;\; \Lambda_m = 3\Lambda_n \tag{8.22}$$

Next, separating real and imaginary parts in Eqs. (8.16) and (8.17), we obtain the real–valued modulation equations

$$a_n' = -\mu a_n - \frac{\Lambda_n}{\omega_n} a_m^3 \sin\gamma_1 - \frac{1}{2}\frac{f_n}{\omega_n}\delta_{in}\sin\gamma_2 \tag{8.23}$$

$$\begin{aligned} a_n \beta_n' = {} & -\frac{S_{nn}}{\omega_n} a_n^3 - \frac{S_{nm}}{\omega_n} a_n a_m^2 - \frac{\Lambda_n}{\omega_n} a_m^3 \cos\gamma_1 \\ & + \frac{1}{2}\frac{f_n}{\omega_n}\delta_{in}\cos\gamma_2 \end{aligned} \tag{8.24}$$

$$a_m' = -\mu a_m + \frac{\Lambda_m}{\omega_m} a_n a_m^2 \sin\gamma_1 - \frac{1}{2}\frac{f_m}{\omega_m}\delta_{im}\sin\gamma_2 \tag{8.25}$$

$$\begin{aligned} a_m \beta_m' = {} & -\frac{S_{mm}}{\omega_m} a_m^3 - \frac{S_{mn}}{\omega_m} a_m a_n^2 - \frac{\Lambda_m}{\omega_m} a_n a_m^2 \cos\gamma_1 \\ & + \frac{1}{2}\frac{f_m}{\omega_m}\delta_{im}\cos\gamma_2 \end{aligned} \tag{8.26}$$

where

$$\sigma_1 T_2 - 3\beta_m + \beta_n = \gamma_1$$

$$\sigma_2 T_2 - \delta_{in}\beta_n - \delta_{im}\beta_m = \gamma_2$$

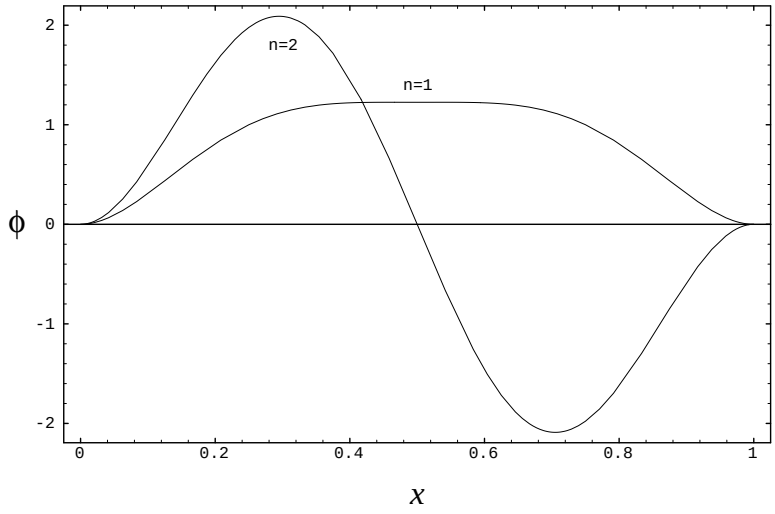

Figure 8.7: The first and second mode shapes when $b = b_1$.

8.3 One–to–One Internal Resonance

In this section, we determine a second–order uniform expansion for the solutions of Eqs. (6.2) and (6.3) when b is near b_2 or b_4. In Fig. 8.7, we show the first and second mode shapes when $b = b_1$. We note that the analysis of the three–to–one internal resonance up to Eqs. (8.9) holds for the present case. However, instead of Eq. (8.10), we have

$$\begin{aligned}\mathcal{L}(v_3) = &-\left[i\omega_n\left(2A_n' + cA_n\right)\phi_n - \chi_{1n}A_n^2\bar{A}_n - \chi_{nm}A_nA_m\bar{A}_m\right]e^{i\omega_nT_0}\\ &-\left[i\omega_m\left(2A_m' + cA_m\right)\phi_m - \chi_{1m}A_m^2\bar{A}_m - \chi_{mn}A_mA_n\bar{A}_n\right]e^{i\omega_mT_0}\\ &+\chi_6A_m^2\bar{A}_ne^{i(2\omega_m-\omega_n)T_0} + \chi_7A_n^2\bar{A}_me^{i(2\omega_n-\omega_m)T_0}\\ &+\frac{1}{2}Fe^{i\Omega T_0} + cc + NST\end{aligned} \tag{8.27}$$

where the χ_{1i}, χ_{ij}, and χ_6 are defined in Eqs. (8.11), (8.12), and (8.14) and χ_7 can be obtained from Eq. (8.12) by interchanging the indices m and n. To describe the nearness of ω_n to ω_m and Ω to ω_n, we introduce the detuning parameters σ_1 and σ_2 defined as

$$\omega_n = \omega_m + \epsilon^2\sigma_1 \ \text{ and } \ \Omega = \omega_n + \epsilon^2\sigma_2 \tag{8.28}$$

Demanding that the right–hand side of Eq. (8.27) be orthogonal to $\phi_n(x)\exp(-i\omega_n T_0)$ and $\phi_m(x)\exp(-i\omega_m T_0)$ and using Eqs. (8.28), we obtain

$$\begin{aligned}2i\omega_n(A_n' +\mu A_n) &= 8S_{nn}A_n^2\bar{A}_n^2 + 8S_{nm}A_nA_m\bar{A}_m + 8R_1A_m^2\bar{A}_me^{i\sigma_1T_2}\\ &+8R_2A_mA_n\bar{A}_ne^{-i\sigma_1T_2} + 8R_3A_m^2\bar{A}_ne^{-2i\sigma_1T_2} + 8R_4A_n^2\bar{A}_ne^{i\sigma_1T_2}\\ &-\frac{1}{2}f_ne^{i\sigma_2T_2}\end{aligned} \tag{8.29}$$

$$\begin{aligned}2i\omega_m(A_m' +\mu A_m) &= 8S_{mm}A_m^2\bar{A}_m + 8S_{mn}A_mA_n\bar{A}_n + 8R_5A_n^2\bar{A}_ne^{2i\sigma_1T_2}\\ &+8R_6A_nA_m\bar{A}_me^{i\sigma_1T_2} + 8R_7A_m^2\bar{A}_ne^{-i\sigma_1T_2} + 8R_8A_n^2\bar{A}_me^{2i\sigma_1T_2}\\ &-\frac{1}{2}f_ne^{i(\sigma_1+\sigma_2)T_2}\end{aligned} \tag{8.30}$$

where S_{mm}, S_{nn}, S_{mn}, and S_{nm} are defined in Eq. (8.19) and

$$8R_1 = \int_0^1 \chi_{1m}\phi_n dx, \quad 8R_5 = \int_0^1 \chi_{1n}\phi_m dx \tag{8.31}$$

$$8R_2 = \int_0^1 \chi_{mn}\phi_n dx, \quad 8R_6 = \int_0^1 \chi_{nm}\phi_m dx \tag{8.32}$$

$$8R_3 = \int_0^1 \chi_6\phi_n dx, \quad 8R_7 = \int_0^1 \chi_6\phi_m dx \tag{8.33}$$

$$8R_4 = \int_0^1 \chi_7\phi_n dx, \quad 8R_8 = \int_0^1 \chi_7\phi_m dx \tag{8.34}$$

Next, separating real and imaginary parts in Eqs. (8.29) and (8.30), we obtain the real–valued modulation equations

$$\begin{aligned}a_n' &= -\mu a_n - \frac{R_1}{\omega_m}a_m^3\sin\gamma_1 - \frac{R_2}{\omega_n}a_ma_n^2\sin\gamma_1\\ &-\frac{R_3}{\omega_n}a_m^2a_n\sin 2\gamma_1 + \frac{R_4}{\omega_n}a_ma_n^2\sin\gamma_1 - \frac{1}{2}\frac{f_n}{\omega_n}\sin\gamma_2\end{aligned} \tag{8.35}$$

$$\begin{aligned}a_n\beta_n' &= -\frac{S_{nn}}{\omega_n}a_n^3 - \frac{S_{nm}}{\omega_n}a_na_m^2 - \frac{R_1}{\omega_n}a_m^3\cos\gamma_1\\ &-\frac{R_2}{\omega_n}a_ma_n^3\cos\gamma_1 - \frac{R_3}{\omega_n}a_m^2a_n\cos\gamma_1\\ &-\frac{R_4}{\omega_n}a_n^2a_m\cos\gamma_1 + \frac{1}{2}\frac{f_n}{\omega_n}\cos\gamma_2\end{aligned} \tag{8.36}$$

$$a'_m = -\mu a_m + \frac{R_5}{\omega_m} a_n^3 \sin\gamma_1 - \frac{R_6}{\omega_m} a_m a_n^2 \sin\gamma_1 \\ -\frac{R_7}{\omega_m} a_m^2 a_n \sin\gamma_1 + \frac{R_8}{\omega_m} a_m a_n^2 \sin 2\gamma_1 - \frac{1}{2}\frac{f_n}{\omega_n}\sin(\gamma_1+\gamma_2) \tag{8.37}$$

$$a_m \beta'_m = -\frac{S_{mm}}{\omega_m} a_m^3 - \frac{S_{mn}}{\omega_m} a_m a_n^2 - \frac{R_5}{\omega_m} a_n^3 \cos\gamma_1 \\ -\frac{R_6}{\omega_m} a_n a_m^2 \cos\gamma_1 - \frac{R_7}{\omega_m} a_m^2 a_n \cos\gamma_1 \\ -\frac{R_8}{\omega_m} a_n^2 a_m \cos 2\gamma_1 + \frac{1}{2}\frac{f_n}{\omega_m}\cos(\gamma_1+\gamma_2) \tag{8.38}$$

where

$$\sigma_1 T_2 + \beta_n - \beta_m = \gamma_1$$

$$\sigma_2 T_2 - \beta_m = \gamma_2$$

We note that, except for the damping, the system is conservative and hence Eq.s (8.29) and (8.30) with $\mu = 0$ are derivable from the Lagrangian

$$\mathcal{L} = i\omega_n\left(A_n\bar{A}'_n - \bar{A}_n A'_n\right) + i\omega_m\left(A_m\bar{A}'_m - \bar{A}_m A'_m\right) \\ +4S_{nn}A_n^2\bar{A}_n^2 + 4S_{mm}A_m^2\bar{A}_m^2 + 8S_{mn}A_n\bar{A}_n A_m\bar{A}_m \\ +\Big[4R_3 A_n^2\bar{A}_m^2 e^{2i\sigma_1 T_2} + 8R_1\bar{A}_m^2 A_m A_n e^{i\sigma_1 T_2} + 4R_2 A_n^2\bar{A}_n\bar{A}_m e^{i\sigma_1 T_2} \\ -\frac{1}{2}f_n\bar{A}_n e^{i\sigma_2 T_2} - \frac{1}{2}f_m\bar{A}_m e^{i(\sigma_1+\sigma_2)T_2} + cc\Big] \tag{8.39}$$

Consequently,

$$S_{nm} = S_{mn}, \quad R_4 = R_5 = \frac{1}{2}R_2, \quad R_6 = 2R_1, \quad R_7 = R_1, \quad R_8 = R_3 \tag{8.40}$$

If we let $A_j = \frac{1}{2}a_j e^{i\beta_j}$, then, the transverse deflection, up to second order, for three–to–one and one–to–one resonances can be expressed as

$$v(x,t) = a_n\cos(\omega_n t + \beta_n)\phi_n(x) + a_m\cos(\omega_m t + \beta_m)\phi_m(x)$$

$$
\begin{aligned}
&+\frac{1}{2}\Bigg\{ a_n^2\Big[\cos 2(\omega_n t+\beta_n)\Gamma_{1n}(x)+\Gamma_{2n}(x)\Big]+\\
&+a_m^2\Big[\cos 2(\omega_m t+\beta_m)\Gamma_{1m}(x)+\Gamma_{2m}(x)\Big]\\
&+a_n a_m\Big[\cos((\omega_n+\omega_m)t+\beta_n+\beta_m)\Gamma_3(x)\\
&+\cos((\omega_n-\omega_m)t+\beta_n-\beta_m)\Gamma_4(x)\Big]\Bigg\}+\ldots
\end{aligned}
\tag{8.41}
$$

where we set $\epsilon = 1$.

8.3.1 Numerical Results

First, we solved the boundary–value problems, Eqs. (8.6)–(8.9) and (6.37). Then, using a symbolic manipulator (MATHEMATICA), we evaluated the integrals in Eqs. (8.19)–(8.20) and (8.31)–(8.34) in closed form. In Tables 8.2 and 8.3, we show the results of these computations. We note that all the of relations between the coefficients predicted by the Lagrangian approach hold with remarkable accuracy. In the case of one–to–one internal resonance between the first and second mode, the accuracy is within eight digits. We also observe in Table 8.2 that the coefficients of the interaction terms in the case of three–to–one internal resonance between the first antisymmetric and second symmetric modes are identically zero. Hence, even though the ratio between the natural frequencies is three–to–one, the first antisymmetric and second symmetric modes are not coupled in the nonlinear sense and cannot exchange energy. In fact, we could not activate experimentally this internal resonance.

Table 8.2: Three–to–One Internal Resonance between the mth and nth Modes
The coefficients S_{ij} and Λ_i in Eqs. (8.16) and (8.17)

m	n	S_{mm}	S_{nn}	S_{mn}	S_{nm}	Λ_m	Λ_n
3	1	42.978	7742.434	−185.938	−185.961	−223.356	−74.451
2	3	−65.541	2463.383	18.653	18.653	0	0

Table 8.3: One–to–One Internal Resonance between the mth and nth Modes
The coefficients S_{ij} and R_i in Eqs. (8.29) and (8.30)

m	n	S_{mm}	S_{nn}	S_{mn}	S_{nm}	R_3	R_8
1	2	71.317	−92.168	234.908	234.908	158.043	158.043
3	4	6330.312	−2708.861	3023.806	3024.666	1314.053	1314.108

and $R_1 = R_2 = R_4 = R_5 = R_6 = R_7 = 0$

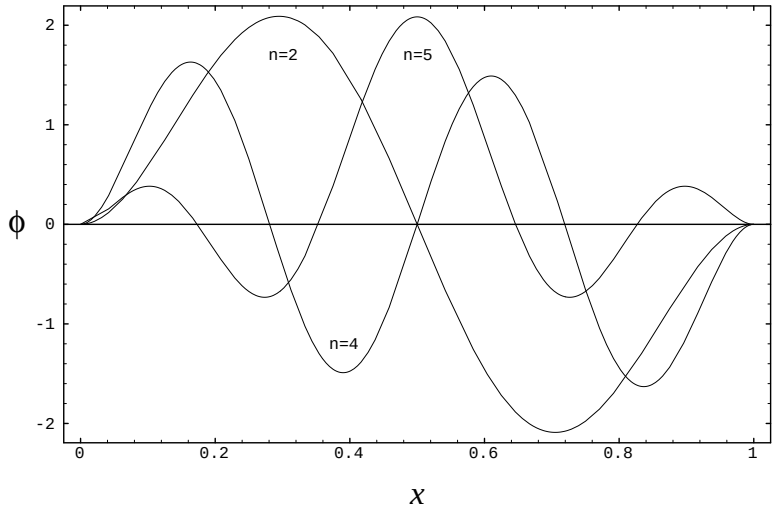

Figure 8.8: The second, fourth, and fifth mode shapes for the case of simultaneous resonance when $b = 23.312$.

8.4 Simultaneous Resonances

In this section, we determine a second–order uniform expansion for the solution of Eqs. (6.2) and (6.3) when $b \approx 23.312$. At this buckling level, $\omega_4 \approx 4\omega_2$ and $\omega_3 \approx \omega_2 + \omega_4$. If the excitation frequency is such that $2\Omega \approx \omega_4$, it follows that $\Omega \approx 2\omega_2$ and $2\Omega \approx \omega_3 - \omega_2$. Consequently, there are three possible simultaneous resonances: a subharmonic resonance of order one–half of the first antisymmetric mode, a superharmonic resonance of order two of the second antisymmetric mode, and a subcombination resonance involving the second and third modes. In Fig. 8.8, we show the second, fourth, and fifth mode shapes when $b = 23.312$. In Fig. 8.9, we show the power spectra of the response and the excitation when the excitation frequency and amplitude are, respectively, 219.53 Hz and 0.164 *g*. The response is a low-amplitude nonresonant single-mode motion. In Fig. 8.10, we show the power spectra of the response and excitation when the excitation frequency and amplitude are, respectively, 221.87 Hz and 0.176 *g*. The second, fourth, and fifth modes are simultaneously

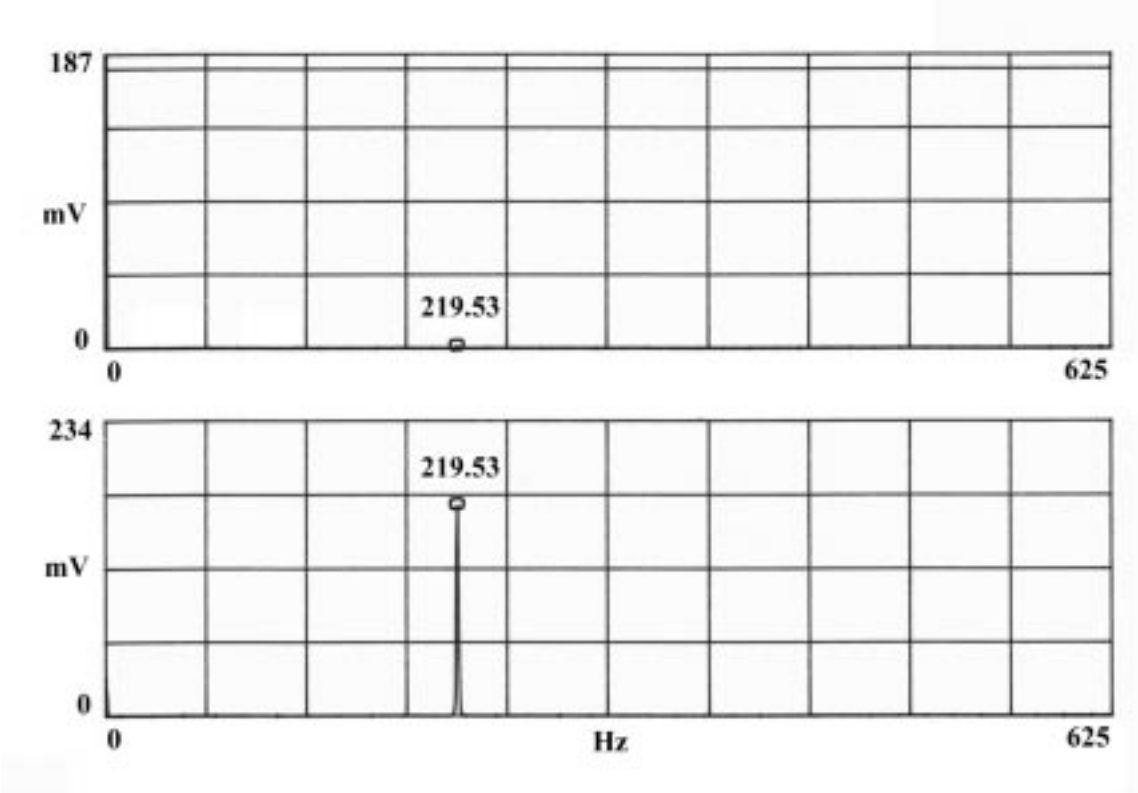

Figure 8.9: Power spectra of the response and excitation for the case of simultaneous resonances for Beam I when the excitation frequency and amplitude are, respectively, 219.53 Hz and 0.164 g.

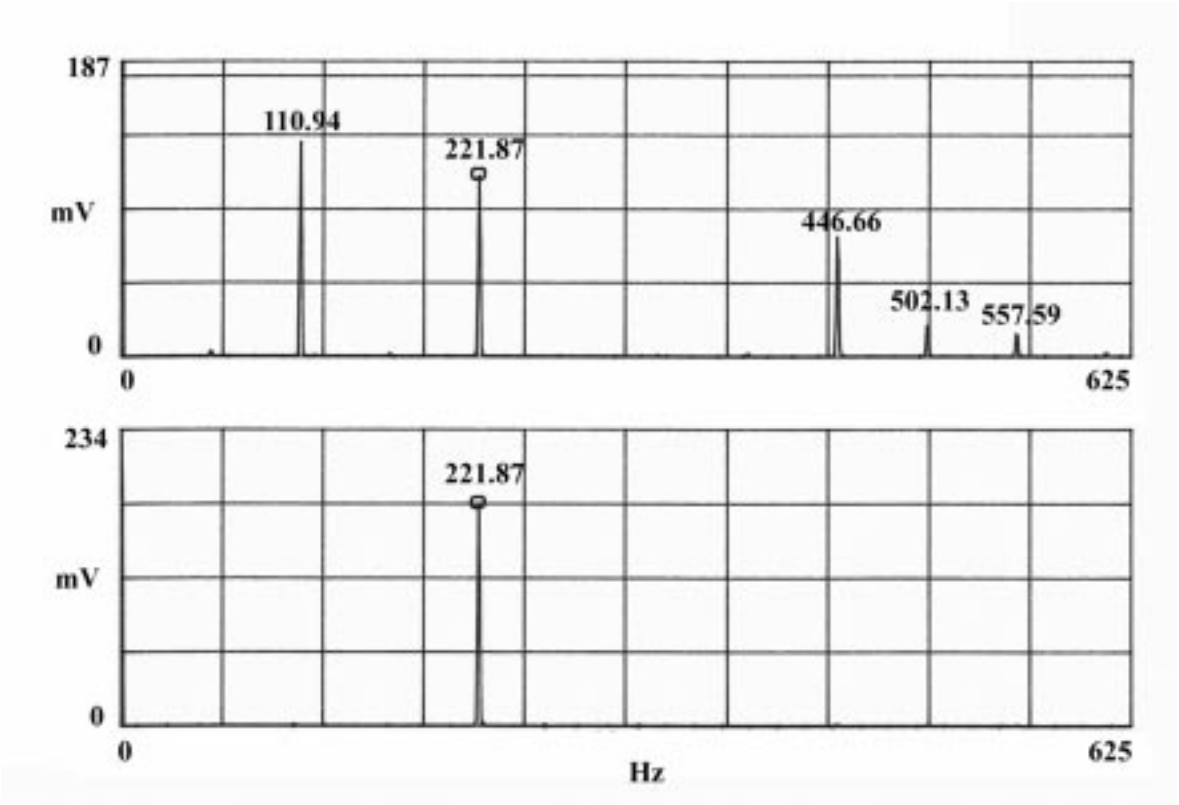

Figure 8.10: Power spectra of the response and excitation for the case of simultaneous resonances for Beam I when the excitation frequency and amplitude are, respectively, 221.87 Hz and 0.176 g.

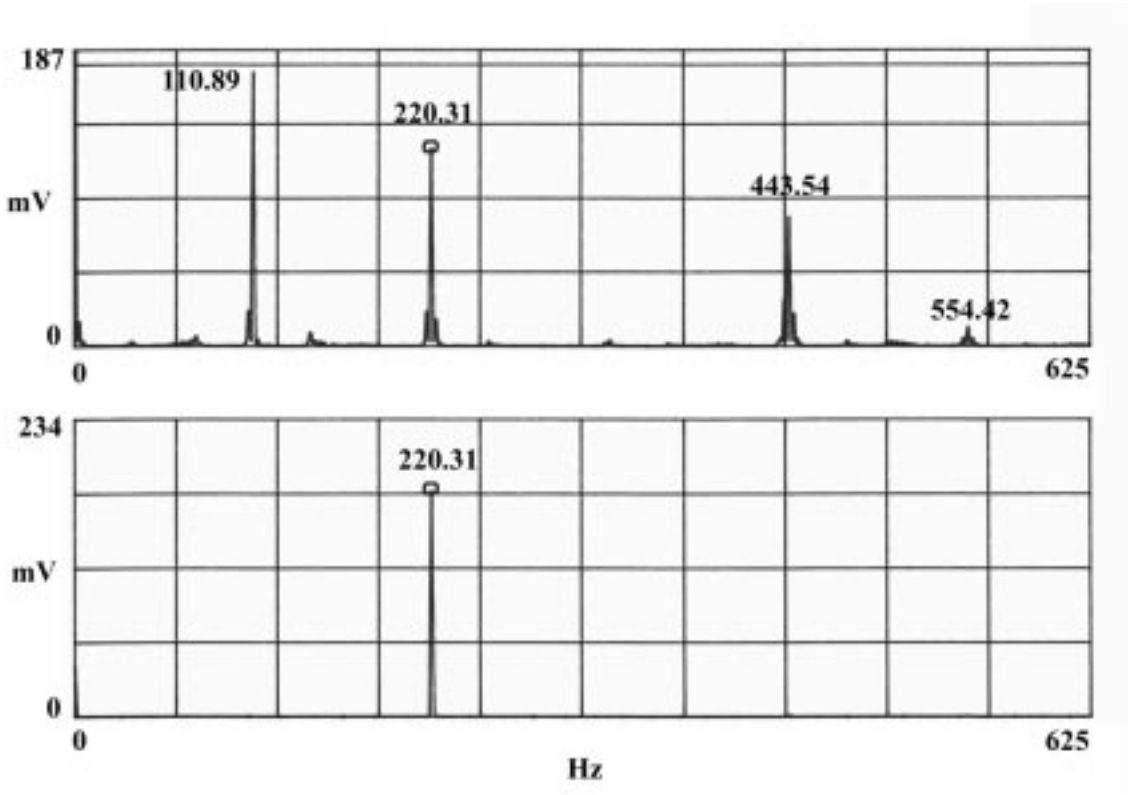

Figure 8.11: Power spectra of the response and excitation in the case of a simultaneous resonance for Beam I when the excitation frequency and amplitude are, respectively, 220.31 Hz and 0.176 g.

excited. In Fig. 8.11, we show the power spectra of the response and excitation when the excitation frequency and amplitude are, respectively, 220.31 Hz and 0.176 g. The nonlinear motion exhibits a clear side-band structure.

The multiple–scale analysis applied to the integro–partial–differential equation and boundary conditions shows that, for uniformly distributed symmetric excitations, the second antisymmetric mode is not excited by the superharmonic resonance because the forcing term produced by the resonance is orthogonal to that eigenmode. Instead, it is the subcombination resonance that is responsible for the activation of the second antisymmetric mode.

Because the effects of the activated resonances will appear at order ϵ^2, we seek a solution that depends on the scales T_0, T_1, and T_2; that is,

$$v(x,t;\epsilon) = \epsilon v(x,T_0,T_1,T_2) + \epsilon^2 v_2(x,T_0,T_1,T_2) + \epsilon^3 v_3(x,T_0,T_1,T_2) + \cdots \tag{8.42}$$

where $T_0 = t$ is a fast scale, describing motions occurring at the natural frequencies of the interacting modes and the excitation frequency, and $T_1 = \epsilon t$ and $T_2 = \epsilon^2 t$ are slow scales, describing the modulation of the amplitudes and phases of the excited modes with the nonlinearity, damping, and resonances. The activation of the simultaneous secondary resonances requires that $F = O(1)$. In order that the nonlinearity balance the effects of the damping and excitation, we replace c with $\epsilon^2 c$. In terms of the scales T_n, the time derivatives become

$$\frac{d}{dt} = D_0 + \epsilon D_1 + \epsilon^2 D_2 + \cdots \tag{8.43}$$

$$\frac{d^2}{dt^2} = D_0^2 + 2\epsilon D_0 D_1 + \epsilon^2 (D_1 + 2D_0 D_2) + \cdots \tag{8.44}$$

Substituting Eqs. (8.42)–(8.44) into Eqs. (6.2) and (6.3) and equating coefficients of like powers of ϵ, we obtain

Order ϵ:

$$\mathcal{L}(v_1) = F(x)\cos(\Omega t) \tag{8.45}$$

Order ϵ^2:

$$\mathcal{L}(v_2) = b\pi\left[v_1''\int_0^1 v_1'\sin 2\pi x dx + \pi\cos 2\pi x\int_0^1 (v_1')^2\,dx\right] - 2D_0D_1v_1 \tag{8.46}$$

Order ϵ^3:

$$\begin{aligned}\mathcal{L}(v_3) = b\pi\Big[&v_1''\int_0^1 \sin 2\pi x dx + v_2''\int_0^1 v_1'\sin 2\pi x dx\\ &+2\pi\cos 2\pi x\int_0^1 v_1'v_2'dx\Big] + \frac{1}{2}v_1''\int_0^1 v_1'^2dx\\ &-2D_0D_2v_1 - D_1^2v_1 - 2D_0D_1v_2 - 2\mu D_0v_1\end{aligned} \tag{8.47}$$

$$v_i = 0 \ \text{ and } \ v_i' \ \text{ at } \ x = 0 \ \text{ and } \ 1,\ i = 1,2,3 \tag{8.48}$$

The solution of the first–order problem, Eqs. (8.45) and (8.48), is assumed to consist of the three excited modes as well as a particular solution; that is,

$$v_1 = A_2(T_1,T_2)\phi_2 e^{i\omega_2T_0} + A_3(T_1,T_2)\phi_3 e^{i\omega_3T_0} + A_4(T_1,T_2)\phi_4 e^{i\omega_4T_0} + \phi_p e^{i\Omega T_0} + cc \tag{8.49}$$

where the complex–valued functions $A_n(T_1,T_2)$ are determined by imposing the solvability conditions at second and third orders, and ϕ_p is a solution of

$$\mathcal{L}(\phi_p) = \frac{1}{2}F(x)e^{i\Omega T_0} + cc \tag{8.50}$$

Substituting Eq. (8.49) into Eq. (8.46) yields

$$\begin{aligned}\mathcal{L}(v_2) = &-2i\omega_2D_1A_2\phi_2e^{i\omega_2T_0} - 2i\omega_3D_1A_3\phi_3e^{i\omega_3T_0}\\ &-2i\omega_4D_1A_4\phi_4e^{i\omega_4T_0} + h_{22}(x)A_2^2e^{2i\omega_2T_0}\end{aligned}$$

$$
\begin{aligned}
&+h_{33}(x)A_3^2 e^{2i\omega_3 T_0} + h_{44}(x)A_4^2 e^{2i\omega_4 T_0} \\
&+h_{23}(x)\left[A_2 A_3 e^{i(\omega_2+\omega_3)T_0} + A_3\bar{A}_2 e^{i(\omega_3-\omega_2)T_0}\right] \\
&+h_{24}(x)\left[A_2 A_4 e^{i(\omega_2+\omega_4)T_0} + A_4\bar{A}_2 e^{i(\omega_4-\omega_2)T_0}\right] \\
&+h_{34}(x)\left[A_3 A_4 e^{i(\omega_3+\omega_4)T_0} + A_3\bar{A}_4 e^{i(\omega_3-\omega_4)T_0}\right] \\
&+h_{2p}(x)\left[A_2 e^{i(\Omega+\omega_2)T_0} + \bar{A}_2 e^{i(\Omega-\omega_2)T_0}\right] \\
&+h_{3p}(x)\left[A_3 e^{i(\Omega+\omega_3)T_0} + \bar{A}_3 e^{i(\Omega-\omega_3)T_0}\right] \\
&+h_{4p}(x)\left[A_4 e^{i(\Omega+\omega_4)T_0} + \bar{A}_4 e^{i(\Omega-\omega_4)T_0}\right] + h_{pp}(x)e^{2i\Omega T_0} \\
&+h_{22}(x)A_2\bar{A}_2 + h_{33}(x)A_3\bar{A}_3 + h_{44}(x)A_4\bar{A}_4 + h_{pp}(x) + cc
\end{aligned} \tag{8.51}
$$

where

$$
h_{nn}(x) = b\pi\left[\phi_n''\int_0^1 \phi_n' \sin 2\pi x dx + \pi\cos 2\pi x\int_0^1 \phi_n'^2 dx\right] \tag{8.52}
$$

$$
h_{pp}(x) = b\pi\left[\phi_p''\int_0^1 \phi_p' \sin 2\pi x dx + \pi\cos 2\pi x\int_0^1 \phi_p'^2 dx\right] \tag{8.53}
$$

$$
\begin{aligned}
h_{nm}(x) = b\pi\Big[&\phi_n''\int_0^1 \phi_m' \sin 2\pi x dx + \phi_m''\int_0^1 \phi_n' \sin 2\pi x dx \\
&+2\pi\cos 2\pi x\int_0^1 \phi_n'\phi_m' dx\Big]
\end{aligned} \tag{8.54}
$$

$$
\begin{aligned}
h_{np}(x) = b\pi\Big[&\phi_n''\int_0^1 \phi_p' \sin 2\pi x dx + \phi_p''\int_0^1 \phi_n' \sin 2\pi x dx \\
&+2\pi\cos 2\pi x\int_0^1 \phi_n'\phi_p' dx\Big]
\end{aligned} \tag{8.55}
$$

To express the nearness of the resonances, we introduce the detuning parameters σ_i defined by

$$
\Omega = 2\omega_2 + \epsilon\sigma_1, \quad 2\Omega = \omega_4 + \epsilon\sigma_2 \ \text{ and } \ \omega_3 = \omega_2 + \omega_4 + \epsilon\sigma_3 \tag{8.56}
$$

Because the homogeneous problem governing v_2 has a nontrivial solution, the corresponding nonhomogeneous problem has a solution only if the right–hand side of Eq. (8.51) is orthogonal to every solution of the adjoint homogeneous problem governing v_2. Since the problem

under consideration is self–adjoint, the adjoints are given by $\phi_j(x)\exp(\pm i\omega_j T_0)$. Demanding that the right–hand side of Eq. (8.51) be orthogonal to $\phi_2\exp(-i\omega_2 T_0)$, $\phi_3\exp(-i\omega_3 T_0)$, and $\phi_4\exp(-i\omega_4 T_0)$ yields the solvability conditions

$$2i\omega_2 D_1 A_2 = A_3\bar{A}_4 e^{i\sigma_3 T_1}\int_0^1 h_{34}\phi_2 dx + \bar{A}_2 e^{i\sigma_1 T_1}\int_0^1 h_{2p}\phi_2 dx \tag{8.57}$$

$$2i\omega_3 D_1 A_3 = A_4 A_2 e^{-i\sigma_3 T_1}\int_0^1 h_{24}\phi_3 dx \tag{8.58}$$

$$2i\omega_4 D_1 A_4 = e^{i\sigma_2 T_1}\int_0^1 h_{pp}\phi_4 dx + A_3\bar{A}_2 e^{i\sigma_3 T_1}\int_0^1 h_{23}\phi_4 dx \tag{8.59}$$

Next, we use Eqs. (8.57)–(8.59) to replace $D_1 A_i$ in Eq. (8.51) to render the second–order problem solvable. Then, we express the particular solution of the second–order problem as

$$\begin{aligned}
v_2 = {} & \psi_{22}(x)A_2^2 e^{2i\omega_2 T_0} + \psi_{33}(x)A_3^2 e^{2i\omega_3 T_)} + \psi_{44}(x)A_4^2 e^{2i\omega_4 T_0} \\
& + \psi_{pp}(x)e^{2i\Omega T_0} + \psi_{23}(x)A_2 A_3 e^{i(\omega_2+\omega_3)T_0} + \psi_{32}(x)A_3\bar{A}_2 e^{i(\omega_3-\omega_2)T_0} \\
& + \psi_{24}(x)A_2 A_4 e^{i(\omega_2+\omega_4)T_0} + \psi_{42}(x)A_4\bar{A}_2 e^{i(\omega_4-\omega_2)T_0} + \psi_{34}(x)A_3 A_4 e^{i(\omega_3+\omega_4)T_0} \\
& + \psi_{43}(x)A_3\bar{A}_4 e^{i(\omega_3-\omega_4)T_0} + \psi_{2p}(x)A_2 e^{i(\Omega+\omega_2)T_0} + \psi_{p2}(x)\bar{A}_2 e^{i(\Omega-\omega_2)T_0} \\
& + \psi_{3p}(x)A_3 e^{i(\Omega+\omega_3)T_0} + \psi_{p3}(x)\bar{A}_3 e^{i(\Omega-\omega_3)T_0} + \psi_{4p}(x)A_4 e^{i(\Omega+\omega_4)T_0} \\
& + \psi_{p4}(x)\bar{A}_4 e^{i(\Omega-\omega_4)T_0} + \psi_2(x)A_2\bar{A}_2 + \psi_3(x)A_3\bar{A}_3 + \\
& \psi_4(x)A_4\bar{A}_4 + \psi_p(x) + cc
\end{aligned} \tag{8.60}$$

where the ψ_i are given by

$$M(\psi_{jj}; 2\omega_j) = h_{jj}(x), \quad j = 2,3,4 \tag{8.61}$$

$$M(\psi_{pp}; 2\Omega) = h_{pp} - \phi_p\int_0^1 h_{pp}\phi_p dx \tag{8.62}$$

$$M(\psi_{23}; \omega_2+\omega_3) = h_{23}(x) \tag{8.63}$$

$$M(\psi_{32}; \omega_3-\omega_2) = h_{23}(x) - \phi_4\int_0^1 h_{23}\phi_4 dx \tag{8.64}$$

$$M(\psi_{24}; \omega_2+\omega_4) = h_{24}(x) \tag{8.65}$$

$$M(\psi_{42}; \omega_4-\omega_2) = h_{24}(x) - \phi_3\int_0^1 h_{24}\phi_3 dx \tag{8.66}$$

$$M(\psi_{34};\omega_3+\omega_4)=h_{34}(x) \tag{8.67}$$

$$M(\psi_{43};\omega_3-\omega_4)=h_{34}(x)-\phi_2\int_0^1 h_{34}\phi_2 dx \tag{8.68}$$

$$M(\psi_{jp};\Omega+\omega_j)=h_{jp}(x),\quad j=2,3,4 \tag{8.69}$$

$$M(\psi_{pj};\Omega-\omega_j)=h_{jp}(x),\quad j=3,4 \tag{8.70}$$

$$M(\psi_{p2};\omega-\omega_2)=h_{2p}(x)-\phi_2\int_0^1 h_{2p}\phi_2 dx \tag{8.71}$$

$$M(\psi_j;0)=h_{jj}(x),\quad j=2,3,4 \tag{8.72}$$

$$M(\psi_p;0)=h_{pp}(x) \tag{8.73}$$

the operator M is given by Eq. (6.38), and the boundary conditions on all the ψ_j are given by Eq. (6.37).

Substituting Eqs. (8.49) and (8.60) into Eq. (8.47) and accounting for the resonance conditions given by Eq. (8.56), we obtain

$$\begin{aligned}\mathcal{L}(v_3)=&-\left[2i\omega_2(D_2A_2+\mu A_2)\phi_2-\chi_{22}A_2^2\bar{A}_2-\chi_{23}A_2A_3\bar{A}_3-\chi_{24}A_2A_4\bar{A}_4\right.\\&\left.-\chi_{2p}\,A_2+D_1^2A_2\phi_2\right]e^{i\omega_2T_0}-\left[2i\omega_3(D_2A_3+\mu A_3)\phi_3-\chi_{33}A_3^2\bar{A}_3\right.\\&\left.-\chi_{32}A_3A_2\bar{A}_2-\chi_{34}\,A_3A_4\bar{A}_4-\chi_{3p}A_3+D_1^2A_3\phi_3\right]e^{i\omega_3T_0}\\&-\left[2i\omega_4(D_2A_4+\mu A_4)-\chi_{44}A_4^2\bar{A}_4-\chi_{42}A_4A_2\bar{A}_2-\chi_{43}A_4A_3\bar{A}_3\right.\\&\left.-\chi_{4p}A_4+D_1^2A_4\phi_4\right]e^{i\omega_4T_0}-2i(\omega_3-\omega_2)D_1A_3\bar{A}_2\psi_{32}e^{i(\omega_3-\omega_2)T_0}\\&-2i(\omega_2+\omega_4)D_1A_2A_4\psi_{24}e^{i(\omega_2+\omega_4)T_0}\\&-2i(\Omega-\omega_2)D_1\bar{A}_2\psi_{p2}e^{i(\Omega-\omega_2)T_0}+cc+NST\end{aligned} \tag{8.74}$$

where

$$\begin{aligned}\chi_{jj}=&\,b\pi\left[\phi_j''\int_0^1(\psi_{jj}'+2\psi_j')\sin 2\pi x dx\right.\\&\left.+(\psi_{jj}''+2\psi_j'')\int_0^1\phi_j'\sin 2\pi x dx+2\pi\cos 2\pi x\int_0^1\phi_j'(\psi_{jj}'+2\psi_j')dx\right]\\&+\frac{3}{2}\phi_j''\int_0^1\phi_j'^2dx,\quad j=2,3,4\end{aligned} \tag{8.75}$$

$$\chi_{ij} = b\pi \left[\phi_j'' \int_0^1 (\psi_{ij}' \psi_{ji}') \sin 2\pi x dx \right.$$
$$+2\phi_i'' \int_0^1 \psi_j' \sin 2\pi x dx + (\psi_{ij}'' + \psi_{ji}'') \int_0^1 \phi_j' \sin 2\pi x dx + 2\psi_j'' \int_0^1 \phi_i' dx$$
$$\left. +2\pi \cos 2\pi x \int_0^1 \left[(\psi_{ij}' + \psi_{ji}') \phi_j' + 2\psi_j' \phi_i' \right] dx \right]$$
$$+ \left[\phi_i'' \int_0^1 \left(\phi_j' \right)^2 dx + 2\phi_j'' \int_0^1 \phi_i' \phi_j' dx \right], \quad ij = 23, 24, 34 \tag{8.76}$$

$$\chi_{jp} = b\pi \left[\phi_p'' \int_0^1 (\psi_{jp}' + \psi_{pj}') \sin 2\pi x dx + 2\phi_j'' \int_0^1 \psi_p' \sin 2\pi x dx \right.$$
$$+(\psi_{jp}'' + \psi_{pj}'') \int_0^1 \phi_p' \sin 2\pi x dx + 2\psi_p'' \int_0^1 \phi_j' \sin 2\pi x dx$$
$$\left. +2\ \pi \cos 2\pi x \int_0^1 \left[(\psi_{jp}' + \psi_{pj}') \phi_p' + 2\psi_p' \phi_j' \right] dx \right]$$
$$+ \left[\phi_j'' \int_0^1 \phi_p'^2 dx + 2\phi_p'' \int_0^1 \phi_j' \phi_p' dx \right], \quad j = 2, 3, 4 \tag{8.77}$$

and $\chi_{ji} (ji = 32, 42, 43)$ can be obtained from χ_{ij} by permuting the indices i and j. Demanding that the right–hand side of Eq. (8.74) be orthogonal to $\phi_2 \exp(-i\omega_2 T_0)$, $\phi_3 \exp(-i\omega_3 T_0)$, and $\phi_4 \exp(-i\omega_4 T_0)$ yields the following solvability conditions:

$$2i\omega_2 \left(D_2 A_2 + \mu A_2 \right) = 8S_{22} A_2^2 \bar{A}_2 + 8S_{23} A_2 A_3 \bar{A}_3 + 8S_{24} A_2 A_4 \bar{A}_4$$
$$+2S_{20} A_2 - D_1^2 A_2 - 2i(\Omega - \omega_2) e^{i\sigma_2 T_1} D_1 \bar{A}_2 \int_0^1 \psi_{p2} \phi_2 dx$$
$$-2i(\omega_3 - \omega_4) e^{i\sigma_3 T_1} D_1 A_3 \bar{A}_4 \int_0^1 h_{34} \phi_2 dx \tag{8.78}$$

$$2i\omega_3 \left(D_2 A_3 + \mu A_3 \right) = 8S_{33} A_3^2 \bar{A}_3 + 8S_{32} A_3 A_2 \bar{A}_2 + 8S_{34} A_3 A_4 \bar{A}_4 + 2S_{30} A_3$$
$$-D_1^2 A_3 - 2i(\omega_2 + \omega_4) e^{-i\sigma_3 T_1} \int_0^1 \psi_{24} \phi_3 dx + cc \tag{8.79}$$

$$2i\omega_4 \left(D_2 A_4 + \mu A_4 \right) = S_{44} A_4^2 \bar{A}_4 + S_{42} A_4 A_2 \bar{A}_2 + S_{43} A_4 A_3 \bar{A}_3 + 2S_{40} A_4$$
$$-D_1^2 A_4 - 2i(\omega_3 - \omega_2) e^{i\sigma_3 T_1} D_1 A_3 \bar{A}_2 \int_0^1 \psi_{32} \phi_4 dx + cc \tag{8.80}$$

where

$$8S_{ij} = \int_0^1 \kappa_{ij} \phi_i dx$$

$$2S_{io} = \int_0^1 \kappa_{ip}\phi_i dx \tag{8.81}$$

The deflection, up to second order, can be expressed as

$$\begin{aligned}
v(x,t) = {} & a_2\cos(\omega_2 t+\beta_2)\phi_2(x) + a_3\cos(\omega_3 t+\beta_3)\phi_3(x) \\
& + a_4\cos(\omega_4 t+\beta_4)\phi_4(x) + \cos(\Omega t)\phi_p(x) \\
& + \frac{1}{2}\Bigg\{ a_2^2\Big[\cos 2(\omega_2 t+\beta_2)\psi_{22}(x) + \psi_2(x)\Big] \\
& + a_3^2\Big[\cos 2(\omega_3 t+\beta_3)\psi_{33}(x) + \psi_3(x)\Big] \\
& + a_4^2\Big[\cos 2(\omega_4 t+\beta_4)\psi_{44}(x) + \psi_4(x)\Big] \\
& + a_2a_3\Big[\cos((\omega_2+\omega_3)t+\beta_2+\beta_3)\psi_{23}(x) \\
& + \cos((\omega_3-\omega_2)t+\beta_2-\beta_3)\Gamma_{32}(x)\Big] \\
& + a_2a_4\Big[\cos((\omega_2+\omega_4)t+\beta_2+\beta_4)\psi_{24}(x) \\
& + \cos((\omega_4-\omega_2)t+\beta_4-\beta_2)\Gamma_{42}(x)\Big] \\
& + a_3a_4\Big[\cos((\omega_3+\omega_4)t+\beta_3+\beta_4)\psi_{34}(x) \\
& + \cos((\omega_3-\omega_4)t+\beta_3-\beta_4)\Gamma_{43}(x)\Big] \\
& + a_2\Big[\cos((\Omega+\omega_2)t+\beta_2)\psi_{2p}(x) \\
& + \cos((\Omega-\omega_2)t-\beta_2)\Gamma_{p2}(x)\Big] \\
& + a_3\Big[\cos((\Omega+\omega_3)t+\beta_3)\psi_{3p}(x) \\
& + \cos((\Omega-\omega_3)t-\beta_3)\Gamma_{p3}(x)\Big] \\
& + a_4\Big[\cos((\Omega+\omega_4)t+\beta_4)\psi_{4p}(x) \\
& + \cos((\Omega-\omega_4)t-\beta_4)\Gamma_{p4}(x)\Big] + \psi_{pp}(x)\cos 2\Omega t + \psi_p(x)\Bigg\} + ...
\end{aligned} \tag{8.82}$$

$$\tag{8.83}$$

where we set $\epsilon = 1$.

8.5 Boundary–Value Problems

The boundary–value problems are governed by linear fourth–order integral–differential equations and four linear, homogeneous boundary conditions; that is,

$$M(\Gamma;\omega) = \Gamma^{iv} + 4\pi^2\Gamma'' - \omega^2\Gamma - 2b^2\pi^3 \cos 2\pi x \int_0^1 \Gamma' \sin 2\pi x dx = B(x) \tag{8.84}$$

$$\Gamma = 0 \ \text{ and } \ \Gamma' = 0 \ \text{ at } \ x = 0 \ \text{ and } \ 1 \tag{8.85}$$

where $B(x)$ represents the known nonhomogeneous term. Equations (8.84) and (8.85) are solvable only if the nonhomogeneous term $B(x)$ is orthogonal to every solution of the adjoint problem; that is,

$$\int_0^1 \Gamma^*(x)B(x)dx = 0 \tag{8.86}$$

where Γ^* denotes any solution of the adjoint problem. We observe that, for any arbitrary ω and a fixed b, the system is self–adjoint; that is,

$$M(\Gamma^*;\omega) \equiv 0 \tag{8.87}$$

$$\Gamma^* = 0 \ \text{ and } \ \Gamma^{*\prime} = 0 \ \text{ at } \ x = 0 \ \text{ and } \ 1 \tag{8.88}$$

There are two possibilities:

(a) ω is not an eigenvalue and hence

$$\Gamma^* \equiv 0 \tag{8.89}$$

(b) ω is an eigenvalue and hence

$$\Gamma^* = \phi(x;\omega) \tag{8.90}$$

where $\phi(x;\omega)$ represents the eigenmode corresponding to the eigenfrequency ω.

In the first case, the solvability condition given by Eq. (8.86) is automatically satisfied. In the second case, Eq. (8.86) becomes

$$\int_0^1 \phi(x;\omega)B(x) = 0 \tag{8.91}$$

In this case, the solution of the nonhomogeneous boundary–value problem exists but it is not unique. We seek conditions to render it unique. The general solution of the boundary–value problem can be expressed as a superposition of the homogeneous solution and a particular solutions. Hence,

$$\begin{aligned}\Gamma = a_1 \sin\lambda_1 x + a_2 \cos\lambda_2 x + a_3 \sinh\lambda_2 x \\ + a_4 \cosh\lambda_2 x + a_5 \cos 2\pi x + \Gamma_p(x)\end{aligned} \tag{8.92}$$

where $\Gamma_p(x)$ represents a particular solution of Eq. (8.84). Insisting that Eq. (8.92) satisfy the differential equation and boundary conditions, given by Eqs. (8.84) and (8.85), respectively, yields

$$a_1\Lambda_1 - a_2\Lambda_2 + a_3\Lambda_3 + a_4\Lambda_4 + a_5\Lambda_5 = 0 \tag{8.93}$$

$$a_2 + a_4 + a_5 = -\Gamma_p(0) \tag{8.94}$$

$$a_1\lambda_2 + a_3\lambda_2 = -\Gamma_p'(0) \tag{8.95}$$

$$a_2 \sin\lambda_1 + a_2 \cos\lambda_1 + a_3 \sinh\lambda_2 + a_4 \cosh\lambda_2 + a_5 = -\Gamma_p(1) \tag{8.96}$$

$$a_1\lambda_1 \cos\lambda_1 - a_2\lambda_2 \sin\lambda_1 + a_3\lambda_2 \cosh\lambda_2 + a_4\lambda_2 \sinh\lambda_2 = -\Gamma_p'(1) \tag{8.97}$$

where

$$\begin{aligned}\Lambda_1 &= \frac{\lambda_1(\cos\lambda_1 - 1)}{\lambda_1^2 - 4\pi^2}, \quad \Lambda_2 = \frac{\lambda_1 \sin\lambda_1}{\lambda_1^2 - 4\pi^2} \\ \Lambda_3 &= \frac{\lambda_2(1 - \cosh\lambda_2)}{\lambda_2^2 + 4\pi^2}, \quad \Lambda_4 = -\frac{\lambda_2 \sinh\lambda_2}{\lambda_2^2 + 4\pi^2}, \quad \Lambda_5 = \frac{\omega^2}{4b^2\pi^4} - \frac{1}{2}\end{aligned} \tag{8.98}$$

We rewrite Eqs. (8.93) in matrix form as

$$A\mathbf{a} = \mathbf{b} \tag{8.99}$$

where

$$A = \begin{bmatrix} 0 & 1 & 0 & 1 & 1 \\ \lambda_1 & 0 & \lambda_2 & 0 & 0 \\ \sin\lambda_1 & \cos\lambda_1 & \sinh\lambda_2 & \cosh\lambda_2 & 1 \\ \lambda_1\cos\lambda_1 & -\lambda_1\sin\lambda_1 & \lambda_2\cosh\lambda_2 & \lambda_2\sinh\lambda_2 & 0 \\ \Lambda_1 & -\Lambda_2 & \Lambda_3 & \Lambda_4 & \Lambda_5 \end{bmatrix} \tag{8.100}$$

$$\mathbf{a}^T = [a_1, a_2, a_3, a_4, a_5] \tag{8.101}$$

$$\mathbf{b}^T = -\left[\Gamma_p(0), \Gamma_p'(0), \Gamma_p(1), \Gamma_p'(1), 0\right] \tag{8.102}$$

Because ω is an eigenvalue,

$$\det A = 0 \tag{8.103}$$

The solvability condition for the algebraic problem, Eq. (8.99), can be expressed as

$$\mathbf{y}^T\mathbf{b} = 0 \tag{8.104}$$

where $\mathbf{y}$ is any solution of the adjoint problem

$$A^T\mathbf{y} = 0 \tag{8.105}$$

If Eq. (8.86) is satisfied, then Eq. (8.104), being the algebraic counterpart of it, is satisfied, automatically.

To determine a solution of Eq. (8.99) we observe that, owing to Eq. (8.103), we can discard any arbitrary equation in the set of linear equations given by Eq. (8.99), and determine a solution to within an arbitrary constant. If we choose to discard the first equation, we can rewrite Eq. (8.99) as

$$\hat{A}\hat{\mathbf{a}} = \hat{\mathbf{b}} - a_1\mathbf{A}_1 \tag{8.106}$$

where

$$\hat{A} = [a_{ij}]\,, \quad i,j = 2,3,4,5 \tag{8.107}$$

$$\hat{\mathbf{a}} = [a_i], \qquad \hat{\mathbf{b}} = [b_i] \;\text{ and }\; \mathbf{A}_1 = [a_{i1}], \quad i = 2,3,4,5$$

Hence,

$$\hat{\mathbf{a}} = \hat{A}^{-1}[\hat{\mathbf{b}} - a_1\mathbf{A}_1] = \hat{\mathbf{a}}(a_1) \tag{8.108}$$

Therefore, the solution of Eqs. (8.84) and (8.85) can be expressed as

$$\begin{aligned}\Gamma = {} & a_1 \sin\lambda_1 x + \hat{a}_2 \cos\lambda_2 x + \hat{a}_3 \sinh\lambda_2 x \\ & + \hat{a}_4 \cosh\lambda_2 x + \hat{a}_5 \cos 2\pi x + \Gamma_p(x)\end{aligned} \tag{8.109}$$

To determine uniquely the solution, we observe that the solution of the first–order problem contains part of the homogeneous solution corresponding to the eigenvalue ω; that is,

$$\phi(x;\omega)\exp(\pm i\omega T_0)$$

Therefore, we require that solutions of the higher–order problems be orthogonal to the homogeneous term

$$\phi(x;\omega)\exp(\pm i\omega T_0)$$

This condition can be rewritten as

$$\int_0^1 \Gamma(x)\phi(x;\omega)dx = 0 \tag{8.110}$$

Substituting Eq. (8.109) and the eigenmode $\phi(x;\omega)$ into Eq. (8.110), we obtain a linear algebraic equation in the unknown a_1. Solving for a_1 and substituting the result into Eq. (8.109), we obtain a unique solution of Eqs. (8.84) and (8.85).

Chapter 9

Conclusions

9.1 Summary and Concluding Remarks

In this thesis, approximate methods for studying nonlinear vibrations of weakly nonlinear distributed-parameter systems have been discussed. Theoretical predictions have been contrasted with experimental results, thus leading to a closer, though not exhaustive, understanding of the limits of applicability of certain classical discretization methods, such as the Galerkin method. More specifically, we used a Galerkin–type discretization technique combined with the method of multiple scales and a direct approach based on the method of multiple scales to produce approximate responses of two continuous systems with quadratic and cubic nonlinearities to a harmonic excitation.

First, we analyzed the nonlinear transverse vibrations of an Euler–Bernoulli beam resting on an elastic foundation with distributed quadratic and cubic nonlinearities. Because the governing equation is a fourth–order partial–differential equation with homogeneous boundary conditions, asymptotic responses to either a primary resonance or a subharmonic

resonance of order one–half of the nth mode could be produced with a relatively modest effort by using either the single–mode Galerkin discretization or the direct approach. By evaluating regions of softening (hardening) behavior of the system, the response drift, and frequency–response curves characterizing asymmetric oscillations around the biased equilibrium, we conclude that the results obtained with both approaches are in agreement for the first mode. However, for higher modes, we find qualitative discrepancies between them in certain regions of the control parameters space.

Second, with the new understanding that deviations between the two approaches depend on the excited mode and on the control parameter values, we attacked the problem of nonlinear, planar, unimodal vibrations of a first–mode buckled beam subject to a harmonic uniform excitation. Inspired by previous studies on buckled beams and based on repeated experimental observations, we recognized the influence of initial geometric imperfections and changes in temperature on the overall dynamic behavior of a post–buckled beam. Hence, we derived the equations of motion governing small but finite–amplitude vibrations of homogeneous, isotropic, geometrically imperfect beams around the post–buckling equilibrium subject to a time–dependent end load, a change in temperature, and a distributed transverse excitation. We used a mixed analytical–numerical procedure to obtain the nonlinear equilibrium solutions in the pre– and post–buckling range. We showed the existence of null–load solutions for a clamped–clamped beam with a prescribed initial geometric imperfection provided that some conditions on the slenderness of the beam and the magnitude of the initial rise–to–span ratio are satisfied. This result raised problematically the question of the dynamic behavior of such 'non–stiff' structures. This is, to our knowledge, a completely unexplored field of investigation. However, even though the subject revealed itself very appealing, it would have represented a major digression from our initial research proposal. Hence, we defined a general exact solution procedure to study linear, undamped vibrations around an initial equilibrium of an imperfect beam. We showed that

small imperfections, on the order of magnitude of the radius of gyration of the beam, do affect quantitatively as well as qualitatively the linear and the nonlinear behavior of buckled beams. Small temperature changes, on the order of a degree Celsius, can affect significantly the frequencies for low buckling levels. However, these effects become less significant for high buckling levels.

Then, to the end of comparing the outcomes of the two mentioned approximate methods, we analyzed one of the simplest cases for a buckled beam. That is, unimodal nonlinear vibrations of an initially straight beam around its first buckling mode shape. We considered the buckling level as a control parameter and computed the effective nonlinearity coefficient by using both approaches over a broad range of the buckling level. We showed that, for the second mode, both methods yield qualitatively comparable results in the whole range of the buckling range under investigation. In contrast, for the first mode, we determined ranges of the buckling level where qualitative discrepancies occur. Because these deviations occur for high buckling levels, the assumed model of initially straight buckled beam is still valid.

Guided by the theoretical predictions, we experimentally obtained frequency–response curves of a buckled beam under a uniform base excitation by sweeping the frequency around the first natural frequency. We used two test specimens made of different steel and having different cross–sections but the same length. We obtained frequency–response curves for buckling levels where the discretization approach predicts a hardening–type behavior whereas the direct approach predicts a softening–type behavior. For both types of beams, at various excitation amplitudes, the experimentally obtained frequency–response curves exhibit a clear softening behavior. Hence, there is a full agreement between the experimental results and the predictions of the direct approach.

While exploring the control space, we observed experimentally the activation of few

internal resonances, particularly, a three–to–one resonance between the lowest symmetric modes. Therefore, by using the direct approach, we obtained asymptotic responses for some relevant internal resonance conditions. We solved a number of boundary–value problems and computed the coefficients appearing in the modulation equations characterizing multimodal interactions. In the case of simultaneous resonances, some of these boundary–value problems needed a special treatment. A theoretical treatment and a solution procedure for these problems have been derived. These results will be useful for constructing uniformly valid asymptotic expansions in the presence of multiple internal resonances under an external subharmonic or superharmonic resonance by using the direct perturbation procedure.

The main results of this thesis show that for, some distributed–parameter systems with quadratic and cubic nonlinearities, the discretization approach may yield inaccurate or, more dangerously, qualitatively wrong results for unimodal responses excited via primary resonances in certain regions of the control parameter space. The deviation is the result of postulating a priori a stationary shape for the nonlinear motion. Therefore, the spatial nonstationarity of the actual nonlinear motion is lost. On the other hand, the direct approach yields corrections to the spatial and temporal dependence of the nonlinear motion at various orders. Hence, some calculated intrinsic system properties, such as the effective nonlinearity coefficient, which depend on the spatial variation, depend on whether they are calculated with either the discretization or direct approach.

Care must be exercised in applying a finite–degree–of–freedom Galerkin–type discretization technique to distributed-parameter systems with quadratic and cubic nonlinearities. The present conclusions seem to be general and apply to a large class of weakly nonlinear continuous systems. Namely, when a system possesses even and hardening odd nonlinearities, then qualitative differences in the dynamics may arise depending on the used approximate method.

We note that application of the direct approach to continuous nonlinear structures with large numbers of elements can be very laborious if not, under certain circumstances, impracticable. Nevertheless, as general purpose approximate numerical methods for treating nonlinear systems (e.g., finite elements) have been developed in reliable software algorithms, we foresee that, in the near future, some generalized direct perturbation procedures will be implemented in software codes by using the extensive potentialities of the fourth generation programming languages.

9.2 Suggestions for future research

Several areas of research are still open for further theoretical and experimental investigation. We showed qualitative discrepancies between a Galerkin–type discretization and the direct approach for two specific distributed–parameter systems with quadratic and cubic nonlinearities by exciting a certain mode via external primary resonance. We succeeded in validating experimentally the direct approach predictions in the case of a buckled beam oscillating around its first buckling deflection. We believe that one open fertile field of investigation is purely mathematical and would result in some theorems giving conditions under which certain sets of weakly nonlinear partial–differential equations and their associated boundary conditions cannot be discretized by using finite–degree–of–freedom Galerkin–type procedures. In addition, theorems giving estimates of the errors of direct perturbation solutions would be a further progress.

More specifically, with regard to the dynamics of buckled beams, we envisage several areas of investigation. First, quantitative comparisons between the experimental results and the direct approach predictions would be of interest. With this respect, an improvement of the quantitative matching could be attained by using the developed theory of

geometrically imperfect buckled beams. No time was left to investigate the influence of prescribed geometric imperfections on the nonlinear dynamics of buckled beams. In addition, experimental work documenting extensively internal resonances in buckled beams, for different boundary conditions, can be done in the future. Asymptotic solutions for these resonances are available and bifurcation analyses of the already developed modulation equations would shed light on the the most likely complex, nonlinear multimodal dynamics of the system. Furthermore, formulation of the problem of cross–well oscillations of buckled beams around the unstable equilibria and the construction of solutions for these motions by using the direct approach would be of interest. In fact, the current knowledge of the cross–well dynamics of buckled beams is based on single–mode Galerkin discretization results.

References

Abhyankar, E. K. and Hanagud, S. V., 1993, "Chaotic vibrations of beams: numerical solution of partial differential equations," *Journal of Applied Mechanics* **60**, pp. 167–174.

Abou-Rayan, A. M., Nayfeh, A. H., Mook, D. T., and Nayfeh, M.A., 1993, "Nonlinear response of a parametrically excited buckled beam," *Nonlinear Dynamics* **4**, pp. 499–525.

Afaneh, A. A. and Ibrahim, R. A., 1993, "Nonlinear response of an initially buckled beam with 1:1 internal resonance to sinusoidal excitation," *Nonlinear Dynamics* **4**, pp. 547–572.

Antman, S. S. and Srubshchik, L. S., 1996, "Nonstiffness of axisymmetric shells," submitted for publication to *Journal of Elasticity*.

Benedettini, F., Rega, G., and Alaggio, R., 1995, "Non-linear oscillations of a four-degree-of-freedom model of a suspended cable under multiple internal resonance conditions," *Journal of Sound and Vibration* **182**, pp. 775–798.

Bhashyam, G. R. and Prathap, G., 1980, "Galerkin finite element method for non-linear beam vibrations," *Journal of Sound and Vibration* **72**, pp. 191–205.

Biezeno, C. B., 1935, "*Ü*ber die Bestimmung der 'Durchschlagkraft' einer schwachgekr*ü*mmten, kreisförmigen Platte," *Z. Angew. Math. Mech.* **15**, pp. 10–22.

Bisplinghoff, R. L. and Pian, T. H. H., 1957, "On the vibration of thermally buckled bars and plates," *Proc. IX Int. Congress Applied Mechanics* **7**, pp. 307–318.

Chin, C. and Nayfeh, A. H., 1996, "Bifurcation and chaos in externally excited circular cylindrical shells," *Journal of Applied Mechanics* **63**, pp. 565–574.

Eisley, J. G., 1964, "Large amplitude vibration of bucked beams and rectangular plates," *AIAA Journal* **2**, pp. 2207–2209.

Eisley, J. G. and Bennett, J. A., 1970, "Stability of large amplitude forced motion of a simply supported beam," *International Journal of Non-Linear Mechanics* **5**, pp. 645–657.

Finlayson, B. A., 1972, *The Method of Weighted Residuals and Variational Principles,* Academic Press, New York.

Johnson, E. R. and Plaut, R. H., 1980, "Load-frequency relationships for shallow elastic arches," Virginia Polytechnic Institute and State University, Blacksburg, VA, Rpt. VPI-E-80-4.

Kantorovich, L. V. and Krylov, V. I., 1964, *Approximate Methods of Higher Analysis*, Interscience Publishers, New York.

Karesmen E., Ileri, L. and Akkas, N., 1992, "Chaotic dynamics analysis of visco-elastic shallow spherical shells," *Computer & Structures* **44**, pp. 851–857.

Kreider, W., 1995, *Linear and nonlinear vibrations of buckled beams*, Master Thesis, Department of Engineering Science and Mechanics, Virginia Polytechnic Institute and State University, Blacksburg, VA, June.

Kreider, W., Nayfeh, A. H., and Chin, C-M., 1995, "Two–to–one resonances in buckled beams," Paper No. SYMP-95-50, *Proceedings of the 15th Biennial Conference on Mechanical Vibration and Noise,* Boston, MA, September 17-21.

Lee, B. H. and Ibrahim, R. A., 1993, "Stochastic bifurcation in nonlinear structures near 1:1 internal resonance," *AIAA Paper* No. 93-1429-CP.

Leissa, A. W. and Saad, A. M., 1994, "Large amplitude vibrations of strings," *Journal of Applied Mechanics* **61**, pp. 296–301.

McConnell, K. G., 1995, *Vibration Testing*, Wiley–Interscience, New York.

Meirovitch, L., 1996, *Principles and Techniques of Vibrations*, Prentice Hall, New York.

Mettler, E., 1962, *Dynamic Buckling*, McGraw-Hill, New York.

Min, G. B. and Eisley, J. G., 1972, "Nonlinear vibration of buckled beams," *Journal of Engineering for Industry* **94**, pp. 637–645.

Mook, D. T., Plaut, R. H., and HaQuang, N., 1985, "The influence of an internal resonance on nonlinear structural vibrations under subharmonic resonance conditions," *Journal of Sound and Vibration* **102**, pp. 473–492.

Nagai, K., 1990, "Experimental study of chaotic vibration of a clamped beam subjected to periodic lateral forces," *Transactions of the Japanese Society of Mechanical Engineering* **56**, p. 1171.

Nagai, K., and Yamaguchi, T., 1994, "Chaotic vibrations of a post–buckled beam carrying a concentrated mass," (1st Report: Experiment), *Transactions of the Japanese Society of Mechanical Engineering* **60**, p. 3733.

Nayfeh, A. H. and Mook, D. T., 1979, *Nonlinear Oscillations*, Wiley–Interscience, New York.

Nayfeh, A. H., 1981, *Introduction to Perturbation Techniques*, Wiley-Interscience, New York.

Nayfeh, A. H. and Balachandran, B., 1995, *Applied Nonlinear Dynamics*, Wiley–Interscience, New York.

Nayfeh, A. H., 1984, "On the low-frequency drumming of bowed structures," *Journal of Sound and Vibration* **94**, pp. 551–562.

Nayfeh, A.H. and Raouf, R.A., 1987, "Nonlinear forced response of infinitely long circular cylindrical shells," *Journal of Applied Mechanics* **54**, pp. 571–577.

Nayfeh, A.H., Nayfeh, J. F., and Mook, D.T., 1992, "On methods for continuous systems with quadratic and cubic nonlinearities," *Nonlinear Dynamics* **3**, pp. 145–162.

Nayfeh, A. H., Nayfeh, S. A., and Pakdemirli, M., 1995, "On the discretization of weakly nonlinear spatially continuous systems," in *Nonlinear Dynamics and Stochastic Mechanics*, W. Kliemann and N. Sri Namachchivaya, eds., pp. 175–200.

Nayfeh, A. H., Kreider, W., and Anderson, T. J., 1995, "An analytical and experimental investigation of the natural frequencies and mode shapes of buckled beams," *AIAA Journal* **33**, pp. 1121–1126.

Nayfeh, A. H. and Lacarbonara, W., 1996, "On the discretization of distributed-parameter systems with quadratic and cubic nonlinearities," *Nonlinear Dynamics*, accepted for publication.

Pakdemirli, M., Nayfeh, S. A., and Nayfeh, A. H., 1995, "Analysis of one-to-one autoparametric resonances in cables-Discretization vs. direct treatment," *Nonlinear Dynamics* **8**, pp. 65–83.

Pellicano, F. and Vestroni, F., 1997, "Free nonlinear vibrations of an axially moving beam," submitted to *Recent Advances in Structural Dynamics*, Southampton, England, July.

Plaut, R. H., HaQuang, N., and Mook, D. T., 1985, "The influence of an internal resonance on nonlinear structural vibrations under two-frequency excitation," *Journal of Sound and Vibration* **107**, pp. 309–319.

Ramu, S. A., Sankar, T.S., and Ganesan, R., 1994, "Bifurcations, catastrophes and chaos in a pre-buckled beam," *International Journal of Non-Linear Mechanics* **29**, pp. 449–462.

Raouf, R.A. and Nayfeh, A.H., 1990, "One-to-one autoparametric resonances in infinitely long cylindrical shells," *Computer & Structures* **35**, pp. 163–173.

Rega, G., Lacarbonara, W., and Nayfeh, A. H., 1996, "Direct perturbation approach to finite oscillations of suspended cables under multiple internal resonance conditions," AiM'96 Conference, St. Petersburg, Russia, October.

Srubshchik, L. S., 1967, "Nonstiffness of spherical shells," *Journal of Applied Mathematics and Mechanics (PMM)* **31**, pp. 737–743.

Srubshchik, L. S., 1972, "On the question of nonrigidity in the nonlinear theory of gently sloping shells," *Math. USSR Izvesija* **6**, pp. 883–903.

Thomsen, J. J., 1992, "Chaotic vibrations of non-shallow arches," *Journal of Sound and Vibration* **153**, pp. 239–258.

Tien, W-M, Namachchivaya, N. S., and Bajaj, A. K., 1994, "Non-linear dynamics of a shallow arch under periodic excitation-I. 1:2 internal resonance," *International Journal of Non-Linear Mechanics* **29**, pp. 349–366.

Tien, W-M, Namachchivaya, N. S., and Malhotra, N., 1994, "Non-linear dynamics of a shallow arch under periodic excitation-II. 1:1 internal resonance," *International Journal of Non-Linear Mechanics* **29**, pp. 367–386.

Tseng, W.-Y. and Dugundji, J., 1971, "Nonlinear vibrations of a buckled beam under a harmonic excitation," *Journal of Applied Mechanics* **38**, 467–476.

Troger, H. and Steindl, A., 1991, *Nonlinear Stability and Bifurcation Theory*, Springer-Verlag, Wien.

Vorovich, I. I., 1957, "O sushchestovanii reshenii v nelineoinoi teorii obolochek," *Dokl. Akad. Nauk. SSSR* **117**, pp. 203–206.

Yamaguchi, T. and Nagai, K., 1994, "Chaotic vibrations of a post-buckled beam carrying a concentrated mass," (2nd Report: Theoretical Analysis), *Transactions of the Japanese Society of Mechanical Engineering* **60**, p. 3741.

Yamaki, N. and Mori, A., 1980, "Non-linear vibrations of a clamped beam with initial defection and initial axial displacement, Part I: Theory," *Journal of Sound and Vibration* **71**, pp. 333–346.

Appendix A

The Functions Ψ_1 and Ψ_2

The solution strategy of Eqs. (6.36) and (6.37), for $i = 1$, consists of treating the homogeneous integral term as an inhomogeneous term. Thus, let

$$\Gamma_1 = \pi \int_0^1 \sin 2\pi x \phi' dx \quad \text{and} \quad \Gamma_2 = \int_0^1 (\phi')^2 dx \tag{A.1}$$

Upon consideration of the definition of ϕ, Eq. (6.36) becomes

$$\begin{aligned} \Psi_1^{iv} + 4\pi^2 \Psi_1'' = \cos 2\pi x \left(2\pi^2 b^2 \int_0^1 \phi' \Psi_1' dx + \pi^2 \Gamma_2 - 4\pi^2 c_5 \Gamma_1 \right) \\ + \Gamma_1 \Big(- c_1 \lambda_1^2 \sin \lambda_1 x - c_2 \lambda_1^2 \cos \lambda_1 x + c_3 \lambda_2^2 \sinh \lambda_2 x + c_4 \lambda_2^2 \cosh \lambda_2 x \Big) \end{aligned} \tag{A.2}$$

We express the homogeneous solution of Eq. (A.2) as

$$\Psi_{1h}(x) = d_1 \sin 2\pi x + d_2 \cos 2\pi x + d_3 x + d_4 \tag{A.3}$$

Then, by employing the method of undetermined coefficients, we expect that a particular solution of Eq. (A.2) will have the form

$$\begin{aligned} \Psi_{1p}(x) = d_5 \sin \lambda_1 x + d_6 \cos \lambda_1 x + d_7 \sin h \lambda_2 x \\ + d_8 \cosh \lambda_2 x + d_9 x \sin 2\pi x + d_{10} x \cos 2\pi x \end{aligned} \tag{A.4}$$

The general solution of Eq. (A.2) is the superposition of the homogeneous and a particular solution. That is,

$$\Psi_1(x) = \Psi_{1h}(x) + \Psi_{1p}(x) \tag{A.5}$$

Requiring that Eq. (A.5) satisfy Eq. (A.2) yields

$$\begin{aligned} 2b^2\pi d_2 - \left(\frac{1}{2}b^2 + 16\right) d_9 &= \frac{\Gamma_2}{\pi} - \frac{4\Gamma_1 c_5}{\pi} \\ +d_5 \left(\lambda_1 g_1 - \lambda_1 k_1 g_2 + \lambda_2 k_2 g_3 + \lambda_2 k_3 g_4\right) & \end{aligned} \tag{A.6}$$

where

$$g_1 = \int_0^1 \sin 2\pi x \cos \lambda_1 x dx = 2\pi \frac{\cos \lambda_1 - 1}{\lambda_1^2 - 4\pi^2} \tag{A.7}$$

$$g_2 = \int_0^1 \sin 2\pi x \sin \lambda_1 x dx = 2\pi \frac{\sin \lambda_1}{\lambda_1^2 - 4\pi^2} \tag{A.8}$$

$$g_3 = \int_0^1 \sin 2\pi x \cosh \lambda_2 x dx = 2\pi \frac{1 - \cosh \lambda_2}{\lambda_2^2 + 4\pi^2} \tag{A.9}$$

$$g_4 = \int_0^1 \sin 2\pi x \sinh \lambda_2 x dx = -2\pi \frac{\sinh \lambda_2}{\lambda_2^2 + 4\pi^2} \tag{A.10}$$

$$d_5 = -\frac{c_1\Gamma_1}{\lambda_1^2 - 4\pi^2}, \quad d_6 = -\frac{c_2\Gamma_1}{\lambda_1^2 - 4\pi^2}, \quad d_7 = \frac{c_3\Gamma_1}{\lambda_2^2 + 4\pi^2}, \quad d_8 = \frac{c_4\Gamma_1}{\lambda_2^2 + 4\pi^2}, \quad d_{10} = 0 \tag{A.11}$$

which can be rewritten as

$$d_6 = k_1 d_5, \quad d_7 = k_2 d_5, \quad d_8 = k_3 d_5 \tag{A.12}$$

where

$$k_1 = \frac{c_2}{c_1}, \quad k_2 = -\frac{c_3}{c_1}\frac{\lambda_1^2 - 4\pi^2}{\lambda_2^2 + 4\pi^2}, \quad k_3 = \frac{c_4}{c_3} k_2 \tag{A.13}$$

Therefore, $\Psi_1(x)$ can be written as

$$\begin{aligned} \Psi_1(x) = d_1 \sin 2\pi x + d_2 \cos 2\pi x + d_3 x + d_4 + d_9 x \sin 2\pi x \\ +d_5 \left(\sin \lambda_1 x + k_1 \cos \lambda_1 x + k_2 \sinh \lambda_2 x + k_3 \cosh \lambda_2 x\right) \end{aligned} \tag{A.14}$$

Enforcing the boundary conditions, Eq. (6.37), yields

$$D\mathbf{v} = \mathbf{q} \tag{A.15}$$

where $\mathbf{v}^T = [d_1, d_2, d_3, d_4, d_9]$,

$$D = \begin{Bmatrix} 0 & 1 & 0 & 1 & 0 \\ 2\pi & 0 & 1 & 0 & 0 \\ 0 & 1 & 1 & 1 & 0 \\ 2\pi & 0 & 1 & 0 & 2\pi \\ 0 & b^2 2\pi & 0 & 0 & -\left(\frac{1}{2}b^2 + 16\right) \end{Bmatrix} \tag{A.16}$$

and

$$\mathbf{q} = \begin{bmatrix} -d_5\left(k_1 + k_3\right) \\ -d_5\left(\lambda_1 + k_2\lambda_2\right) \\ -d_5\left(\sin\lambda_1 + k_1\cos\lambda_1 + k_2\sinh\lambda_2 + k_3\cosh\lambda_2\right) \\ -d_5\left(\lambda_1\cos\lambda_1 - k_1\lambda_1\cos\lambda_1 + k_2\lambda_2\cosh\lambda_2 + k_3\lambda_2\sinh\lambda_2\right) \\ \frac{\Gamma_2}{\pi} - \frac{4\Gamma_1 c_5}{\pi} + 2b^2 d_5\left(\lambda_1 g_1 - \lambda_1 k_1 g_2 + \lambda_2 k_2 g_3 + \lambda_2 k_3 g_4\right) \end{bmatrix} \tag{A.17}$$

To determine a solution for Ψ_2, we rewrite Eq. (6.36) as

$$\begin{aligned} \Psi_2^{iv} + 4\pi^2\Psi_2'' - 4\omega^2\Psi_2 = \cos 2\pi x \left(2\pi^2 b^2 \int_0^1 \phi'\Psi_2' dx + \pi^2\Gamma_2 - 4\pi^2 c_5\Gamma_1\right) \\ +\Gamma_1\left(-c_1\lambda_1^2\sin\lambda_1 x - c_2\lambda_1^2\cos\lambda_1 x + c_3\lambda_2^2\sinh\lambda_2 x + c_4\lambda_2^2\cosh\lambda_2 x\right) \end{aligned} \tag{A.18}$$

We express the homogeneous solution of Eq. (A.18) as

$$\Psi_{2h}(x) = s_1\sin\zeta_1 x + s_2\cos\zeta_1 x + s_3\sinh\zeta_2 x + s_4\cosh\zeta_2 x \tag{A.19}$$

Then, a particular solution of Eq. (A.18) can be expressed as

$$\Psi_{2p}(x) = s_5\sin\lambda_1 x + s_6\cos\lambda_1 x + s_7\sinh\lambda_2 x + s_8\cosh\lambda_2 x + s_9\cos 2\pi x \tag{A.20}$$

Hence, expressing the general solution as the superposition of the homogeneous and particular solutions and requiring it to satisfy Eq. (A.18), we obtain

$$b^2\chi_1 h_1 s_1 - b^2\chi_1 h_2 s_2 + b^2\chi_2 h_3 s_3 + b^2\chi_2 h_4 s_4 + \left(\frac{2\omega^2}{\pi^3} - \pi b^2\right) s_9 = \\ -\frac{\Gamma_2}{2\pi} + \frac{2\Gamma_1 c_5}{\pi} - b^2 s_5 \left(\lambda_1 g_1 - \lambda_1\kappa_1 g_2 + \lambda_2\kappa_2 g_3 + \lambda_2\kappa_3 g_4\right) \tag{A.21}$$

where

$$s_6 = \kappa_1 s_5, \quad s_7 = \kappa_2 s_5, \quad s_8 = \kappa_3 s_5 \tag{A.22}$$

$$\kappa_1 = \frac{c_2}{c_1}, \quad \kappa_2 = -\frac{c_3}{c_1}\frac{\lambda_2^2}{\lambda_1^2}\frac{\lambda_1^4 - 4\pi^2\lambda_1^2 - 4\omega^2}{\lambda_2^4 + 4\pi^2\lambda_2^2 - 4\omega^2}, \quad \kappa_3 = \frac{c_4}{c_3}\kappa_2 \tag{A.23}$$

$$h_1 = \int_0^1 \sin 2\pi x \cos\chi_1 x dx, \quad h_2 = \int_0^1 \sin 2\pi x \sin\chi_1 x dx, \\ h_3 = \int_0^1 \sin 2\pi x \cosh\chi_2 x dx, \quad h_4 = \int_0^1 \sin 2\pi x \sinh\chi_2 x dx \tag{A.24}$$

Hence, $\Psi_2(x)$ can be expressed as

$$\Psi_2 = s_1 \sin\zeta_1 x + s_2 \cos\zeta_1 x + s_3 \sinh\zeta_2 x + s_4 \cosh\zeta_2 x + s_9 \cos 2\pi x \\ + s_5(\sin\lambda_1 x + \kappa_1 \cos\lambda_1 x + \kappa_2 \sinh\lambda_2 x + \kappa_3 \cosh\lambda_2 x) \tag{A.25}$$

Enforcing the boundary conditions, Eq. (6.37), yields

$$S\mathbf{z} = \mathbf{w} \tag{A.26}$$

where $\mathbf{z}^T = [s_1, s_2, s_3, s_4, s_9]$,

$$S = \begin{Bmatrix} 0 & 1 & 0 & 1 & 1 \\ \chi_1 & 0 & \zeta_2 & 0 & 0 \\ \sin\zeta_1 & \cos\zeta_1 & \sinh\zeta_2 & \cosh\zeta_2 & 1 \\ \zeta_1\cos\zeta_1 & -\zeta_1\sin\zeta_1 & \zeta_2\cosh\zeta_2 & \zeta_2\sinh\zeta_2 & 0 \\ b^2\zeta_1 h_1 & -b^2\zeta_1 h_2 & b^2\zeta_2 h_3 & b^2\zeta_2 h_4 & \left(\frac{2\omega^2}{\pi^3} - \pi b^2\right) \end{Bmatrix} \tag{A.27}$$

and

$$\mathbf{w} = \begin{bmatrix} -s_5\left(\kappa_1 + \kappa_3\right) \\ -s_5\left(\lambda_1 + \kappa_2\lambda_2\right) \\ -s_5\left(\sin\lambda_1 + \kappa_1\cos\lambda_1 + \kappa_2\sinh\lambda_2 + \kappa_3\cosh\lambda_2\right) \\ -s_5\left(\lambda_1\cos\lambda_1 - \kappa_1\lambda_1\cos\lambda_1 + \kappa_2\lambda_2\cosh\lambda_2 + \kappa_3\lambda_2\sinh\lambda_2\right) \\ -\frac{\Gamma_2}{2\pi} + \frac{2\Gamma_1 c_5}{\pi} - b^2 s_5\left(\lambda_1 g_1 - \lambda_1\kappa_1 g_2 + \lambda_2\kappa_2 g_3 + \lambda_2\kappa_3 g_4\right) \end{bmatrix} \tag{A.28}$$

VITA

Walter Lacarbonara was born on February 27, 1968 in Grottaglie, Italy. He earned a Master of Science degree in the Department of Structural Engineering and Geomechanics from the University of Rome, "La Sapienza" in the Spring of 1993. From 1993 until 1995, he worked as a consultant engineer in the field of structural design. In the Spring of 1995, he won a Rotary Foundation scholarship, which sponsored his first two semesters at Virginia Tech. He enrolled at Virginia Tech in the Fall of 1995.